BOUSSINESQ-TYPE MODEL FOR NEARSHORE WAVE PROCESSES IN FRINGING REEF ENVIRONMENT

A DISSERTATION SUBMITTED TO THE GRADUATE DIVISION OF THE UNIVERSITY OF HAWAI`I AT MĀNOA IN PARTIAL FULFILLMENT OF THE REQUIREMENTS FOR THE DEGREE OF

DOCTOR OF PHILOSOPHY

IN

OCEAN AND RESOURCES ENGINEERING

DECEMBER 2010

By

Volker Roeber

Dissertation Committee:

Kwok Fai Cheung, Chair
Marcelo H. Kobayashi
Geno Pawlak
H. Ronald Riggs
Ian N. Robertson

We certify that we have read this dissertation and that, in our opinion, it is satisfactory in scope and quality as a dissertation for the degree of Doctor of Philosophy in Ocean and Resources Engineering.

DISSERTATION COMMITTEE

_____
Chairperson

_____

_____

_____

_____

ACKNOWLEDGEMENTS

I would like to thank my advisor, Prof. Kwok Fai Cheung, for his excellent guidance and continuous encouragement during my studies. He provided me with the necessary freedom to pursue my research interests; his broad expertise in many fields of engineering as well as his unique ability of analytical thinking are unforgettable.

I would like to thank my committee members: Prof. Marcelo H. Kobayashi for teaching me computational fluid dynamics and providing crucial support during the development of the numerical model, Prof. Geno Pawlak, Prof. H. Ronald Riggs, and Prof. Ian N. Robertson for many fruitful discussions on the numerical model and dissertation, and for their invaluable assistance during the experimental phase of this work.

Special thanks go to Gary Chock and Dr. Lyle Carden from Martin & Chock, Inc. for many productive meetings and constructive criticisms on this research work, and to Prof. Patrick Lynett for providing the data from the benchmark experiment. I am deeply grateful to Prof. George D. Curtis for passing on to me his profound knowledge on tsunamis and introducing me to the Oahu tsunami observer team. Sincere thanks are given to Prof. Chen-Jun Yang for his patience and dedication in helping me to achieve a priceless insight into fluid mechanics.

I would like to thank Prof. Dan Cox, Prof. Solomon Yim, and the entire staff of the O.H. Hinsdale Wave Research Laboratory at Oregon State University for their support and hospitality during the laboratory experiments and throughout my stay in Corvallis, Oregon.

My special thanks go to all my project team colleagues, Dr. Yong Wei, Dr. Yoshiki Yamazaki, Megan Craw, Pablo Duarte-Quiroga, Abdulla Mohamed, Krystian

Paczkowski, Yefei Bai, and Jacob Tyler, for constructive discussions and assistance with model runs and laboratory work.

I would also like to thank those who joined me during my studies in the Department of Ocean and Resources Engineering, Dr. Krishnakumar Rajagopalan, Dr. Liang Ge, Dr. Yongyan Wu, Randi Arinaga, Danny Merritt, Suvabrata Das, Jacob Foster, Justin Stopa, Kay Gemba, Masoud Hayatdavoodi, Richard Carter, Troy Heitmann, Vasco Nunes, and my friends, Fabian Schloesser, Jonathan Weiss, Kolja Rotzoll, Thomas Decloedt, Tobias Friedrich, and Volker Schwarzer. Also, many thanks to the department's staff for taking care of administrative paperwork.

Lastly, I would like to thank my family and my parents, Ingrid and Peter, for unconditional support and encouragement, my brother, Frank, for introducing me to computer programming and being always a very special person in my life. With true love I thank my wife, Maiumi, for always believing in me and for making my life joyful every day. Without Maiumi this dissertation would have been unimaginable.

Financial support for my study was provided in the form of research assistantships from the National Tsunami Hazard Mitigation Program via Hawaii State Civil Defense, the National Science Foundation Grant No. CMS-0530759, and the US Army Corps of Engineers Contract No. W912HZ-09-C-0085.

ABSTRACT

The extended lagoons and steep flanks of most fringing reefs produce unique coastal processes that are challenging to numerical wave models developed for continental shelf conditions. This dissertation describes the formulation and validation of a coastal wave model applicable to fringing reef environment. The governing Boussinesq-type equations, which include a continuity and a momentum equation with conserved variables, contain the conservative form of the nonlinear shallow-water equations for shock capturing.

The finite volume method with a Godunov-type scheme provides a conservative numerical procedure compatible to the present governing equations. A fifth-order TVD (Total Variation Diminishing) reconstruction procedure evaluates the inter-cell variables, while a directional splitting scheme with a Riemann solver supplies the inter-cell flux and bathymetry source terms in the two-dimensional horizontal plane. Time integration of the governing equations provides the conserved variables, which in turn provide the flow velocities through a linear system of equations derived from the dispersive terms in the momentum equations. The model handles wave breaking through momentum conservation based on the Riemann solver without the use of predefined empirical coefficients for energy dissipation.

A series of numerical experiments verify the dispersion characteristics of the model. The computed results show very good agreement with laboratory data for wave propagation over a submerged bar, wave breaking and runup on plane beaches as well as wave transformation over fringing reefs. The model accurately describes transition between supercritical and subcritical flows as well as development of dispersive waves in the processes.

TABLE OF CONTENTS

LIST OF FIGURES

CHAPTER 1
INTRODUCTION

Numerical modeling of nearshore waves is of growing interest in the coastal engineering and science communities. Waves generated in the open ocean by storms or seismic activities undergo drastic changes close to shore due to refraction, shoaling, diffraction, nonlinear wave-wave interaction, and wave breaking. These transformation processes determine the nearshore wave height and runup as well as the circulation patterns and sediment transport. A rising sea level exacerbates the impact of ocean waves to the coastal community. Numerical modeling can effectively describe nearshore wave processes to provide guidelines for hazard mitigation as well as planning and utilization of coastal resources. However, accurate modeling of water wave motion in the nearshore area is still a challenging task. Most wave models cater to continental shelf coasts with gently sloping bathymetry. But many events of destructive waves generated by storms and tsunamis affect tropical areas that are often sheltered by fringing reefs making the nearshore processes far more complex. Nonlinearity and dispersion become important aspects that numerical models have to deal with. Wave breaking over the reef and bore formation in the lagoon with intermittent submergence of coastal features pose additional challenges. Numerical models built upon Boussinesq-type equations include nonlinearity and frequency dispersion and have the potential to handle these nearshore processes.

The pioneer work of Peregrine (1967) provides the foundation for many Boussinesq-type models used today. Madsen & Sørensen (1992) and Nwogu (1993) enhanced the classical Boussinesq equations to an equivalence of a Padé approximation of the linear dispersion relation. The former introduces third-order terms with a free parameter into the momentum equation, while the latter derives from the three-dimensional Euler equations a new set of governing equations with the horizontal velocity evaluated at a reference

depth. The two approaches have identical linear dispersion characteristics that show good agreements with linear wave theory. Madsen & Schäffer (1998), Madsen *et al*. (2003), and Fuhrman & Madsen (2009) provided further improvements by including high-order nonlinearity and frequency dispersion. Wei *et al*. (1995) extended Nwogu's (1993) formulation by retaining higher order nonlinear dispersion terms from the Taylor series expansion and Gobbi *et al*. (2000) derived an approach with fourth-order accuracy in dispersion. These higher-order Boussinesq-type equations are difficult to implement in the two horizontal dimensions for practical applications, but remain useful for theoretical studies with idealized bathymetries. Independent of their numerical formulations, all Boussinesq-type equations satisfy approximate conservation laws in contrast to the nonlinear shallow-water equations that satisfy exact conservation laws for non-dispersive waves.

Wave breaking in the nearshore environment becomes an important modeling issue. As the wave height and steepness increase, frequency dispersion balances amplitude dispersion to produce a local anomaly leading to instability prior to wave breaking. Researchers have developed semi-empirical approaches to account for wave breaking in Boussinesq-type models. These involve addition of a dissipative term to the momentum equation with prescribed criteria for onset and termination of wave breaking and energy dissipation rates. A popular approach is the concept of eddy viscosity (Zelt, 1991; Wei *et al*., 1995; Kennedy *et al*., 2000; Lynett *et al*., 2002). The surface roller concept is another common approach to account for wave breaking (e.g., Svendsen, 1984; Schäffer *et al*., 1993; Madsen *et al*., 1997). The laboratory experiments of Ting & Kirby (1994) for spilling and plunging waves on a plane beach provide a useful dataset for calibration of these semi-empirical wave-breaking models. Alternately, transport equations for vorticity can be incorporated into the governing equations to account for wave breaking

(Veeramony & Svendsen, 2000).

Modeling of wave transformation over fringing reefs involves energetic wave breaking and transition between sub and supercritical flows. Many numerical wave models have difficulties simulating bore-like surges over an extended reef. The conservative form of the nonlinear shallow-water equations and the associated numerical schemes are uniquely suitable to describe these processes (e.g., Toro, 2001; LeVeque, 2002). Godunov-type schemes based on a Riemann solver have remarkable shock-capturing capabilities to describe breaking waves as bores and conserve flow volume and momentum across discontinuities independent of the grid size. The Riemann solver automatically delineates wet and dry cells to track the moving waterline without numerical approximations. Researchers have applied shock-capturing finite volume schemes in coastal and riverine flood hazard modeling (e.g., Dodd, 1998; Pan *et al*., 2007; Begnudelli *et al*., 2008, George, 2010). Although these applications are relevant in some aspects to surf-zone processes, the lack of dispersion in the nonlinear shallow-water equations hampers their application to nearshore wave modeling. Horrillo *et al.* (2006) indicated that frequency dispersion can be important even in long wave processes associated with tsunamis. Dispersive waves from tsunamis of less than 3 min period can resonate over fringing reef bathymetry as demonstrated by Roeber *et al*. (2010).

An approach to remediate the lack of dispersion in the nonlinear shallow-water equations was proposed by Casulli (1998) and Stelling & Zijlema (2003) who reformulated the governing equations from the Navier-Stokes equations to include non-hydrostatic pressure. These equations incorporate effects of low order dispersion and are suitable for large-scale free surface flows such as tides and tsunamis. The standard form of non-hydrostatic shallow-water equations is expressed in physical variables and solved with a finite difference scheme. Bradford (2004) provided a similar formulation with conserved

variables together with a Riemann solver based Godunov-type scheme to account for momentum conservation under supercritical flow conditions. Yamazaki *et al*. (2009, 2010) extended the non-hydrostatic model of Stelling & Zijlema (2003) to describe breaking waves as bores through a momentum conserved advection scheme and include a system of two-way nested grids for basin-wide propagation and coastal runup of tsunamis. These non-hydrostatic approaches might not be amenable to general applications in modeling of coastal processes due to their limited dispersion characteristic. High order dispersion can be achieved in these non-hydrostatic models only through a multi-layer formulation with additional computational effort (Zijlema & Stelling, 2008; Bai & Cheung, 2010).

Generally, Boussinesq-type models have good dispersion characteristics, but often include an *ad hoc* approach to account for wave breaking. The Riemann solver of the conservative form of the nonlinear shallow-water equations provides a good approximation of breaking waves as bores and the resulting energy dissipation without the need for predefined mechanisms. The goal of this dissertation is to combine the merits of the two approaches to develop a nearshore model suitable for, but not limited to, fringing reef-type environment. The proposed model incorporates the shock-capturing capabilities of a Godunov-type scheme with a Riemann solver into a Boussinesq-type dispersive wave model. This includes reformulation of Nwogu's (1993) Boussinesq-type equations in the conservative form of the nonlinear shallow-water equations and derivation of a finite volume scheme for the solution. In contrast to the Boussinesq-type equations in physical variables, the use of conserved variables allows direct implementation of a Godunov-type scheme to handle the transition between sub- and supercritical flows without special flux term treatments to ensure momentum conservation. Since the proposed governing equations are comparable to Nwogu's

(1993), the model should retain the inherent dispersion and shoaling properties independent of the numerical scheme.

In this dissertation, Chapter 2 describes the derivation of the Boussinesq-type equations in conserved variables from the Euler equations. The governing equations are reorganized in the conservative form of the nonlinear shallow-water equations for implementation of the numerical scheme. The linearized governing equations provide analytical expressions for examination of the basic dispersion and shoaling characteristics. Chapter 3 summarizes the finite volume method with a Godunov-type scheme and an adaptation of the TVD (Total Variation Diminishing) technique for reconstruction of the flow variables at the cell interface. This includes the formulation of a system of equations from the dispersive terms in the momentum equations. Chapter 4 summarizes the conventional eddy viscosity approach and the proposed use of a Riemann solver to account for energy dissipation due to wave breaking. The laboratory data of Ting & Kirby (1994) allows calibration and evaluation of the two approaches prior to the implementation. In Chapter 5, a series of standard tests with analytical or laboratory data provides verification and validation of the proposed model. Simulation of solitary wave collision and sinusoidal wave transformation over a submerged bar allow verification and validation of the dispersion and nonlinearity characteristics, while laboratory experiments of solitary wave transformation over a plane beach and a conical island provide a series of validation tests for modeling of wave breaking, bore propagation and runup.

There is, however, a lack of suitable laboratory data to validate wave transformation models for fringing reef environment. Chapter 6 describes a series of flume experiments at the O.H. Hinsdale Wave Research Laboratory, Oregon State University, specifically designed to examine wave propagation and breaking over fringing reefs, reformation of bores in the lagoon, and breaking of the reflected waves with release of dispersive waves.

Chapter 7 examines and validates the capability of the proposed model in describing the unique wave processes over fringing reefs observed in the flume experiments. In addition, the model is implemented to describe wave transformation over a complex three-dimensional reef system, which was a benchmark test with laboratory data at the 2009 NSF-sponsored Benchmark Challenge at Oregon State University. Chapter 8 provides conclusions of this study and outlines future research directions.

CHAPTER 2
MATHEMATICAL FORMULATION

The motion of water waves is three-dimensional. Owing to the simple flow structure in the vertical direction, two-dimensional depth-integrated models usually suffice to describe the pertinent physical processes otherwise not amenable to computationally intensive three-dimensional models. General assumptions leading to these models are low ratios of amplitude to depth and depth to wavelength as elucidate in the seminal work of Peregrine (1967). Nwogu (1993) improved the dispersion characteristics of the classical Boussinesq equations of Peregrine (1967) and that enables modeling of ocean wave processes over a large region for practical applications. This section provides a summary of the commonly used Boussinesq-type approach from Nwogu (1993) and its adaptation with conserved variables to capture three-dimensional wave breaking processes as two-dimensional bores. The dispersion and shoaling relations from the linearized governing equations allow assessment of the validity of the proposed formulation and provide comparisons with those from Airy wave theory, the classical Boussinesq equations, and Nwogu's original formulation.

2.1 Nwogu's Boussinesq-Type Equations

Figure 2.1 shows a schematic of the three-dimensional flow problem defined by a Cartesian coordinate system (x, y, z), in which z is positive upward from the still water level. The symbols η and h indicate the surface elevation and water depth from the still water level. Let t denote time. The Euler equations consist of a continuity equation and momentum equations in the x, y, and z directions as

$$u_x + v_y + w_z = 0, \tag{2.1}$$

$$u_t + uu_x + vu_y + wu_z + \frac{1}{\rho} p_x = 0, \tag{2.2}$$

$$v_t + uv_x + vv_y + wv_z + \frac{1}{\rho} p_y = 0, \tag{2.3}$$

$$w_t + uw_x + vw_y + ww_z + \frac{1}{\rho} p_z + g = 0, \tag{2.4}$$

where (u, v, w) is flow velocity, p is pressure, g is gravitational acceleration, and ρ the fluid density. The irrotational assumption leads to

$$v_x - u_y = 0,\ w_y - v_z = 0,\ u_z - w_x = 0 \tag{2.5}$$

In addition, the flow satisfies the kinematic boundary conditions at the seabed and the free surface as

$$w + uh_x + vh_y = 0 \qquad \text{at } z = -h, \tag{2.6}$$

$$w - \eta_t - u\eta_x - v\eta_y = 0 \qquad \text{at } z = \eta. \tag{2.7}$$

The pressure vanishes at the free surface to give the dynamic free surface boundary condition as

$$p = 0 \qquad \text{at } z = \eta. \tag{2.8}$$

This boundary value problem is computationally intensive, but provides the basis for formulations of many free-surface flow models in research and application.

Most researchers utilize dimensionless variables to highlight their relative magnitude in the physical processes. In the present problem, the independent variables become

$$x^* = \frac{x}{h_o};\ y^* = \frac{y}{h_o};\ z^* = \frac{z}{h_o};\ t^* = t\sqrt{\frac{g}{h_o}}, \tag{2.9}$$

and the dependent variables are

$$p^* = \frac{p}{\rho g h_o};\ \eta^* = \frac{\eta}{h_o};\ u^* = \frac{u}{\sqrt{g h_o}};\ v^* = \frac{v}{\sqrt{g h_o}};\ w^* = \frac{w}{\sqrt{g h_o}}, \tag{2.10}$$

where h_o is a characteristic water depth parameter. Peregrine (1967) derived the classical Boussinesq equations through depth-integration with scaling parameters representing nonlinearity and frequency dispersion as

$$\varepsilon = \frac{a_o}{h_o}, \tag{2.11}$$

$$\mu = \frac{h_o}{\lambda}, \tag{2.12}$$

where a_o is a typical wave amplitude and λ is a typical wavelength. Scaling of the independent horizontal variables and time is carried out as

$$x = \mu x^*,\ y = \mu y^*,\ t = \mu t^*. \tag{2.13}$$

The dependent variables are scaled as

$$\eta = \frac{\eta^*}{\varepsilon},\ u = \frac{u^*}{\varepsilon},\ v = \frac{v^*}{\varepsilon},\ w = \frac{w^*}{\mu\varepsilon}. \tag{2.14}$$

The scaling parameters, which are of $O(0.1)$, adjust the dependent and independent variables differently to capture small amplitude weakly dispersive waves through a perturbation expansion.

Nwogu (1993) derived a set of Boussinesq-type equations using the scaled, dimensionless variables defined in (2.13) and (2.14). Integration of the continuity equation (2.1) to the still water level and implementation of the Leibniz rule give

$$w\big|_z - w\big|_{-h} = -\left(\int_{-h}^{z} u\ dz\right)_x + u\big|_{-h}(-h)_x - u\big|_z z_x - \left(\int_{-h}^{z} v\ dz\right)_y + v\big|_{-h}(-h)_y - v\big|_z z_y. \tag{2.15}$$

Applying the bottom boundary condition (2.6) gives the vertical velocity component in terms of the horizontal components

$$w = -\left(\int_{-h}^{z} u\ dz\right)_x - \left(\int_{-h}^{z} v\ dz\right)_y \tag{2.16}$$

Substitution of (2.16) into the irrotationality conditions (2.5) gives

$$u_z = -\mu^2\left(\int_{-h}^{z} u\ dz\right)_{xx}, \tag{2.17a}$$

$$v_z = -\mu^2\left(\int_{-h}^{z} v\ dz\right)_{yy}. \tag{2.17b}$$

The tenet of Nwogu's (1993) formulation is the approximation of the horizontal velocity components u and v by a Taylor series expansion about an arbitrary depth $z = z_\alpha$

$$u = u\big|_{z=z_\alpha} + (z - z_\alpha)u_z\big|_{z=z_\alpha} + \frac{(z - z_\alpha)^2}{2}u_{zz}\big|_{z=z_\alpha} + \frac{(z - z_\alpha)^3}{6}u_{zzz}\big|_{z=z_\alpha} + \ldots \tag{2.18a}$$

$$v = v\big|_{z=z_\alpha} + (z - z_\alpha)v_z\big|_{z=z_\alpha} + \frac{(z - z_\alpha)^2}{2}v_{zz}\big|_{z=v} + \frac{(z - z_\alpha)^3}{6}v_{zzz}\big|_{z=z_\alpha} + \ldots \tag{2.18b}$$

This introduces a free parameter to optimize the dispersion of the classical Boussinesq equation for a range of μ. Combining (2.17) and (2.18) gives the horizontal velocity components evaluated at the arbitrary depth $z = z_\alpha$

$$u = u\big|_{z=z_\alpha} - \mu^2\left((z - z_\alpha)\left(u(h + z_\alpha)\right)_{xx} + \left(\frac{(z - z_\alpha)^2}{2}\right)_{xx}\right)_{z=z_\alpha}, \tag{2.19a}$$

$$v = v\big|_{z=z_\alpha} - \mu^2\left((z - z_\alpha)\left(v(h + z_\alpha)\right)_{yy} + \left(\frac{(z - z_\alpha)^2}{2}\right)_{yy}\right)_{z=z_\alpha}. \tag{2.19b}$$

Substitution of (2.19a, b) into (2.16) gives

$$\begin{aligned} w = &-\left((h + z)u + \mu^2\left(\frac{(h + z_\alpha)^2}{2}\right)\left(u(h + z_\alpha)\right)_x - \left(\frac{(h + z_\alpha)^3}{6}\right)u_{xx}\right)_x \\ &-\left((h + z)v + \mu^2\left(\frac{(h + z_\alpha)^2}{2}\right)\left(v(h + z_\alpha)\right)_y - \left(\frac{(h + z_\alpha)^3}{6}\right)v_{yy}\right)_y \end{aligned} \tag{2.20}$$

The vertical velocity component is expressed in terms of the horizontal components and its derivatives.

The vertical momentum equation (2.4) now gives the pressure p in terms of the horizontal velocity components

$$-p_z = 1 - \mu^2\varepsilon\left((z+h)u\right)_{xt} - \mu^2\varepsilon\left((z+h)v\right)_{yt}. \tag{2.21}$$

Integration of the pressure from the depth z to the free surface $\varepsilon\eta$ and implementation of the dynamic free surface boundary condition give

$$p\big|_{z=-h} = \varepsilon\eta - z + \mu^2\varepsilon\left(\left(\frac{z^2}{2}+hz\right)u\right)_{xt} - \mu^2\varepsilon\left(\left(\frac{z^2}{2}+hz\right)u\right)_{xt}. \tag{2.22}$$

With the velocity components and bottom pressure, depth integration of the horizontal momentum equations (2.2) and (2.3) provides the momentum equations in the formulation of Nwogu (1993). Returning to dimensional variables, the equations read

$$u_t + uu_x + vu_y + g\eta_x + \frac{z_\alpha^2}{2}\left(u_{txx} + v_{txy}\right) + z_\alpha\left(\left(hu_t\right)_{xx} + \left(hv_t\right)_{xy}\right) = O\left(\varepsilon\mu^2, \mu^4\right), \tag{2.23}$$

$$v_t + vv_y + uv_x + g\eta_y + \frac{z_\alpha^2}{2}\left(v_{tyy} + u_{txy}\right) + z_\alpha\left(\left(hv_t\right)_{yy} + \left(hu_t\right)_{xy}\right) = O\left(\varepsilon\mu^2, \mu^4\right). \tag{2.24}$$

Depth integration of the continuity equation (2.1) from the bottom at $z = -h$ to the free surface $\varepsilon\eta$, implementation of the Leibniz rule to incorporate the boundary conditions, and making use of the velocity components (2.19a, b) and (2.20) provide the final continuity equation. In dimensional form,

$$\begin{aligned}
&\eta_t + \left((h+\eta)u\right)_x + \left((h+\eta)v\right)_y \\
&+\left(\frac{z_\alpha^2}{2} - \frac{h^2}{6}\right)h\left(u_{xx} + v_{xy}\right) + \left[\left(z_\alpha + \frac{h}{2}\right)h\left(\left(hu\right)_{xx} + \left(hv\right)_{xy}\right)\right]_x \\
&+\left[\left(\frac{z_\alpha^2}{2} - \frac{h^2}{6}\right)h\left(v_{yy} + u_{xy}\right) + \left(z_\alpha + \frac{h}{2}\right)h\left(\left(hv\right)_{yy} + \left(hu\right)_{xy}\right)\right]_y = O\left(\varepsilon\mu^2, \mu^4\right).
\end{aligned} \tag{2.25}$$

The Boussinesq-type equations are truncated at $O(\varepsilon\mu^2,\mu^4)$ with the parameters ε and μ assumed to be small and of the same order. This approach does not resolve the non-hydrostatic pressure in deep water and, in theory, limits the application in shallow and intermediate water depth. The applicable range can be defined by the Ursell number, which relates the nonlinearity and dispersion as

$$U_r = \frac{\varepsilon}{\mu^2} = \frac{a_o \lambda^2}{h_o^3}, \tag{2.26}$$

The Boussinesq-type equations of Nwogu (1993) are valid for $U_r = O(10)$. The optimization of the dispersion through z_α would account for larger values of μ, thereby extending the applicable range in terms of the Ursell parameter.

2.2 Formulation in Conserved Variables

The horizontal velocity in the Boussinesq-type equations derived by Nwogu (1993) is evaluated at an arbitrary depth z_α, from which the vertical flow structure can be derived. The equations contain the non-conserved variables (u, v) and η. In the absence of frequency dispersion, the equations reduce to the nonlinear shallow-water equations in the form

$$\eta_t + \left((h+\eta)u\right)_x + \left((h+\eta)v\right)_y = 0, \tag{2.27}$$

$$u_t + uu_x + vu_y + g\eta_x = 0, \tag{2.28}$$

$$v_t + vv_y + uv_x + g\eta_y = 0, \tag{2.29}$$

The continuity equation (2.27) already utilizes the conserved variable $H = (h + \eta)$. Let (U, V) denote (u, v) for the depth-averaged velocity. With a stationary bathymetry, the equation can be expressed in the conserved variables (HU, HV) and H as

$$H_t + (HU)_x + (HV)_y = 0, \tag{2.30}$$

Combining (2.30) and (2.28) pre-multiplied by U and H and (2.30) and (2.29) pre-multiplied by V and H respectively, gives the momentum equations in conserved variables

$$(HU)_t + \left(HU^2\right)_x + (HUV)_y + Hg\eta_x = 0, \tag{2.31}$$

$$(HV)_t + \left(HV^2\right)_y + (HUV)_x + Hg\eta_y = 0. \tag{2.32}$$

The momentum equations (2.28) and (2.29) express the same conservation law as (2.31) and (2.32), but can cater to the full solution of the hyperbolic system of equations. Reorganizing the flux terms as

$$\frac{1}{H}\left[\left(HU^2\right)_x + (HUV)_y\right] = UU_x + VU_y + \frac{U}{H}\left[(HU)_x + (HV)_y\right] = UU_x + VU_y + \frac{U}{H}H_t, \tag{2.33}$$

$$\frac{1}{H}\left[\left(HV^2\right)_y + (HUV)_x\right] = VV_y + UV_x + \frac{V}{H}\left[(HV)_y + (HU)_x\right] = VV_y + UV_x + \frac{V}{H}H_t, \tag{2.34}$$

shows additional terms related to flow continuity in comparison to the momentum equations (2.28) and (2.29) in non-conserved variables.

The nonlinear shallow-water equations in conserved variables have been extensively used for flood hazard modeling because of their ability to handle flux dominated flows even with discontinuities. A numerical model for nearshore wave processes based on Boussinesq-type equations would benefit significantly from a similar conservative structure. The continuity equation (2.25) in the Nwogu's (1993) formulation can readily be expressed in terms of the conserved variables as in (2.30). The local acceleration and flux terms in the momentum equations (2.23) and (2.24) need to be expressed in terms of conserved variables (*HU*, *HV*). To this end, the local acceleration and flux terms of the

momentum equations (2.31) and (2.32) in the conservative form of the nonlinear shallow-water equations can be expanded as

$$(HU)_t + \left(HU^2\right)_x + (HUV)_y = H\left(U_t + UU_x + VU_y\right) + U\left(H_t + (HU)_x + (HV)_y\right) \tag{2.35}$$

$$(HV)_t + \left(HV^2\right)_y + (HUV)_x = H\left(V_t + VV_y + UV_x\right) + U\left(H_t + (HU)_x + (HV)_y\right) \tag{2.36}$$

Equations (2.35) and (2.36) are identical to

$$H\left(u_t + uu_x + vu_y\right) = (HU)_t + \left(HU^2\right)_x + (HUV)_y - U\left(\eta_t + \left((h+\eta)u\right)_x + \left((h+\eta)v\right)_y\right) \tag{2.37}$$

$$H\left(v_t + vv_y + uv_x\right) = (HV)_t + \left(HV^2\right)_y + (HUV)_x - V\left(\eta_t + \left((h+\eta)u\right)_x + \left((h+\eta)v\right)_y\right) \tag{2.38}$$

After multiplying (2.23) and (2.24) by H, substitution of (2.37) and (2.38) gives

$$\begin{aligned}(HU)_t + \left(HU^2\right)_x + (HUV)_y + H\left(g\eta_x + \frac{z_\alpha^2}{2}\left(u_{txx} + v_{txy}\right) + z_\alpha\left(\left(hu_t\right)_{xx} + \left(hv_t\right)_{xy}\right)\right) \\ - U\left(\eta_t + \left((h+\eta)u\right)_x + \left((h+\eta)v\right)_y\right) = 0\end{aligned} \tag{2.39}$$

$$\begin{aligned}(HV)_t + \left(HV^2\right)_y + (HUV)_x + H\left(g\eta_y + \frac{z_\alpha^2}{2}\left(v_{tyy} + u_{txy}\right) + z_\alpha\left(\left(hv_t\right)_{yy} + \left(hu_t\right)_{xy}\right)\right) \\ - V\left(\eta_t + \left((h+\eta)u\right)_x + \left((h+\eta)v\right)_y\right) = 0\end{aligned} \tag{2.40}$$

The last terms in (2.39) and (2.40) contain the local acceleration and flux terms from the continuity equation (2.25) that can be replaced by the corresponding dispersion term.

The formulation has replaced the local acceleration and flux terms in the continuity and momentum equations in Nwogu's (1993) formulation with conserved variables. The resulting Boussinesq-type equations are given by

$$\begin{aligned}H_t + (HU)_x + (HV)_y + \left[\left(\frac{z_\alpha^2}{2} - \frac{h^2}{6}\right)h\left(U_{xx} + V_{xy}\right) + \left(z_\alpha + \frac{h}{2}\right)h\left((hU)_{xx} + (hV)_{xy}\right)\right]_x \\ + \left[\left(\frac{z_\alpha^2}{2} - \frac{h^2}{6}\right)h\left(U_{xy} + V_{yy}\right) + \left(z_\alpha + \frac{h}{2}\right)h\left((hU)_{xy} + (hV)_{yy}\right)\right]_y = 0\end{aligned} \tag{2.41}$$

$$
\begin{aligned}
&(HU)_t + \left(HU^2\right)_x + (HUV)_y + gH\eta_x \\
&+H\frac{z_\alpha^2}{2}\left[U_{xxt} + V_{xyt}\right] + Hz_\alpha\left[(hU_t)_{xx} + (hV_t)_{xy}\right] \\
&+U\left[\left(\frac{z_\alpha^2}{2} - \frac{h^2}{6}\right)h\left(U_{xx} + V_{xy}\right) + \left(z_\alpha + \frac{h}{2}\right)h\left((hU)_{xx} + (hV)_{xy}\right)\right]_x \\
&+U\left[\left(\frac{z_\alpha^2}{2} - \frac{h^2}{6}\right)h\left(U_{xy} + V_{yy}\right) + \left(z_\alpha + \frac{h}{2}\right)h\left((hU)_{xy} + (hV)_{yy}\right)\right]_y = 0
\end{aligned}
\tag{2.42}
$$

$$
\begin{aligned}
&(HV)_t + \left(HV^2\right)_y + (HUV)_x + gH\eta_y \\
&+H\frac{z_\alpha^2}{2}\left[V_{yyt} + U_{xyt}\right] + Hz_\alpha\left[(hV_t)_{yy} + (hU_t)_{xy}\right] \\
&+V\left[\left(\frac{z_\alpha^2}{2} - \frac{h^2}{6}\right)h\left(U_{xx} + V_{xy}\right) + \left(z_\alpha + \frac{h}{2}\right)h\left((hU)_{xx} + (hV)_{xy}\right)\right]_x \\
&+V\left[\left(\frac{z_\alpha^2}{2} - \frac{h^2}{6}\right)h\left(U_{xy} + V_{yy}\right) + \left(z_\alpha + \frac{h}{2}\right)h\left((hU)_{xy} + (hV)_{yy}\right)\right]_y = 0
\end{aligned}
\tag{2.43}
$$

The final governing equations consist of the conservative form of the nonlinear shallow-water equations and the dispersion terms derived from Nwogu (1993). Because flux and dispersion are counteracting processes, it is important not to alter the dispersion terms with the conserved variables that are meant for flux-dominated processes.

2.3 Conservative Form for Shock-Capturing

The nonlinear shallow-water equations are hyperbolic and admit both continuous and discontinuous solutions. Their conservative form has been used extensively in shock-wave modeling. The governing equations (2.41) - (2.43) can be rearranged in the conservative form of the nonlinear shallow-water equations. In the momentum equations (2.42) and (2.43), the terms including the free surface gradients are expanded with respect to the conserved variable H only as

$$
hH\eta_x = \frac{1}{2}g\left(H^2\right)_x - gHh_x, \tag{2.44a}
$$

$$hH\eta_y = \frac{1}{2} g\left(H^2\right)_y - gHh_y . \tag{2.44b}$$

The dispersion terms $Hz_\alpha[0.5z_\alpha U_{txx}+(hU_t)_{xx}]$ and $Hz_\alpha[0.5z_\alpha V_{tyy}+(hV_t)_{yy}]$, which involve products of a time-dependent variable and temporal derivatives and present a challenge to the time integration, are expanded as

$$Hz_\alpha\left[0.5z_\alpha U_{txx} + \left(hU_t\right)_{xx}\right] = \frac{z_\alpha^2}{2}\left(HU_{xx}\right)_t + z_\alpha\left(hHU_{xx}\right)_t - \frac{z_\alpha^2}{2} H_t U_{xx} - z_\alpha H_t \left(hU\right)_{xx}, \tag{2.45a}$$

$$Hz_\alpha\left[0.5z_\alpha V_{tyy} + \left(hV_t\right)_{yy}\right] = \frac{z_\alpha^2}{2}\left(HV_{xx}\right)_t + z_\alpha\left(hHV_{xx}\right)_t - \frac{z_\alpha^2}{2} H_t V_{yy} - z_\alpha H_t \left(hV\right)_{yy} . \tag{2.45b}$$

Even though the last two terms on the right hand still contain products of a temporal derivative and time-dependent variables, the temporal derivative H_t is directly given by the continuity equation (2.41) in terms of spatial derivatives only.

With the expansions (2.44) and (2.45), the governing equations (2.41) - (2.43) are written in matrix form analogous to the nonlinear shallow-water equations as

$$\mathbf{U}_t + \mathbf{F}\left(\mathbf{U}\right)_x + \mathbf{G}\left(\mathbf{U}\right)_y + \mathbf{S}\left(\mathbf{U}\right) = 0, \tag{2.46}$$

where **U** is the vector of the conserved variables, **F** and **G** are the flux vectors in x and y directions respectively, and **S** is the source term, given respectively as

$$\mathbf{U} = \begin{bmatrix} H \\ P \\ Q \end{bmatrix} \quad \mathbf{F} = \begin{bmatrix} HU \\ HU^2 + \frac{1}{2} gH^2 \\ HUV \end{bmatrix} \quad \mathbf{G} = \begin{bmatrix} HV \\ HVU \\ HV^2 + \frac{1}{2} gH^2 \end{bmatrix}$$

$$\mathbf{S} = \begin{bmatrix} \psi_C \\ -gHh_x - \psi_{P1} + U\psi_C + \psi_{P2} + \tau_1 \\ -gHh_y - \psi_{Q1} + V\psi_C + \psi_{Q2} + \tau_2 \end{bmatrix} \tag{2.47}$$

In comparison to the nonlinear shallow-water equations, the evolution variables P and Q include the flux-related terms from the right hand side of (2.45)

$$P = HU + z_\alpha\left[0.5 z_\alpha HU_{xx} + \left(hHU\right)_{xx}\right], \tag{2.48}$$

$$Q = HV + z_\alpha\left[0.5 z_\alpha HV_{xx} + \left(hHV\right)_{xx}\right]. \tag{2.49}$$

This approach groups all time derivative terms into the evolution variables to simplify the time integration. The remaining terms in (2.45) become part of the source term accounting for dispersion

$$\psi_{P1} = H_t z_\alpha\left[0.5 z_\alpha U_{xx} + \left(hU\right)_{xx}\right], \tag{2.50}$$

$$\psi_{Q1} = H_t z_\alpha\left[0.5 z_\alpha V_{yy} + \left(hV\right)_{yy}\right]. \tag{2.51}$$

The other dispersion terms ψ_C, ψ_{P2}, and ψ_{Q2} are defined as

$$\begin{aligned}\psi_C = &\left[\left(\frac{z_\alpha^2}{2} - \frac{h^2}{6}\right)h\left(U_{xx} + V_{xy}\right) + \left(z_\alpha + \frac{h}{2}\right)h\left(\left(hU\right)_{xx} + \left(hV\right)_{xy}\right)\right]_x \\ &+ \left[\left(\frac{z_\alpha^2}{2} - \frac{h^2}{6}\right)h\left(U_{xy} + V_{yy}\right) + \left(z_\alpha + \frac{h}{2}\right)h\left(\left(hU\right)_{xy} + \left(hV\right)_{yy}\right)\right]_y,\end{aligned} \tag{2.52}$$

$$\psi_{P2} = Hz_\alpha\left[0.5 z_\alpha V_{xyt} + \left(hV\right)_{xyt}\right], \tag{2.53}$$

$$\psi_{Q2} = Hz_\alpha\left[0.5 z_\alpha U_{xyt} + \left(hU\right)_{xyt}\right]. \tag{2.54}$$

The friction terms are given by

$$\tau_1 = \frac{gn^2}{H} U\sqrt{U^2 + V^2}, \tag{2.55}$$

$$\tau_2 = \frac{gn^2}{H} V\sqrt{U^2 + V^2}, \tag{2.56}$$

where n is the Manning coefficient representing bottom roughness. Bretschneider *et al.* (1986) determined the Manning coefficient for large-scale roughness by measuring wind

profiles over typical terrain in Hawaii covered by lava rocks, coral rocks, and dense vegetation.

A solution for the mass flux and shock speed across a flow discontinuity is derived to show the governing equation (2.46) inherits a structure for correct representation of the physical processes. In the absence of the dispersion and source terms, the governing equation reduces to the conservative and homogeneous form of the nonlinear shallow-water equations for a pure advection system. In one dimension,

$$\begin{bmatrix} H \\ HU \end{bmatrix}_t + \begin{bmatrix} HU \\ HU^2 + \frac{1}{2} gH^2 \end{bmatrix}_x = 0. \tag{2.57}$$

Similarly, the Boussinesq-type equations (2.23) - (2.25) of Nwogu (1993) based on non-conserved variables gives rise to

$$\begin{bmatrix} \eta \\ U \end{bmatrix}_t + \begin{bmatrix} (h+\eta)U \\ \frac{1}{2}U^2 + gh \end{bmatrix}_x = 0. \tag{2.58}$$

Both equations represent conservation laws of mass and momentum. However, the Rankine-Hugoniot condition can show only (2.57) satisfies the conservation laws when discontinuities develop. A complete detailed derivation of the Rankine-Hugoniot condition is presented in the Appendix.

The Rankine-Hugoniot condition is set up for a linear system of equations with $h = H$ (Toro, 2001). The vector of conserved variables becomes

$$\mathbf{U} = \begin{bmatrix} h \\ hu \end{bmatrix}, \tag{2.59}$$

and the governing equation (2.57) leads to

$$\mathbf{U}_t + \mathbf{F}(\mathbf{U})_x = 0. \tag{2.60}$$

This equation defines the temporal change of conserved quantities in terms of the fluxes. When a discontinuity develops, the flux propagates through a shock. The flow parameters on the two sides of the discontinuity define the shock speed C_S through the Rankine-Hugoniot jump condition

$$C_S\left(\mathbf{U}_L - \mathbf{U}_R\right) = \mathbf{F}\left(\mathbf{U}_L\right) - \mathbf{F}\left(\mathbf{U}_R\right), \tag{2.61}$$

where the subscripts L and R denote the flow parameters to the left and right of the shock. The shock corresponds to a system of intersecting characteristics from the left and right states. It is necessary to utilize the entropy condition to identify a physically acceptable and unique solution. The entropy condition states the relation between the shock speed and the characteristic speeds on the two sides as

$$C\left(\mathbf{U}_L\right) > C_S > C\left(\mathbf{U}_R\right). \tag{2.62}$$

Equation (2.61) gives the speed for a right moving shock as

$$C_S = U_R + \sqrt{g\frac{\left(h_* + h_R\right)h_*}{2h_R}}, \tag{2.63}$$

where h_* is the water depth in the star region. However, the shock speed from (2.61) based on non-conserved variables is

$$C_S = U_R + \sqrt{g\frac{2h_*^2}{h_* + h_R}}. \tag{2.64}$$

Even though (2.57) and (2.58) mathematically describe systems of conservation laws, the shock speeds in (2.63) and (2.64) are equivalent only for a continuous solution with $h_* = h_R$. In (2.64), the conservation of mass is correct, but the conservation of particle speed is physically meaningless. The lack of conservation of momentum results in wrong shock speeds and mass fluxes for discontinuous solutions. The errors are cumulative and cannot be overcome by just using a conservative numerical scheme.

The governing equation (2.46) allows implementation of the local acceleration, flux, and bottom gradient terms into a conservative numerical scheme to handle discontinuous flows. However, the dispersion terms are derived from approximations of the velocity profile. The governing equations might not fully satisfy exact conservation laws even in the conservative form of the nonlinear shallow-water equations.

2.4 Linear Dispersion and Shoaling

The linear dispersion and shoaling properties provide a reference for evaluation of the proposed governing equations. After replacing H by h and dropping the nonlinear terms, the same linearized governing equations as in Nwogu (1993) arise. In the x direction, they become

$$\eta_t + hu_x + \left(\frac{z_\alpha^2}{2} - \frac{h^2}{6}\right)hu_{xxx} + \left(z_\alpha + \frac{h}{2}\right)h^2 u_{xxx} = 0 \tag{2.64}$$

$$u_t + g\eta_x + \frac{z_\alpha^2}{2}u_{txx} + z_\alpha hu_{txx} = 0 \tag{2.65}$$

The dispersion and shoaling properties depend on the depth z_α, where the flow velocity is evaluated. The depth z_α is part of the dispersive terms in both equations. Nwogu (1993) introduced a single parameter α to represent the terms containing z_α as

$$\alpha = 0.5\left(\frac{z_\alpha}{h}\right)^2 + \left(\frac{z_\alpha}{h}\right). \tag{2.66}$$

The governing equations become

$$\eta_t + hu_x + \left(\alpha + \frac{1}{3}\right)h^3 u_{xxx} = 0, \tag{2.67}$$

$$u_t + g\eta_x + \alpha\, h^2 u_{txx} = 0. \tag{2.68}$$

The parameter α is pre-determined from (2.67) and (2.68) to define the value of z_α for expected applications of the governing equations (2.41) - (2.43).

To derive a linear dispersion relation, we consider a system of small amplitude periodic waves as

$$\eta(x,t) = a\sin(kx - \omega t) \tag{2.69}$$

$$u(x,t) = b\sin(kx - \omega t) \tag{2.70}$$

where a and b are the respective amplitudes, k denotes the wave number $2\pi/\lambda$, and ω is the angular frequency. Substitution of (2.69) and (2.70) into the linearized form of the governing equations gives

$$-a\omega + hbk - \left(\alpha + \frac{1}{3}\right)h^3 bk^3 = 0 \tag{2.71}$$

$$-b\omega + gak + \alpha h^2 b\omega k^2 = 0 \tag{2.72}$$

Solving (2.71) for b leads to

$$b = \frac{a\omega}{hk\left(1 - \left(\alpha + \frac{1}{3}\right)h^2k^2\right)} \tag{2.73}$$

Substitution of (2.73) and (2.72) gives the dispersion relation

$$C = \left(\frac{\omega^2}{k^2}\right)^{1/2} = \left[gh\frac{1 - \left(\alpha + \frac{1}{3}\right)h^2k^2}{1 - \alpha h^2k^2}\right]^{1/2} \tag{2.74}$$

The group velocity, which is related to energy propagation and shoaling of gravity waves, is given in terms of the celerity as

$$C_g = \frac{\partial\omega}{\partial k} = \frac{\partial}{\partial k}(kC) = C + k\frac{\partial C}{\partial k} = C\left[1 - \frac{k^2h^2}{3\left(1 - \alpha k^2h^2\right)\left(1 - (\alpha + 1/3)k^2h^2\right)}\right]. \tag{2.75}$$

Shoaling is the result of the decrease of the group velocity with water depth leading to an increase in wave height, since the energy flux has to be constant. Based on the constancy of energy flux, Beji & Nadaoka (1996) defined the shoaling coefficient in terms of the group velocity. For the group velocity (2.75), the shoaling coefficient is given by

$$S = \frac{\frac{1}{2} + \left[\frac{-2k^2h^2}{K1\ K2}\left(\frac{K3}{3\ K1\left(1-(\alpha+1/3)k^2h^2\right)-k^2h^2}-1\right)\right]}{\frac{4}{K1\ K2}\left(1+(\alpha+1/3)(\alpha k^2h^2-2)k^2h^2\right)}, \tag{2.76}$$

where $K1 = 1-\alpha k^2h^2$, $K2 = 1-(\alpha+1/3)k^2h^2$, and $K3 = 1-(\alpha+1/3)k^4h^4$. The optimal value of α can be determined to optimize the celerity (2.74) and shoaling coefficient (2.76) for a specific range of *kh*.

Figure 2.2 shows the ratio of the celerity from (2.74) and Airy wave theory versus the water depth parameter *kh*. The results illustrate the effect of α on wave dispersion in the model. When α = -1/3, the computed celerity is equivalent to that of the classical Boussinesq equation of Peregrine (1967) for long waves. Nwogu (1993) determined α = -0.393 to minimize the error between the dispersion relations of the linearized governing equations and Airy wave theory for $kh < \pi$. This covers the frequency range of the incident waves, but might not account for the high frequency dispersive components generated from coastal wave transformation. The present study considers a larger range of $kh < 2\pi$ but with stronger emphasis on $kh < \pi$. The optimal value of α = -0.38519 is determined through minimization of the error

$$err = \int_0^{\pi}\left(\left|C - C_{Airy}\right|/C_{Airy}\right)^2 \mathrm{d}(kh) + \int_{\pi}^{2\pi}\left(\left|C - C_{Airy}\right|/C_{Airy}\right)\mathrm{d}(kh). \tag{2.77}$$

This places more weight on the minimization of the dispersion error at low *kh* that affects the solution more significantly than the errors in low-energy, high-frequency dispersive waves. The difference in celerity is below 1 % for $kh < \pi$ and below 4% at kh = 5. It

should be noted that at kh = 3.443 the dispersion characteristics agree perfectly with Airy wave theory. The value of α = -0.38519 thereby extends the applicability of the governing equations to high frequency dispersive waves. Figure 2.3 compares the shoaling coefficient from (2.76) with that based on Airy wave theory from Madsen (1992). The use of α = -0.38519 also improves the shoaling property of the equations at higher values of kh. This gives z_α = -0.5208132 from (2.66), leading to the horizontal velocity (U, V) defined slightly below mid depth.

CHAPTER 3
NUMERICAL FORMULATION

The finite volume method with a Godunov-type scheme described in this chapter is complementary with the governing equations to capture shock-related processes. This imposes conservation laws of mass and momentum at each cell in the computational domain. The numerical formulation includes an adaptation of a polynomial reconstruction technique with a TVD (Total Variation Diminishing) limiter. This provides the flow variables on either side of the cell interface and the input to the Riemann solver to determine the interface flow variables for the flux terms. A high-order Godunov-type scheme integrates the evolution variables in time. The dispersion terms in the evolution variables provides two systems of equations for the solutions of the flow velocity.

3.1 Explicit Time Integration

The governing equations (2.41) - (2.43) contain a mix of flux and dispersion terms that require different numerical treatments. It is convenient to rearrange the governing equations in a modular structure similar to Wei *et al*. (1995) for the finite volume formulation and code development:

$$H_t = E(H,U,V) \tag{3.2}$$

$$\left[P(H,U)\right]_t = F_1(H,U,V) + \left[F_2(V)\right]_t \tag{3.3}$$

$$\left[Q(H,U)\right]_t = G_1(H,U,V) + \left[G_2(U)\right]_t \tag{3.4}$$

This arrangement places the evolution variables on the left-hand side for the time integration, while the time derivatives on the right-hand side are evaluated based on

quantities from previous time steps. The right hand side of (3.2) contains a mix flux and dispersion terms as in the original governing equations

$$E(H,U,V) = -(HU)_x - (HV)_y - \psi_C . \tag{3.5}$$

In the momentum equations (3.3) and (3.4), F_1 and G_1 include the flux, dispersion, and bottom friction terms,

$$F_1(H,U,V) = -\left(HU^2 + \frac{1}{2}gH^2\right)_x - (HUV)_y + gHh_x + \psi_{P1} - U\psi_C - \tau_1, \tag{3.6}$$

$$G_1(H,U,V) = -\left(HV^2 + \frac{1}{2}gH^2\right)_y - (HUV)_x + gHh_y + \psi_{Q1} - V\psi_C - \tau_2, \tag{3.7}$$

and F_2 and G_2 contain the cross derivatives as

$$F_2(V) = -\psi_{P2} \tag{3.8}$$

$$G_2(U) = -\psi_{Q2}. \tag{3.9}$$

In the absence of dispersion, (3.5), (3.6), and (3.7) reduce to the nonlinear shallow-water equations and (3.8) and (3.9) vanish. This equation structure excludes the cross derivatives from the evolution variables and decouples the x and y flow parameters in the solution process.

The time-integration scheme should at least match the order of truncation errors from the spatial derivatives in the dispersion term (Wei & Kirby, 1995). With third-order spatial derivatives, the time integration utilizes an explicit fourth-order Adams-Bashforth-Moulton method leading to a truncation error of $O(\Delta t^4)$. Let Δt denote the time step. The third-order predictor provides an intermediate solution of the evolution variables H'^{n+1}, P'^{n+1}, and Q'^{n+1} explicitly as

$$H'^{n+1}_{i,j} = H^n_{i,j} + \frac{\Delta t}{12}\left[23E^n_{i,j} - 16E^{n-1}_{i,j} + 5E^{n-2}_{i,j}\right], \tag{3.10}$$

$$P_{i,j}^{\prime n+1} = P_{i,j}^{n} + \frac{\Delta t}{12}\left[23\left(F_1\right)_{i,j}^{n} - 16\left(F_1\right)_{i,j}^{n-1} + 5\left(F_1\right)_{i,j}^{n-2}\right] + \frac{\Delta t}{12}\left[23\left(F_{2t}\right)_{i,j}^{n} - 16\left(F_{2t}\right)_{i,j}^{n-1} + 5\left(F_{2t}\right)_{i,j}^{n-2}\right], \tag{3.11}$$

$$Q_{i,j}^{\prime n+1} = Q_{i,j}^{n} + \frac{\Delta t}{12}\left[23\left(G_1\right)_{i,j}^{n} - 16\left(G_1\right)_{i,j}^{n-1} + 5\left(G_1\right)_{i,j}^{n-2}\right] + \frac{\Delta t}{12}\left[23\left(G_{2t}\right)_{i,j}^{n} - 16\left(G_{2t}\right)_{i,j}^{n-1} + 5\left(G_{2t}\right)_{i,j}^{n-2}\right], \tag{3.12}$$

where the subscripts i and j are indices in the x and y direction at the cell centroid as shown on Figure 3.1 and n indicates the present time step. The intermediate solution of $H^{\prime n+1}$, $P^{\prime n+1}$, and $Q^{\prime n+1}$ leads to estimates of $E^{\prime n+1}$, $F_1^{\prime n+1}$, $G_1^{\prime n+1}$, $F_2^{\prime n+1}$, and $G_2^{\prime n+1}$ for the fourth-order corrector step as

$$H_{i,j}^{n+1} = H_{i,j}^{n} + \frac{\Delta t}{24}\left[9E_{i,j}^{\prime n+1} + 19E_{i,j}^{n} - 5E_{i,j}^{n-1} + E_{i,j}^{n-1}\right], \tag{3.13}$$

$$P_{i,j}^{n+1} = P_{i,j}^{n} + \frac{\Delta t}{24}\left[9\left(F_1^{\prime}\right)_{i,j}^{n+1} + 19\left(F_1\right)_{i,j}^{n} - 5\left(F_1\right)_{i,j}^{n-1} + \left(F_1\right)_{i,j}^{n-2}\right] \frac{\Delta t}{24}\left[9\left(F_2^{\prime}\right)_{i,j}^{n+1} + 19\left(F_2\right)_{i,j}^{n} - 5\left(F_2\right)_{i,j}^{n-1} + \left(F_2\right)_{i,j}^{n-2}\right], \tag{3.14}$$

$$Q_{i,j}^{n+1} = Q_{i,j}^{n} + \frac{\Delta t}{24}\left[9\left(G_1^{\prime}\right)_{i,j}^{n+1} + 19\left(G_1\right)_{i,j}^{n} - 5\left(G_1\right)_{i,j}^{n-1} + \left(G_1\right)_{i,j}^{n-2}\right] \frac{\Delta t}{24}\left[9\left(G_2^{\prime}\right)_{i,j}^{n+1} + 19\left(G_2\right)_{i,j}^{n} - 5\left(G_2\right)_{i,j}^{n-1} + \left(G_2\right)_{i,j}^{n-2}\right]. \tag{3.15}$$

Both the predictor and corrector steps include cross-derivative terms from the momentum equation that require additional numerical treatment.

In contrast to F_1 and G_1, the cross terms F_{2t} and G_{2t} do not contribute to the nonlinear flux terms and can be evaluated independently from values of F_2 and G_2 at previous time steps through a Taylor-series expansion. Denoting $\phi = [F_2(V), G_2(U)]$, the values at all four time steps involved in the predictor step are stated as

$$\left(\phi_t\right)_{i,j}^{n} = \frac{1}{6\Delta t}\left[11\phi_{i,j}^{n} - 18\phi_{i,j}^{n-1} + 9\phi_{i,j}^{n-2} - 2\phi_{i,j}^{n-3}\right] + O\left(\Delta t^3\right) \tag{3.16}$$

$$\left(\phi_t\right)_{i,j}^{n-1} = \frac{1}{6\Delta t}\left[2\phi_{i,j}^{n} + 3\phi_{i,j}^{n-1} - 6\phi_{i,j}^{n-2} + \phi_{i,j}^{n-3}\right] + O\left(\Delta t^3\right) \tag{3.17}$$

$$\left(\phi_t\right)_{i,j}^{n-2} = \frac{1}{6\Delta t}\left[-2\phi_{i,j}^{n-3} - 3\phi_{i,j}^{n-2} + 6\phi_{i,j}^{n-1} - \phi_{i,j}^{n}\right] + O\left(\Delta t^3\right) \tag{3.18}$$

A similar discretization with fourth-order accuracy leads to ϕ_t in the corrector step as

$$\left(\phi_t\right)_{i,j}^{n+1} = \frac{1}{12\Delta t}\left[25\phi_{i,j}^{n+1} - 48\phi_{i,j}^{n} + 36\phi_{i,j}^{n-1} - 16\phi_{i,j}^{n-2} + 3\phi_{i,j}^{n-3}\right] + O\left(\Delta t^4\right) \tag{3.19}$$

$$\left(\phi_t\right)_{i,j}^{n} = \frac{1}{12\Delta t}\left[3\phi_{i,j}^{n+1} + 10\phi_{i,j}^{n} - 18\phi_{i,j}^{n-1} + 6\phi_{i,j}^{n-2} + \phi_{i,j}^{n-3}\right] + O\left(\Delta t^4\right), \tag{3.20}$$

$$\left(\phi_t\right)_{i,j}^{n-1} = \frac{1}{12\Delta t}\left[-3\phi_{i,j}^{n-3} - 10\phi_{i,j}^{n-2} + 18\phi_{i,j}^{n-1} - 6\phi_{i,j}^{n} - \phi_{i,j}^{n+1}\right] + O\left(\Delta t^4\right), \tag{3.21}$$

$$\left(\phi_t\right)_{i,j}^{n-2} = \frac{1}{12\Delta t}\left[-25\phi_{i,j}^{n-3} + 48\phi_{i,j}^{n-2} - 36\phi_{i,j}^{n-1} + 16\phi_{i,j}^{n} - 3\phi_{i,j}^{n+1}\right] + O\left(\Delta t^4\right). \tag{3.22}$$

Substituting (3.16) - (3.18) into (3.11) and (3.12) eliminates the time derivatives of the cross terms in the predictor step of the momentum equations as

$$\begin{aligned} P_{i,j}'^{n+1} = P_{i,j}^{n} + \frac{\Delta t}{12}\Big[&23\left(F_1\right)_{i,j}^{n} - 16\left(F_1\right)_{i,j}^{n-1} + 5\left(F_1\right)_{i,j}^{n-2}\Big] \\ &+ 3\left(F_2\right)_{i,j}^{n} - 6\left(F_2\right)_{i,j}^{n-1} + 4\left(F_2\right)_{i,j}^{n-2} - \left(F_2\right)_{i,j}^{n-3} \end{aligned} \tag{3.23}$$

$$\begin{aligned} Q_{i,j}'^{n+1} = Q_{i,j}^{n} + \frac{\Delta t}{12}\Big[&23\left(G_1\right)_{i,j}^{n} - 16\left(G_1\right)_{i,j}^{n-1} + 5\left(G_1\right)_{i,j}^{n-2}\Big] \\ &+ 3\left(G_2\right)_{i,j}^{n} - 6\left(G_2\right)_{i,j}^{n-1} + 4\left(G_2\right)_{i,j}^{n-2} - \left(G_2\right)_{i,j}^{n-3} \end{aligned} \tag{3.24}$$

Similarly, substitution of (3.19) - (3.22) into (3.14) and (3.15) simplifies the integration in the corrector stage as

$$\begin{aligned} P_{i,j}'^{n+1} = P_{i,j}^{n} + \frac{\Delta t}{24}\Big[&9\left(F_1'\right)_{i,j}^{n+1} + 19\left(F_1\right)_{i,j}^{n} - 5\left(F_1\right)_{i,j}^{n-1} + \left(F_1\right)_{i,j}^{n-2}\Big] \\ &+ \frac{137}{144}\left(F_2'\right)_{i,j}^{n+1} - \frac{49}{72}\left(F_2\right)_{i,j}^{n} - \frac{1}{2}\left(F_2\right)_{i,j}^{n-1} + \frac{17}{72}\left(F_2\right)_{i,j}^{n-2} - \frac{1}{144}\left(F_2\right)_{i,j}^{n-3} \end{aligned} \tag{3.25}$$

$$Q_{i,j}^{\prime n+1} = Q_{i,j}^{n} + \frac{\Delta t}{24}\left[9\left(G_1^{\prime}\right)_{i,j}^{n+1} + 19\left(G_1\right)_{i,j}^{n} - 5\left(G_1\right)_{i,j}^{n-1} + \left(G_1\right)_{i,j}^{n-2}\right] + \frac{137}{144}\left(G_2^{\prime}\right)_{i,j}^{n+1} - \frac{49}{72}\left(G_2\right)_{i,j}^{n} - \frac{1}{2}\left(G_2\right)_{i,j}^{n-1} + \frac{17}{72}\left(G_2\right)_{i,j}^{n-2} - \frac{1}{144}\left(G_2\right)_{i,j}^{n-3} \tag{3.26}$$

This time-integration scheme determines the evolution variables P and Q from the governing equations.

3.2 Spatial Discretization

The governing equations contain the conservative form of the nonlinear shallow-water equations that handles flux-dominated processes including discontinuities. The finite volume method with a Godunov-type scheme imposes conservation laws over a control volume through a Riemann solver and provides the solution for smooth and discontinuous flows. A Riemann problem is a generalization of the one-dimensional dam-break flow defined by the nonlinear shallow-water equations and the discontinuous initial conditions

$$\mathbf{U} = \left(x,0\right) = \begin{cases} \mathbf{U}_{\mathrm{L}} & \text{if } x \le 0 \\ \mathbf{U}_{\mathrm{R}} & \text{if } x > 0 \end{cases}. \tag{3.27}$$

where $\mathbf{U}_{\mathrm{L}}$ and $\mathbf{U}_{\mathrm{R}}$ contain the flow depth and momentum defined to the left and right of the cell interface. Figure 3.2 illustrate the solution of the Riemann problem that includes four possible cases involving two shock waves, two rarefaction waves, and one rarefaction and one shock wave on either side of the initial discontinuity. There are a wide variety of solvers for this problem as documented by Brocchini & Dodd (2008). Wu & Cheung (2008) solve the Riemann problem using the homotopy analysis method and provide an explicit solution in all four cases. Since the time-integration scheme requires this solution over all cell interfaces at the predictor and corrector steps, an efficient algorithm can reduce the computation time significantly.

The evolution variables are defined at the cell centers with a piece-wise linear distribution within the cells. It is necessary to reconstruct the initial condition (3.27) on the two sides of the cell interface for the Riemann problem. According to Zhou *et al*. (2001), a reconstruction of the surface elevation instead of the flow depth reduces spurious oscillations over irregular bathymetry and ensures a well-balanced finite volume scheme. We adapted the fifth-order TVD (Total Variation Diminishing) reconstruction scheme from Kim & Kim (2005) to evaluate the initial values of η for the continuity equation and *HU* and *HV* for the momentum equation for the Riemann problem in (19). Let ϕ denote either η, *HU* or *HV*. The values at the left and right sides of each interface are given by

$$\phi^{L}_{i+1/2,j} = \phi_{i,j} + \frac{1}{60}\left(-2\overline{\Delta\phi}_{i-2,j} + 11\overline{\Delta\phi}_{i-1,j} + 24\overline{\Delta\phi}_{i,j} - 3\overline{\Delta\phi}_{i+1,j}\right) \tag{3.28}$$

$$\phi^{R}_{i+1/2,j} = \phi_{i+1,j} - \frac{1}{60}\left(-2\overline{\Delta\phi}_{i+3,j} + 11\overline{\Delta\phi}_{i+2,j} + 24\overline{\Delta\phi}_{i+1,j} - 3\overline{\Delta\phi}_{i,j}\right). \tag{3.29}$$

Similarly, the values at the top and the bottom of each interface are derived as

$$\phi^{T}_{i,j+1/2} = \phi_{i,j} + \frac{1}{60}\left(-2\overline{\Delta\phi}_{i,j-2} + 11\overline{\Delta\phi}_{i,j-1} + 24\overline{\Delta\phi}_{i,j} - 3\overline{\Delta\phi}_{i,j+1}\right) \tag{3.30}$$

$$\phi^{B}_{i,j+1/2} = \phi_{i,j+1} - \frac{1}{60}\left(-2\overline{\Delta\phi}_{i,j+3} + 11\overline{\Delta\phi}_{i,j+2} + 24\overline{\Delta\phi}_{i,j+1} - 3\overline{\Delta\phi}_{i,j}\right). \tag{3.31}$$

where $\overline{\Delta\phi}$ denotes the TVD values computed from quantities at the neighboring cell centroids. For example,

$$\overline{\Delta\phi}_{i,j} = \xi_{i,j}\left(r_{i,j}\right)\ 0.5\left[\left(\phi_{i,j} - \phi_{i-1,j}\right) + \left(\phi_{i+1,j} - \phi_{i,j}\right)\right], \tag{3.32}$$

in which $\xi_{ij}(r_{ij})$ is the SUPERBEE slope limiter (e.g., Toro, 2001):

$$\xi\left(r_{i,j}\right) = \begin{cases} 0 & \text{if} \quad r \le 0 \\ 2r_{i,j} & \text{if} \quad 0 \le r \le 0.5 \\ 1 & \text{if} \quad 0.5 \le r \le 1 \\ \min\left\{r_{i,j}, \xi_R\left(r_{i,j}\right), 2\right\} & \text{if} \quad r \ge 1 \end{cases}, \tag{3.33}$$

where

$$r_{i,j} = \frac{\left(\phi_{i+1,j} - \phi_{i,j}\right)}{\left(\phi_{i,j} - \phi_{i-1,j}\right)}\ ,\ \xi_R\left(r_{i,j}\right) = \frac{2}{1+r_{i,j}}. \tag{3.34}$$

Figure 3.1 shows the locations of the reconstructed variables. The reconstructed values of $\eta^L_{i+1/2,j}$ and $\eta^R_{i+1/2,j}$ are then added to the water depth $h_{i+1/2,j}$ to provide $H^L_{i+1/2,j}$ and $H^R_{i+1/2,j}$. In the same way, $\eta^T_{i,j+1/2}$ and $\eta^B_{i,j+1/2}$ together with $h_{i,j+1/2}$ lead to $H^T_{i,j+1/2}$ and $H^B_{i,j+1/2}$. The reconstructed values of $\left(HU\right)^L_{i+1/2,j}$ and $\left(HU\right)^R_{i+1/2,j}$ must be divided by $H^L_{i+1/2,j}$ and $H^R_{i+1/2,j}$ to give $U^L_{i+1/2,j}$ and $U^R_{i+1/2,j}$. Similarly, $\left(HV\right)^T_{i,j+1/2}$ and $\left(HV\right)^B_{i,j+1/2}$ require division by $H^T_{i,j+1/2}$ and $H^B_{i,j+1/2}$ respectively to provide the velocities $V^T_{i,j+1/2}$, and $V^B_{i,j+1/2}$. This requires a minimum water depth to account for dry cells. The model treats cells with a water depth smaller than 10^{-4} m as dry cells. The solution of a local Riemann problem provides the flow velocity and depth at each cell interface for the derivation of the flux and bathymetry source terms.

The Riemann solver has first-order characteristics. The respective flux and bottom gradient terms in (3.5), (3.6), and (3.7) are computed with a first-order scheme to ensure a stable and well-balanced solution without adding noise even with rapidly varying bathymetry

$$E\left(H,U,V\right)_{i,j} = -\frac{1}{\Delta x}\left[\mathbf{F}\left(\mathbf{U}_{i+1/2,j}\right) - \mathbf{F}\left(\mathbf{U}_{i-1/2,j}\right)\right] - \frac{1}{\Delta y}\left[\mathbf{G}\left(\mathbf{U}_{i,j+1/2}\right) - \mathbf{G}\left(\mathbf{U}_{i,j-1/2}\right)\right] - \left(\psi_C\right)_{i,j} \tag{3.35}$$

$$\begin{aligned} F_1\left(H,U,V\right)_{i,j} = &-\frac{1}{\Delta x}\left[\mathbf{F}\left(\mathbf{U}_{i+1/2,j}\right) - \mathbf{F}\left(\mathbf{U}_{i-1/2,j}\right)\right] - \frac{1}{2\Delta y}\left[\left(\overline{H}\overline{U}\overline{V}\right)_{i,j+1} - \left(\overline{H}\overline{U}\overline{V}\right)_{i,j-1}\right], \\ &+ \frac{1}{\Delta x} g\overline{H}\left[h_{i+1/2,j} - h_{i-1/2,j}\right] + \left(\psi_{M1}\right)_{i,j} - U_{i,j}\left(\psi_C\right)_{i,j} - \left(\tau_1\right)_{i,j} \end{aligned} \tag{3.36}$$

$$\begin{aligned} G_1\left(H,U,V\right)_{i,j} = &-\frac{1}{\Delta y}\left[\mathbf{G}\left(\mathbf{U}_{i,j+1/2}\right) - \mathbf{G}\left(\mathbf{U}_{i,j-1/2}\right)\right] - \frac{1}{2\Delta x}\left[\left(\overline{H}\overline{U}\overline{V}\right)_{i+1,j} - \left(\overline{H}\overline{U}\overline{V}\right)_{i-1,j}\right], \\ &+ \frac{1}{\Delta y} g\overline{H}\left[h_{i,j+1/2} - h_{i,j-1/2}\right] + \left(\psi_{M2}\right)_{i,j} - V_{i,j}\left(\psi_C\right)_{i,j} - \left(\tau_2\right)_{i,j} \end{aligned} \tag{3.37}$$

where $\overline{H}$, $\overline{U}$, and $\overline{V}$ are cell averages. The spatial derivatives in the dispersion terms are evaluated at the cell centroids with finite difference approximations of second order accuracy. Let ϕ denote U, V, (hU), and (hV). The first-order derivative is stated as

$$\left(\phi_{i,j}\right)_x = \frac{\phi_{i+1,j} - \phi_{i-1,j}}{2\Delta x} + O\left(\Delta x^2\right), \tag{3.38}$$

$$\left(\phi_{i,j}\right)_y = \frac{\phi_{i,j+1} - \phi_{i,j-1}}{2\Delta y} + O\left(\Delta y^2\right), \tag{3.39}$$

and the second order derivative is given by

$$\left(\phi_{i,j}\right)_{xx} = \frac{\phi_{i-1,j} - 2\phi_{i,j} + \phi_{i+1,j}}{\Delta x^2} + O\left(\Delta x^2\right), \tag{3.40}$$

$$\left(\phi_{i,j}\right)_{yy} = \frac{\phi_{i,j-1} - 2\phi_{i,j} + \phi_{i,j+1}}{\Delta y^2} + O\left(\Delta y^2\right). \tag{3.41}$$

The third order derivative, which is only present in the continuity dispersion term ψ_C, is evaluated by

$$\left(\phi_{i,j}\right)_{xxx} = \frac{-\phi_{i-2,j} + 2\phi_{i-1,j} - 2\phi_{i+1,j} + \phi_{i+2,j}}{2\Delta x^3} + O\left(\Delta x^2\right) \tag{3.42}$$

$$\left(\phi_{i,j}\right)_{yyy} = \frac{-\phi_{i,j-2} + 2\phi_{i,j-1} - 2\phi_{i,j+1} + \phi_{i,j+2}}{2\Delta y^3} + O\left(\Delta y^2\right). \tag{3.43}$$

Second-order approximations are also extended to the boundaries of the domain. The momentum dispersion terms ψ_{PI} and ψ_{QI} from (3.6) and (3.7) involve $(H_{i,j})_t$, which is explicitly obtained from the right side of the continuity equation (3.2) in terms of spatial derivatives only.

3.3 System of Equations

The explicit time-integration scheme accounts for the cross-derivative terms in the governing equations and provides the evolution variables H, P and Q in (3.13), (3.25),

and (3.26) via the Riemann solver. The momentum variables P and Q contain x and y derivatives of U and V respectively, which in turn can be solved independently from series of one-dimensional problems in the x and y directions.

Discretization of (2.48) and (2.49) as part of (3.3) and (3.4) respectively with a second-order central difference scheme gives systems of equations in terms of U and V respectively:

$$P_{i,j} = (HU)_{i,j} + H_{i,j} z_{i,j} \left[\frac{z_{i,j}}{2} \left(\frac{U_{i-1,j} - 2U_{i,j} + U_{i+1,j}}{\Delta x^2} \right) + \left(\frac{(hU)_{i-1,j} - 2(hU)_{i,j} + (hU)_{i+1,j}}{\Delta x^2} \right) \right] \quad (3.44)$$

$$Q_{i,j} = (HV)_{i,j} + H_{i,j} z_{i,j} \left[\frac{z_{i,j}}{2} \left(\frac{V_{i,j-1} - 2V_{i,j} + V_{i,j+1}}{\Delta y^2} \right) + \left(\frac{(hV)_{i,j-1} - 2(hV)_{i,j} + (hV)_{i,j+1}}{\Delta y^2} \right) \right]. \quad (3.45)$$

The central difference scheme only involves the adjacent cells of each grid and thus forms the following linear systems of equations

$$\begin{bmatrix} H^*_{i,j}C_{1,j} & H^*_{i,j}R_{1,j} & \vdots & \vdots & \vdots \\ H^*_{i,j}L_{2,j} & H^*_{i,j}C_{2,j} & H^*_{i,j}R_{2,j} & \vdots & \vdots \\ \vdots & H^*_{i,j}L_{3,j} & H^*_{i,j}C_{3,j} & \vdots & \vdots \\ \vdots & \vdots & \vdots & \vdots & H^*_{i,j}R_{N-1,j} \\ \vdots & \vdots & \vdots & H^*_{i,j}L_{N,j} & H^*_{i,j}C_{N,j} \end{bmatrix} \begin{bmatrix} U_{1,j} \\ U_{2,j} \\ \vdots \\ U_{N-1,j} \\ U_{N,j} \end{bmatrix} = \begin{bmatrix} P_{1,j} \\ P_{2,j} \\ \vdots \\ P_{N-1,j} \\ P_{N,j} \end{bmatrix}, \quad (3.46)$$

$$\begin{bmatrix} H^*_{i,j}C_{i,1} & H^*_{i,j}T_{i,1} & \vdots & \vdots & \vdots \\ H^*_{i,j}B_{i,2} & H^*_{i,j}C_{i,2} & H^*_{i,j}T_{i,2} & \vdots & \vdots \\ \vdots & H^*_{i,j}B_{i,3} & H^*_{i,j}C_{i,3} & \vdots & \vdots \\ \vdots & \vdots & \vdots & \vdots & H^*_{i,j}T_{i,N-1} \\ \vdots & \vdots & \vdots & H^*_{i,j}B_{i,N} & H^*_{i,j}C_{i,N} \end{bmatrix} \begin{bmatrix} V_{i,1} \\ V_{i,2} \\ \vdots \\ V_{i,N-1} \\ V_{i,N} \end{bmatrix} = \begin{bmatrix} Q_{i,1} \\ Q_{i,2} \\ \vdots \\ Q_{i,N-1} \\ Q_{i,N} \end{bmatrix}, \quad (3.47)$$

in which

$$C_{i,j} = z_{i,j} \left[\frac{1}{z_{i,j}} - \frac{z_{i,j}}{\Delta x^2} - \frac{2h_{i,j}}{\Delta x^2} \right] \text{ or } z_{i,j} \left[\frac{1}{z_{i,j}} - \frac{z_{i,j}}{\Delta y^2} - \frac{2h_{i,j}}{\Delta y^2} \right]; \quad (3.48)$$

$$L_{i,j} = z_{i,j}\left[\frac{z_{i,j}}{2\Delta x^2} + \frac{h_{i-1,j}}{\Delta x^2}\right], \tag{3.49}$$

$$R_{i,j} = z_{i,j}\left[\frac{z_{i,j}}{2\Delta x^2} + \frac{h_{i+1,j}}{\Delta x^2}\right], \tag{3.50}$$

$$B_{i,j} = z_{i,j}\left[\frac{z_{i,j}}{2\Delta y^2} + \frac{h_{i,j-1}}{\Delta y^2}\right], \tag{3.51}$$

$$T_{i,j} = z_{i,j}\left[\frac{z_{i,j}}{2\Delta y^2} + \frac{h_{i,j+1}}{\Delta y^2}\right], \tag{3.52}$$

where H_i^* is H_i^n in the predictor and $H_i'^{n+1}$ in the corrector step. The five vectors *C*, *L*, *R*, *T*, and *B* of the matrix equations (3.46) and (3.47) can be pre-calculated and used throughout the computation. The tri-diagonal matrices are symmetric and positive definite. A Thomas algorithm in Ferziger & Peric (2002) solves for the flow velocity ($U_i'^{n+1}$, $V_i'^{n+1}$) in the predictor and for (U_i^{n+1}, V_i^{n+1}) in the corrector step.

The numerical procedures include a number of steps starting with the reconstructions of η, *HU*, and *HV* for the initial conditions of the Riemann problem in (3.27). The explicit solver of Wu & Cheung (2008) provides the cell interface values for the evaluation of the flux and the bathymetry source terms for the predictor in (3.10), (3.23), and (3.24) from which an estimate of *H*, *P* and *Q* are evaluated. The flow velocity components *U* and *V* are then determined from the matrix equations (3.46) and (3.47). The procedure is repeated in the corrector step (3.13), (3.25), and (3.26) and the relative error is evaluated

$$\Delta f = \frac{\sum_i \sum_j \left| f_{i,j}^{n+1} - f_{i,j}'^{n+1} \right|}{\sum_i \sum_j \left| f_{i,j}^{n+1} \right|}, \tag{3.53}$$

where f^{n+1} and f'^{n+1} denote *H*, *U*, and *V* at the present and previous steps in the iteration. Since the predictor step provides very accurate estimates of the variables, the scheme usually converges to the prescribed tolerance of $\Delta f < 0.001$ in two iterations or less. As pointed out by Wei *et al.* (1995), the numerical solution might oscillate above the

tolerance for strong nonlinear problems. Thus, the solution proceeds to the next time step if the iteration error in the corrector, f^{n+1}, is larger than the error from the predictor, f'^{n+1}. Tests during the development stage of the model have confirmed such behavior occurs in very few cases. The time integration scheme has to satisfy the Courant-Friedrichs-Lewy condition

$$\Delta t = C_r \min\left[\frac{\Delta x}{\max\left[\left|U_{i,j}\right| + \sqrt{gH_{i,j}}\right]}, \frac{\Delta y}{\max\left[\left|V_{i,j}\right| + \sqrt{gH_{i,j}}\right]}\right], \tag{3.54}$$

where C_r is the Courant number between zero and one, thereby preventing the fastest wave from traversing more than one grid cell within a time step.

The model uses an adaptive time step, which is constantly being readjusted based on the maximum flow velocity. The variable time step violates the assumptions of the explicit time integration and the resulting error has to be tracked. The numerical error in the fourth-order multistep method can be estimated as

$$err = \frac{19\left|f_{i,j}^{n+1} - f_{i,j}^{\prime n+1}\right|}{270\Delta t}, \tag{3.55}$$

which must remain below the allowable tolerance

$$tol = \frac{\left|b_{i,j}^{n+1} - f_{i,j}^{n+1}\right|}{10\Delta t}, \tag{3.56}$$

where $b_{i,j}^{n+1}$ is the right hand side of (3.2) - (3.4) (Burdon & Faires, 2005). The time step is expected to change very little over the four steps in the time integration. Significant variations of Δt might only occur over several hundreds time steps. In the unlikely case of $err > tol$, the computation of the current time integration is repeated by a fourth-order Runge-Kutta method with a constant time step. The adaptive time step contributes significantly to a fast and stable numerical solution. Many nearshore models use a pre-defined time step derived from the maximum still water depth in the computational

domain. This, however, might underestimate the allowable maximum time step during most of the numerical computation. Further, a fixed time step might momentarily violate the Courant-Friedrichs-Lewy criterion for transient, local high-speed flows as often encountered during the wave breaking process and propagation over dry bed.

CHAPTER 4
WAVE BREAKING

Depth-integrated models do not describe overturning of the free surface and thus cannot fully reproduce the wave breaking processes. The use of conserved variables in the present governing equations allows approximation of breaking waves as discontinuous flows. This section summarizes the shock-capturing properties of the formulation in conserved variables and their implementation to describe breaking waves in Boussinesq-type models. The conventional eddy viscosity approach is adapted to the present formulation to provide an alternate treatment for wave breaking and a reference for comparison. The laboratory data of Ting & Kirby (1994) facilitates calibration and evaluation of the two approaches prior to their implementation.

4.1 Riemann Solver Approach

For wave breaking in shallow-water, the free-surface flow becomes an advection- or flux-dominated process. The governing equations expressed in conserved evolution variables (H, HU) show a fundamental difference to those based on non-conserved variables (η, U). Expanding the flux terms of the present momentum equation (2.42) in the x direction leads to

$$\frac{1}{H}(HU)_t + UU_x + VU_y + \frac{U}{H}(HU)_x + \frac{V}{H}(HU)_y + g\eta_x + \frac{U}{H}\psi_C + \frac{1}{H}\psi_M = 0, \tag{4.1}$$

whereas the momentum equation of Nwogu (1993) reads

$$\frac{1}{H}U_t + UU_x + VU_y + \frac{1}{H}g\eta_x + \frac{1}{H}\psi_M = 0, \tag{4.2}$$

where the dispersion term ψ_M is given by

$$\psi_M = H\frac{z_\alpha^2}{2}\left[U_{xxt} + V_{xyt}\right] + Hz_\alpha\left[\left(hU_t\right)_{xx} + \left(hV_t\right)_{xy}\right]. \tag{4.3}$$

It becomes obvious that the present evolution variables introduce a second set of flux and dispersion terms to the momentum equations. The flux term $(HU)_x$ is instrumental in enforcing momentum conservation under supercritical flows and the driving force for mass flux across discontinuities. The Riemann solution to the nonlinear shallow-water equations imbedded in the present governing equations defines the shock conditions and accounts for energy loss due to flow discontinuities. The parabolic non-hydrostatic part of the governing equations, however, cannot handle discontinuous flows. The governing equations balance amplitude dispersion with frequency dispersion as the free surface steepens, but the depth-integrated system breaks down when the wave is about to overturn. The surface profile does not reach a discontinuity for the Riemann solver to describe the energy dissipation associated with the breaking waves. Additional treatment is necessary to fully utilize the capabilities of the governing equations.

The imbalance between amplitude and frequency dispersion results in a local anomaly at the breaking location that might lead to numerical instability depending on the order of the dispersion terms, the numerical scheme, and most important, the grid size. When the grid is fine enough to resolve the leading edge of a steep wave, the dispersion terms might not be able to describe the physical processes and the large local gradients can lead to instabilities, which are often too strong to be overcome by numerical diffusion. If only a limited number of cells are available to describe a bore-shaped wave, this leads to underestimation of the local gradients and the resulting numerical diffusion might be able to control the numerical instabilities to avoid breakdown of the model. Although no special treatment is necessary to avoid numerical instabilities, the use of numerical diffusion is not a solution to the stability problem as the grid size must be determined on a trial-and-error basis and the results become grid size dependent. In practical

applications, the users expect a model to work under a wide variety of wave breaking conditions and provide stable and reliable results. It is necessary to develop a general approach to eliminate potential instabilities due to the dispersion terms and enable the imbedded shock-capturing structure in the governing equations to describe wave breaking.

Conventional approaches utilize a dissipative term to reduce the wave height prior to wave breaking as a way to avoid numerical instabilities. Since wave breaking in the surf zone is advection dominated, the present study considers an alternate approach by deactivating the dispersion terms to allow the Riemann solver to describe the breaking wave as a bore or hydraulic jump. The solution conserves momentum across the discontinuity and thus automatically accounts for the energy dissipation during the breaking process. The local momentum gradients, $(HU)_x$ and $(HV)_y$, provide a good indicator for the onset of wave breaking consistent with the flux-based formulation even for a slow-moving hydraulic jump. Wave breaking begins when

$$0.5[|(HU)_x|+(HU)_x] \geq B_1\sqrt{gH}\text{, or} \tag{4.4a}$$

$$0.5[|(HV)_y|+(HV)_y] \geq B_1\sqrt{gH}\text{,} \tag{4.4b}$$

where

$$\left[(HU)_{i,j}\right]_x = \frac{(HU)_{i+1/2,j} - (HU)_{i-1/2,j}}{\Delta x}\text{,} \tag{4.5a}$$

$$\left[(HV)_{i,j}\right]_y = \frac{(HV)_{i,j+1/2} - (HV)_{i,j-1/2}}{\Delta y}\text{,} \tag{4.5b}$$

and B_1 denotes the wave breaking criterion in terms of the shallow-water celerity. It is a calibration coefficient determined from laboratory experiments. The use of (4.4) instead of $(HU)_x$ and $(HV)_y$ accounts for the direction of the flow and rules out wave breaking

behind the crest, where large momentum gradients might occur in short period waves. Even though $(HU)_x$ and $(HV)_y$ are strictly not velocity terms, the calibration with laboratory data would define their relations to the velocity for the wave-breaking criterion. In addition, it is not straightforward to compute the flow velocity from the momentum, when the flow depth H approaches zero on dry bed. Cross-directional momentum gradients, such as $(HU)_y$ and $(HV)_x$, are generally smaller than the x or y gradients and are not taken into account in this approach. Though a breaking event might occur in only one horizontal direction, the dispersion terms are locally deactivated in both directions. Since the Riemann solver used in this study is exact, the solution over the breaking cells satisfies exact conservation laws of mass and momentum. This provides a robust solution over an area, which is often the source of instabilities. Since the local variables in the resulting nonlinear shallow-water equations do not contain mixed time and space derivatives, the rank of the matrix equations (3.52) and (3.53) is reduced accordingly.

The present approach is based on the fact that the flow is flux dominated and non-hydrostatic effects are negligible near the breaking wave. The Boussinesq-type equations locally reduce to the nonlinear shallow-water equations for the shock-related hydraulic processes, while the waves in the rest of the domain remain dispersive. Local deactivation of dispersion terms along the breaking wave front automatically eliminates any source of high frequency contribution, which might give rise to instabilities. This approach is valid for waves breaking in shallow water including the swash zone, but it has limitations for wave breaking at intermediate water depth. Such a scenario might occur when superposition of two or more waves leads to rapid steepening and breaking of the free surface analogous to freak or sneak wave generation. Local deactivation of the dispersion terms over the steep wave front would terminate not only the potential

instability but also the dispersion of the underlying wave train. One way to work around this issue would be reconstruction of the dispersion terms at the breaking wave front from neighboring cells. However, the dispersion terms over irregular bathymetry do not necessarily follow the free surface profile for meaningful interpolation over the gap.

4.2 Eddy Viscosity Approach

For governing equations formulated in primitive variables, a wave-breaking model not only has to control potential instabilities along the steep wave front, but also has to account for momentum conservation across flow discontinuities. There are numerous semi-empirical approaches originated from the eddy viscosity concept of von Neumann & Richtmyer (1950) to stabilize shock fronts in the Euler equations. The idea was later used by Smagorinsky (1963) to parameterize the effect of unresolved subgrid-scale processes in an ocean circulation model under the assumption that the eddy viscosity is directly proportional to the horizontal gradient of the velocity. Heitner & Housner (1970) implemented the eddy viscosity approach to approximate energy dissipation due to wave breaking. Zelt (1991) and Kennedy *et al*. (2000) adapted this idea to account for wave breaking in Boussinesq-type models.

Adaptation of the approach of Heitner & Housner (1970) for the present formulation with conserved variables leads to the following dissipation terms

$$R_{Bx} = \left[\upsilon_1 (HU)_x\right]_x + \frac{1}{2}\left[\upsilon_1\left((HU)_y + (HV)_x\right)\right]_y, \tag{4.6a}$$

$$R_{By} = \left[\upsilon_2 (HV)_y\right]_y + \frac{1}{2}\left[\upsilon_2\left((HV)_x + (HU)_y\right)\right]_x, \tag{4.6b}$$

where υ_1 and υ_2 are the eddy viscosity calibrated to describe energy dissipation in the breaking process. The dissipation terms (4.6a) and (4.6b) are simply added to the left

hand sides of the momentum equations (2.42) and (2.43) respectively. Kennedy *et al.* (2000) use a velocity indicator derived from η_t to determine the eddy viscosity. Consistent with the present formulation, the eddy viscosities are given by

$$\upsilon_1 = -\Psi_1 H\left|(HU)_x\right| , \tag{4.7a}$$

$$\upsilon_2 = -\Psi_2 H\left|(HV)_y\right|, \tag{4.7b}$$

in which

$$\Psi_1 = 1 - \frac{(HU)_x}{B_1\sqrt{gH}} \text{ for } \left|(HU)_x\right| \geq B_2\sqrt{gH} \tag{4.8a}$$

$$\Psi_2 = 1 - \frac{(HV)_y}{B_1\sqrt{gH}} \text{ for } \left|(HV)_y\right| \geq B_2\sqrt{gH} \tag{4.8b}$$

where B_1 and B_2 denote the onset and termination of the wave-breaking process in terms of the shallow-water celerity and must be calibrated through laboratory experiments. The onset and termination criteria enable gradual energy dissipation through the momentum equation over time and distance from the initial steepening of the surface to the reduction of the wave height after wave breaking. In contrast, the Riemann solver approach uses only one criterion to deactivate the dispersion terms for energy dissipation through a flow discontinuity. Both approaches provide a mechanism to eliminate instabilities associated with the dispersion terms prior to wave breaking. The former dissipates the energy over a larger area analogous to turbulence dissipation, whereas the latter describes dissipation of energy locally at the steep wave front through bore formation.

For illustration and comparison, this study considers the eddy viscosity approach in one-dimensional problems in the x direction only. Consistent with the flux-based formulation, the local momentum gradient $(HU)_x$ is used to determine the eddy viscosity and the wave breaking criterion. Equations (4.6) - (4.8) become

$$R_B = \left[\upsilon (HU)_x\right]_x, \tag{4.9}$$

$$\upsilon = -\Psi H \left|(HU)_x\right| , \tag{4.10}$$

$$\Psi = 1 - \frac{(HU)_x}{B_1\sqrt{gH}} \text{ for } \left|(HU)_x\right| \geq B_2\sqrt{gH} . \tag{4.11}$$

Wave energy dissipation associated with breaking begins when $|(HU)_x| \geq B_1\sqrt{gH}$ and continues as long as $|(HU)_x| \geq B_2\sqrt{gH}$. Since this approach involves both the onset and termination criterion, a proper indexing system has to track each breaker individually. The same approach as in (4.4) is applied to avoid activation of wave breaking cells at the back of the wave. The largest momentum gradients occur at the steep wave face or hydraulic jump where wave breaking initiates. Air entrainment and white water turbulence follows. The breaking term stays active for a duration equal to T^*, accounting for the continuing dissipation process behind the broken waves, where the momentum gradient would not exceed the breaking thresholds. This also prevents development of unrealistic kinks at the tip of the wave faces by distributing the energy dissipation in time and along the wave train. Kennedy *et al*. (2000) found $T^* = T_C\sqrt{H/g}$ to be applicable for a wide range of wave conditions. For plunging breakers, the momentum gradient far exceeds the breaking thresholds along the entire wave face resulting in large initial energy dissipation over a number of grid cells. Air entrainment and turbulence resulting from the overturning wave remain as the wave propagates forward. The breaker index would keep the previously assigned breaking cells active for the duration T^*. The eddy viscosity term would consequently affect a larger part of the wave from the front to the back. Under spilling wave conditions, the breaking process is less intense without major overturning of the free surface. Hence, fewer cells in the upper part of the wave face would pass the breaking threshold. This will also result in fewer cells affected by the index and more gradual energy dissipation.

It is worth mentioning that the eddy viscosity approach is suitable for the Boussinesq-type models formulated in non-conserved variables. The imbedded momentum term $(HU)_x$ helps to overcome the missing momentum conservation locally during the wave breaking process and to account for shock propagation under supercritical flow conditions. However, the dissipation term has to act over a large area around the breaking wave and that might smear out the physical character of any subsequent bores propagating over an extended distance.

4.3 Model Calibration

Both the Riemann solver and eddy viscosity approaches involve empirical parameters that require calibration with laboratory experiments. Ting & Kirby (1994) provided laboratory data for 0.125-m high incident waves in 0.4 m water depth with 2 and 5 s period. The incident cnoidal waves transform into spilling and plunging breakers on a 1:35 slope. These test cases provide a valuable dataset for calibration of the present concept as it has been in the past for other depth-integrated wave-breaking models (e.g., Madsen *et al*., 1997; Bredmose *et al*., 2004; Sørensen *et al*., 2004; Lynett, 2006).

The Riemann solver approach uses the coefficient B_1 to define the threshold for deactivation of the dispersion terms. The predefined coefficient must work reliably for both spilling and plunging wave breakers. We consider a computational domain of 40 m with a 0.025-m grid. The incident cnoidal waves, which are generated at the left boundary, propagate over a distance of 20 m before reaching the toe of the 1:35 beach. Figure 4.1 compares the laboratory data for spilling and plunging breakers with computed results for B_1 = [0.4; 0.5; 0.6]. The comparison includes the crest and trough envelopes as well as the wave setup. The three thresholds deactivate the dispersion terms at different stages and over different amounts of cells during the wave breaking process. The overall

results from all three thresholds are very similar for both spilling and plunging waves indicating that the results are not very sensitive to the calibration coefficient. The model reproduces the wave breaking location, but underestimates the initial breaking wave height due to deactivation of the dispersion terms, which are responsible for the steepening of the wave front to balance the flux terms. Because dissipation only occurs locally at the portion of the wave face exceeding the threshold, the model underestimates the overall dissipation in the adjacent area where turbulence and air entrainment might be important. In addition, the abrupt termination of the dispersion terms generates a small local peak at the wave front resulting in overestimation of the wave height and under prediction of the setup in the surf zone. Close to the beach, the momentum gradient is lower than the breaking thresholds for all three parameters and, as a consequence, the dispersion terms maintain active. At this stage, the dispersion terms do not cause instabilities anymore and the model continues the wave breaking process. The overall agreement between the numerical and laboratory data is reasonable.

Since the depth-integrated model cannot describe overturning of the free surface, the computed crest elevation does not fully reproduce the laboratory data for the range of B_1 considered. It is also difficult to measure precisely the surface elevation of the overturning waves and the subsequent splash up in the laboratory experiment. The computed crest envelope shows that the onset parameter B_1 is responsible for the location and timing of the breaking process. A small value of B_1 causes the waves to break early, but does not adversely affect the rest of the results. A large value of B_1 delays the breaking process and causes unrealistic steepening of the wave face. For both spilling and plunging breakers, the breaking wave height is best accounted for by using $B_1 = 0.6$. The high threshold, however, delays deactivation of the dispersion terms prior to wave breaking and allows dispersion in the waves close to shore leading to larger deviation

with the laboratory data. The coefficient B_1 = 0.4 produces the lowest breaking wave height, but slightly lower wave heights in the inner surf zones. The value of B_1 = 0.5 appears to provide the best compromise on the onset and duration of wave breaking for subsequent applications. It is worth to mention that this calibration includes long-period cnoidal waves, which possess characteristics of solitary waves as well.

The eddy viscosity model involves the calibration coefficients B_1 and B_2 defining the onset and termination of the wave-breaking process in terms of the shallow-water celerity $\sqrt{gH}$. The calibration is carried out with the same laboratory dataset. Figure 4.2 compares the computed and laboratory data for six combinations of B_1 and B_2 in the spilling case. The choice of B_1 affects the breaking wave height and slightly modifies the wave setup profile, but produces little effect on the wave trough elevation. The termination parameter B_2 does not influence the overall results for the range considered. For this particular test case, good agreement with the laboratory data is obtained with B_1 = 0.5 and $0.1 \leq B_2 \leq 0.25$. Figure 4.3 shows the comparison for the plunging case. The best agreement is obtained for B_1 = 0.6, which corresponds to the onset of breaking at a higher speed in comparison to the spilling breaker. This is consistent with the higher flow speed and surface elevation developed prior to a plunging breaker. The termination parameter is sufficiently low to ensure a continuous breaking process until most of the wave energy is dissipated. Additional tests with both spilling and plunging wave breakers have shown a deviation of the computed crest envelope from the experimental data towards the end of the breaking process for $B_2 > 0.25$ due to the breaking term being applied to an insufficient number of grid cells. The trough elevation is set by the initial wave height and period and has little to do with the breaking parameters. The wave setup results from the excess of momentum in the surf zone and the computed and measured data agrees in both test cases. Overall, B_1 = 0.5 and B_2 = 0.15 provide the best

compromise between the spilling and plunging wave breakers.

The calibration has demonstrated that the eddy viscosity approach with two coefficients better reproduces the laboratory data. Its extension to the two-dimensional horizontal plane is not straightforward. Depending on the angle of approach and the local bathymetry, wave breaking is a dynamic process and the breaker has many configurations. The breaking wave front may simultaneously advance forward and laterally as seen at a surfing site. Apart from the validity of the dissipation mechanism empirically predefined for uni-directional waves, tracking of the individual breakers is a challenging task in the two-dimensional horizontal plane. Each wave would have to be indexed and tracked as it propagates across the surf zone. A tracking algorithm has to work reliably for all possible breaking scenarios, but there is no guarantee that all breaking processes over complex bathymetry can be detected. The Riemann solver approach determines the breaking threshold using one coefficient without the need for a tracking mechanism. Since the numerical model uses analytical solutions of all admissible wave breaking conditions and their combinations over a number of cells to construct a wave-breaking scenario, it is more amendable to situations not seen in the calibration process. Hence, the subsequent analysis uses the Riemann solver approach with local deactivation of the dispersion terms to account for wave breaking.

CHAPTER 5
VERIFICATION AND VALIDATION

This dissertation introduces conserved variables into the Boussinesq-type equations and obtains the solution through a conservative numerical scheme analogous to that of the nonlinear shallow-water equations. While the linearized governing equations retain the original dispersion and shoaling characteristics, it is still necessary to verify the numerical scheme and its capability in handling these processes under nonlinear conditions through a series of numerical experiments. These include an examination of the linear dispersion characteristics and test cases for head-on solitary wave collision in a straight channel and sinusoidal wave transformation over a submerged bar. In addition, the use of the proposed reference depth versus the original approach of Nwogu (1993) is examined more closely in the wave transformation experiment. The implementation of a Riemann solver to describe breaking waves in Boussinesq-type equations also needs validation. The standard test cases of solitary wave runup on a plane beach and a conical island allow validation of the model for both wave breaking and runup.

5.1 Linear Dispersion

The reference depth z at which the velocity is evaluated has a significant impact on the dispersion characteristics of the Boussinesq-type equations of Nwogu (1993) and their applicability to wave propagation over a range of water depths. He determined an optimal value of $z_\alpha = -0.5374h$ to provide the best overall dispersion characteristics for $0 < h/L_o < 0.5$. While the present governing equations retain the same dispersion characteristics, it is necessary to confirm that the numerical scheme would work for the same value of z_α despite truncation errors in the spatial derivatives and time integration.

By setting $z_\alpha = -0.5374h$ as a demonstration, a numerical experiment with small amplitude waves would identify the same optimal value of z_α as Nwogu (1993) to reproduce the celerity from the linear dispersion relation. The computational domain is 1.0 m deep and 120 m long with a grid size $\Delta x = 0.012$ m. A wavemaker at the left boundary generates periodic waves of small amplitude $A = 0.01$ m towards the open boundary at the right. The input periods were selected to produce wavelengths between 2 m and 10 m with $-0.56253 < z_\alpha/h < -0.51253$ at $z_\alpha/h = 0.0025$ increments. The zero up-crossing method identifies the average wavelength for computation of the celerity. Figure 5.1 shows the ratio of the computed and linear celerity over a range of h/L_o up to 0.5. The overall optimum value of z_α/h is found by minimizing the sum of the relative errors between the computed and analytical values of h/L_o. A minimum relative error of 0.012 occurs over the range of h/L_o for $z_\alpha/h = -0.53503$, which is close to the analytical value of $z_\alpha/h = -0.5374$ from Nwogu (1993). This confirms that the numerical scheme does not alter the dispersion characteristics of the governing equations.

5.2 Head-on Collision of Two Solitary Waves

A common test for Boussinesq-type and non-hydrostatic models is the propagation of solitary waves in a long, frictionless channel of constant depth (Wei & Kirby, 1995; Li & Raichlen, 2002; Stelling & Zijlema, 2003; Yamazaki *et al*., 2009). The solitary wave is a single symmetric pulse above the still water level characterized by an exact balance of nonlinearity and dispersion. Since a solitary wave involves actual mass flux, it can be seen as a dispersive shallow-water wave, thereby making this test suitable for nearshore models. The uniform channel allows examination of the balance between nonlinearity and dispersion without interference from additional nonlinear effects due to irregular bathymetry. The numerical model must handle the equilibrium between amplitude and frequency dispersion to propagate the wave profile at constant shape and speed. Typical

problems during propagation often involve trailing edge dispersion consequently causing reduction in wave height and celerity. Those phenomena mostly arise from approximation errors in the governing equations with respect to nonlinearity and dispersion or a combination of numerical errors from poorly balanced schemes and truncation of numerical approximations.

The numerical experiment simulates two solitary waves with an initial height of $A/h = 0.3$ propagating in opposite directions in a channel. Their collision presents additional challenges to the model by a sudden change of the nonlinear and frequency dispersion characteristics. In theory, the two solitary waves maintain their original identity after passing each other. The computation uses a grid spacing of $\Delta x/h = 0.1$ and a Courant number of $C_r = 0.4$ resulting in a time step of $\Delta t\sqrt{g/h} = 0.028$. The channel is $300h$ long and the initial position of the solitary waves is at $x/h = 35$ and $x/h = 265$. Figure 5.2 shows the simulated surface profiles at $t\sqrt{g/h} = 0$, 101.2, and 200. Due to incompatibility between the analytical and numerical solutions, it takes about 150 time steps for the model to adjust to a steady free surface profile of approximately $A/h = 0.31$. At $t\sqrt{g/h} = 101.2$, the solitary waves align at their peaks. Local nonlinear interactions occur and give rise to a wave height of $A/h = 0.65$. At $t\sqrt{g/h} = 200$, the wave profiles are almost identical to the initial solitary waveform with a slight reduction of amplitude to $A/h = 0.30$.

The total reduction in wave height between the numerically adjusted profiles at $t\sqrt{g/h} = 21$ and the final stage at $t\sqrt{g/h} = 200$ is $A/h = 0.01$. The average celerity of the numerical solution is 0.3% lower than the analytical celerity resulting in a small phase lag of the computed solitary waves and the analytical solution. The test demonstrates the capability of the proposed numerical procedure to handle the strong nonlinearity and dispersion of solitary waves and maintain stable and accurate results even after long

computations. Nwogu (1993) compared the quadratic transfer function of the linearized form of his equations with second-order Laplace equation and pointed out that nonlinear effects can reasonably be accounted for up to $A/h \sim 0.3$. This test shows the numerical approach provides acceptable and stable solutions for nonlinear and dispersive waves beyond the range of the model's intended applicability. This supports the use of the proposed reference depth to potentially enhance the dispersion characteristics of Nwogu's (1993) Boussinesq-type equations.

5.3 Periodic Wave Propagation over a Submerged Bar

Beji & Battjes (1992) and Luth *et al*. (1994) described a series of laboratory experiments to investigate wave propagation and dispersion over a submerged bar. Figure 5.3 shows a schematic of the 37.7 m long, 0.8 m wide, and 0.75 m high flume with a 0.3 m high trapezoidal bar at 6 m from a piston-type wavemaker. The bar has a 1:20 offshore slope followed by a 2-m crest and a 1:10 back slope. A gravel beach at the end of the flume acts as a wave absorber. Waves shoal when propagating up the slope of the bar forcing development of bound higher harmonics, which are then released from the carrier frequency on the lee side of the bar as the water depth parameter kh increases rapidly. Bar-type features are quite common in coastal waters making this study an important test case for nearshore models. Many Boussinesq-type or non-hydrostatic models do not fully resolve the higher harmonics due to low-order approximation of nonlinearity and dispersion in the governing equations. This provides a good test case for the use of the proposed reference depth versus the original approach of Nwogu (1993).

The present study focuses on test cases A and C of their experiment that involve sinusoidal incident waves with 1 cm amplitude (A) and 2.02 sec period and with 2.05 cm amplitude and 1.01 sec period respectively. Both tests were conducted in 0.4 m of water

producing $kh \approx 0.67$ and $A/L_o \approx 0.0054$ in case A and $kh \approx 1.7$ and $A/L_o \approx 0.0276$ in case C. The model consists of a 35-m long flume with $\Delta x = 0.012$ m and a Courant number $C_r = 0.4$. A wavemaker at the left boundary generates the incident waves and a 6-m long sponge layer dissipates the outgoing waves at the right boundary. Figure 5.4 shows the results for case A. The numerical model maintains good agreement with the experimental data at stations 4 to 8 over the bar. With the z_α proposed by Nwogu (1993), minor discrepancies arise behind the bar at stations 9, 10, and 11, where higher harmonics are released. A spectral analysis shows evidence of fourth and fifth-order free harmonics of $6 > kh > 10$, which cannot be fully resolved by the present governing equations. These higher harmonics, however, do not contain significant energy to affect the overall performance of the model. The use of the proposed reference depth appears to capture most of these low-energy higher harmonics.

The results from case C are illustrated in Figure 5.5. Because of the larger value of kh, the waves maintain a typical cnoidal profile over the crest and do not release the higher harmonics until propagating over the back slope. The model results match the measured data well over the bar with only minor phase shifts despite the strong nonlinearity. The largest discrepancy can be seen at gauge 10 where nonlinear, higher order dispersive waves arise over the back slope of the bar. With Nwogu's (1993) $z_{\alpha,}$ the model does not properly describe the strong second and third-order free harmonics at $kh \approx 6$ and 14 behind the bar. The proposed value of z_α helps to at least account for the second harmonics and reproduce the overall waveforms over and behind the bar. In addition to case A, this test shows the model's capabilities in handling wave conditions that are well beyond the applicable range of the governing equations and providing stable results. The model's errors in describing highly nonlinear dispersive waves are small, provided the main energy is contained in waves not far exceeding $kh \approx 5$. It should also be noted that

part of the discrepancy between laboratory data and model results might be due to the experimental setup, since the gravel beach in the laboratory experiment might not act as a perfect wave absorber.

5.4 Solitary Wave Runup on a Plane Beach

Solitary wave runup on a plane slope is one of the most intensively studied problems in long-wave modeling. In particular, the laboratory experiments of Hall & Watts (1953) and Synolakis (1987) have provided frequently used data for validation of wave breaking and runup models (e.g., Zelt, 1991; Titov & Synolakis, 1995; Lynett *et al*., 2002; Li & Raichlen, 2002; Wei *et al*., 2006; Yamazaki *et al*., 2009). Figure 5.6 shows a schematic of the experiment with A indicating the initial solitary wave height, R the runup, and β the beach slope. The numerical model runs with a Courant number C_r = 0.4 and a grid size $\Delta x/h$ = 0.1 for all the tests. A Manning coefficient n = 0.01 s/m$^{1/3}$ defines the surface roughness of the smooth glass beach in the laboratory experiment. The initial solitary wave location is at x/h = -20 from the beach toe allowing the initial wave profile to adjust to the governing equations before reaching the slope.

The runup on a beach with β = 19.85 and a wave height A/h = 0.3 is first examined. Figure 5.7 compares the measured surface profiles and the model results. Different from nonlinear shallow-water models, which lack dispersive terms, the present model reproduces the shoaling process up to $t\sqrt{g/h} = 20$ at the onset of a plunging breaker as observed in the laboratory experiment. With the conserved variables, the model mimics the three-dimensional breaking process as a collapsing bore and conserves the flow volume and momentum during the process. The resulting surge reaches the maximum elevation of R/h = 0.55 around $t\sqrt{g/h} = 40$. The model shows a minor discrepancy with the laboratory data starting around $t\sqrt{g/h} = 50$, when a hydraulic jump begins to develop

from the drawdown. This may be due to the complex two-dimensional flow structure in the vertical plane that the depth-integrated model cannot fully capture. Since the computed results agree with the measured data toward the end, the local disagreement might also be due to instrumentation errors. The drawdown process introduces air entrainment in the water column and splashes at the surface that are difficult to measure by any instrument.

Figure 5.8 plots the measured and computed runup as a function of the initial solitary wave height A/h for beach slopes of 1:19.85, 1:15, and 1:5.67. The data shows good agreement over a wide range of breaking and non-breaking events characterized by a bilinear distribution with a distinct transition. For the 1:19.85 and 1:15 slopes, the data to the right of the transition represents plunging breakers, whereas the relatively steep slope of 1:5.67 produces surging waves without flow discontinuities or breaking. The model is able to simulate the runup for incident wave heights of up to $A/h = 0.7$, which is beyond the model's range of nonlinearity. The tests prove the validity of the use of the Riemann solver for wave breaking in Boussinesq-type models. The results are stable without artificial smoothing or filtering and are not grid sensitive.

5.5 Solitary Wave Transformation around a Conical Island

Transformation of long waves around an island has attracted a lot of attention in the research community. Refraction and diffraction of long waves may result in significant inundation on the lee side and trapping of energy around an island. During the Flores Island tsunami in 1992, the circular shaped Babi Island experienced unexpectedly large runup on the leeside (Liu *et al.*, 1991, Liu *et al.*, 1995a,b; Yeh *et al.*, 1996). Similar impacts were observed at a small island during the Okushiri Island tsunami in 1993 (Cho, 1995) and more recently during the Great Indian Ocean tsunami at Car Nicobar Island near the Sumatra-Andaman earthquake source region (Choi *et al.*, 2005). In addition, Munger & Cheung (2008) and Roeber *et al*. (2010) reported trapped waves with resonance amplification around the Hawaiian and Samoan Islands. A common observation is that waves refract around an island on the two sides, collide in the back with additional energy from the diffracted waves, and continue to wrap around the island.

Briggs *et al.* (1995) conducted a large-scale laboratory experiment to investigate solitary wave transformation around a conical island. The collected data has become a standard for validation of runup models in the tsunami community (Liu *et al.*, 1995a; Titov & Synolakis, 1998; Wei *et al.*, 2006, Yamazaki *et al*., 2009), but also for Boussinesq-type models (Chen *et al.*, 2000; Lynett *et al.*, 2002). Figure 5.9 shows schematics of the laboratory experiment. The basin is 25 m by 30 m. The circular island has the shape of a truncated cone constructed of concrete with diameters of 7.2 m at the bottom and 2.2 m at the top. The island is 0.625 m high and has a side slope of 1:4. A 27.4-m long directional wave maker consisting of 61 paddles generates the input solitary waves for the laboratory test. Wave absorbers at the three remaining sidewalls reduce reflection in the basin.

The experiment covers the water depths h = 0.32 and 0.42 m and the solitary wave heights A/h = 0.05, 0.1 and 0.2. The present study considers the smaller water depth h = 0.32 m, which provides a more challenging test case for dispersive models. In the computation, the solitary wave is generated from the left boundary with the measured incident wave heights of A/h = 0.045, 0.096, and 0.181. These measured wave heights, instead of the target wave heights A/h = 0.05, 0.1, and 0.2 in the laboratory experiment, better represent the recorded data at gauge 2 and thus the incident wave conditions to the conical island. The radiation condition is imposed at the lateral boundaries to account for the effects of the wave absorbers. While the radiation condition acts as an open boundary condition for low frequency waves, the laboratory wave absorbers partially eliminate the incoming wave signal. The model is set up with a grid of $\Delta x = \Delta y$ = 5 cm. A Manning's roughness coefficient n = 0.014 s/m$^{1/3}$ accounts for the smooth concrete finish according to Chaudhry (1993). The time step constraint is set to C_r = 0.4. Figure 5.10 shows a series of snapshots as the solitary wave with A/h = 0.181 propagates around the island. The result shows the maximum runup at the front and refraction and trapping of the solitary wave over the island slope. The trapped waves from the two sides superpose with the diffracted wave on the leeside of the island. Wave breaking occurs around the island according to Titov & Synolakis (1998) and reduces the runup particularly on the leeside of the island. After the solitary wave passes the island, the trapped waves continue to wrap around to the front.

A number of gauges recorded the transformation of the solitary wave around the conical island. Figure 5.11 shows the time series of the solutions and the measured free surface elevations at selected gauges. With reference to Figure 5.9, gauges 2 and 6 are located in front of the island and 9, 16, and 22 are placed close to the still waterline at 0°, 270°, and 180° around the island. These gauges provide sufficient coverage of the wave conditions

important to the experiment. The measured data at gauge 2 provides a reference for adjustment of the timing of the computed waveforms. The results show the incident wave profile and reflection from the island. With higher nonlinearity, the crest of the solitary wave is narrower and the reflection is more distinct. Wave breaking was observed at gauge 9 for A/h = 0.181 and 0.096. The model accurately describes the subsequent drawdown in all three cases, but just like most published models, does not reproduce the small amplitude short period waves afterwards. A careful inspection of the laboratory setup shows the wavemaker is 2.6 m shorter than the basin width and diffraction of the incident wave at the two ends of the wavemaker likely generated these short period waves in all three cases. For A/h = 0.181, the wave breaks as it wraps around the island and the model approximates the wave breaking process as bores resulting in steep front faces. The waves wrapped around from the two sides superpose and break symmetrically as if it is a standing wave. This is a classical example of the two-shock interaction in the Riemann solver used in the present model. Most empirical wave breaking mechanisms cater to typical spilling and plunging wave breakers such as those examined by Ting & Kirby (1994) and might not correctly account for these conditions. Figure 5.12 compares the measured data and the computed inundation in its original resolution around the conical island. The computed results show good agreement with the laboratory data and are symmetric about the wave propagation direction despite the use of a Cartesian grid to describe curved surfaces.

This chapter has documented standard verification and validation tests for wave transformation models in the literature. The overall agreement between the computed results and laboratory data demonstrates the capability of the present model to estimate wave transformation, breaking, and inundation in the two horizontal dimensions.

CHAPTER 6
LABORATORY EXPERIMENTS

6.1 Background

Laboratory experiments are always a crucial component in scientific research. The controlled environment in a laboratory enables researchers to accentuate certain processes for thorough examination and for model validation. Many laboratory studies for long waves have focused on runup of solitary waves on a plane slope (e.g.: Hall & Watts, 1953; Synolakis, 1987; Li & Raichlen, 2002; Chang *et al*., 2009). The tsunami modeling community frequently uses these experiments for model validation. The measured runup data on a straight slope can be a valid test for the moving boundary scheme of a numerical model. Although these experiments involve wave breaking in most cases, the breaking events occur over a short period of time near the initial waterline and cannot truly validate the shock-capturing capabilities of a model. In fringing reef environments, numerical models need to describe propagation and decay of flow discontinuities over an extended lagoon.

Limited laboratory data pertaining to the detailed hydraulics and wave processes over reef-type bathymetry exists in the literature. Most previous laboratory experiments utilized monochromatic or narrow-banded waves to investigate integrated processes over fringing reefs such as wave setup and setdown (e.g., Seelig, 1983; Gourlay, 1996a,b; Skotner & Apelt, 1999). A recent laboratory study by Nwogu & Demirbilek (2010) focused on transfer of spectral energy during the breaking process and development of infragravity waves over fringing reefs. However, these laboratory studies do not characterize the flow conditions on the time-scale of the individual waves for validation of the flow kinematics. For example, very little experimental data relates to the wave

breaking, bore formation, and the hydraulic processes over a fringing reef that can affect the subsequent coastal inundation, scouring of foundations, and loading on coastal structures. Such data is necessary for understanding and characterization of the physical processes involved in wave transformation over fringing reefs for validation of numerical wave models.

A laboratory experiment for validation of nearshore wave models in fringing reef environment shall include processes related to breaking, bore formation, and dispersion with a sufficient scale. Such experiments should utilize high amplitude solitary waves and a lagoon of constant water depth to accentuate these processes for a deterministic assessment. This allows investigation of transitions between sub- and supercritical flows as well as bore propagation over a lagoon for an extended period of time.

6.2 Laboratory Facility

A National Science Foundation grant enabled performance of large-scale flume experiments pertaining to wave transformation over fringing reefs at the O.H. Hinsdale Wave Research Laboratory, Oregon State University (OSU). The test facility is a National Science Foundation designated site for tsunami research within the Network for Earthquake Engineering Simulation. Two series of experiments were conducted in fall 2007 and summer 2009.

The first series of experiments was carried out in two-dimensional flumes constructed in the Tsunami Wave Basin (TWB), which is 48.8 m long, 26.5 m wide, and 2.1 m high. The wave maker consists of 29 individual paddles of 0.905 m width and 2.0 m height each attached to a piston driven by an electric motor. A silicon band caulks the seams between adjacent paddles and the tank walls. The motors, which are mounted to a fixed steel frame, move the paddles with a maximum speed of 2.0 m/s along a caterpillar-type

belt to displace the water. The independent motion of the paddles can produce multidirectional waves with active absorption in addition to unidirectional linear and nonlinear waves. Depending on the water depth, the system can create regular waves between 0.5 sec and 10 sec period.

Additional experiments were carried out at the Large Wave Flume (LWF) to provide data for similar flow conditions at a larger scale. The LWF has a length of 104 m, a width of 3.66 m, and a height of 4.57 m. The piston-type wavemaker was installed in early 2009 prior to the second series of experiments. A hydraulic actuator moves a single piston, which in turn drives a 4.57-m high waveboard at a maximum speed of 4.0 m/s. The wavemaker capabilities are similar to the one in the TWB except for the multi-directionality of wave formation. The system can create regular waves between 0.5 sec and 10 sec period. This facility can accommodate tests with a scale of up to 2.5 times of that in the TWB.

Solitary wavelength and amplitude have an inverse relation in constant water depth. The generation of solitary waves is thus limited by the stroke of the piston. Figure 6.1 illustrates the stroke over time for three target wave conditions in the TWB and LWF. The wavemaker in the TWB can produce a maximum stroke of 2.1 m. This generates a solitary wave height of 0.8 m in 1.0 m water depth but fails to produce the same wave height in 1.2 m water depth. For a larger water depth of 1.3 m, the maximum wave height is 0.6 m. The LWF has a maximum stroke of 4.0 m. A 1.2 m solitary wave in 2.6 m water depth is already the limit of the wavemaker. The other two configurations with the solitary wave height of 1.6 m and water depths 2.0 and 2.4 m would exceed the stroke limit. It can be inferred that the maximum stroke velocities of 2 m/s and 4 m/s in the TWB and LWF are not a limiting factor for solitary wave generation in this facility.

6.3 Design of Experiment

The OSU facility offers a good opportunity to investigate the detailed hydraulic and wave processes over fringing reefs. These are often dominated by turbulence, air entrainment, and splashing that cannot be examined in small-scale experiments. The OSU TWB and LWF have sufficient scales to accommodate reef profiles commonly seen in tropical and subtropical environment. A typical reef includes an extended shallow lagoon followed by a steep fore-reef. Figure 6.2 shows reef profiles from various locations in the Hawaiian Islands, American Samoa, and Guam. The lagoon extends as far as 1 km offshore and the slope of the fore-reef has a range of 1:5 to 1:30. A pronounced reef crest that exposes at low tides might be present at the transition between the fore-reef and the lagoon. Though wave transformation over fringing reefs is a three-dimensional process, the laboratory study focuses on the characteristics of cross-shore wave transformation to understand the dominant processes. The resulting data provide an excellent opportunity for modelers to validate their numerical codes along transects in the x or y direction without the interference from the longshore components.

Two channels were constructed in the TWB with reinforced concrete walls as illustrated in Figure 6.3. Each channel is 2.16 m wide, 2.1 m high, and 38 m long with both ends open. Figure 6.4 shows the setup of the two-dimensional reef models with a 1:5 slope and $x = 0$ at the neutral position of the wavemaker. The experiments also included two other fore-reef slopes of 1:10 and 1:15 with the reef flat at 1.0 m above the bottom. The fore reef and flat were constructed of 0.1 m thick concrete poured on top of a sand fill. Some of the tests included a reef crest composed of marine plywood, which was bolted to the edge of the slope covering the entire width of the flume. The reef crests are 0.5 m long and 0.05, 0.10 and 0.15 m high extending from the fore reef. While the offshore side of the crest follows the same slope as the fore reef, the onshore side always has a 1:15 slope.

The tests were conducted with the reef crest submerged, exposed or flush with the water level.

Figure 6.5 shows the model setup in the LWF. The reef configuration is similar to the experiments in the TWB to examine the scale effects. Due to the much larger dimensions, reinforced concrete slabs were used to build the fore-reef slope and the reef flat. The prefabricated slabs of 0.2 m thickness, 3.66 m width, and 4.57 m length were mounted at bolt holes in the tank walls 0.305 m apart resulting in a 1:12 fore-reef slope and a flat reef 2.36 m above the bottom. It was necessary to cast a wedge in front of the fore reef to provide a smooth transition between the 0.2-m slab and the floor of the flume. The optional reef crest was constructed of marine plywood and set up in the same way as the experiments in the TWB. It has a crest height of 0.2 m and a length of 1.25 m with a 1:15 slope connecting the crest with the lagoon.

Figures 6.4 and 6.5 show the instrumentation layouts in the TWB and LWF experiments. The devices were mounted along the slope, reef crest, and over the lagoon to obtain the overall flow conditions involving wave shoaling, breaking, bore formation, and release of dispersive waves around the reef crest. The measurements include time series of free surface elevation and fluid particle velocity. The wave gauges, which are placed closely on either side of the reef edge, capture the free surface elevation. The flow regime required two types of wave gauge devices. Resistance-type wire gauges give accurate readings of the water level of non-breaking waves, whereas ultrasonic wave gauges can track sheet flows over dry bed as well as turbulent bores with significant amounts of white water and air bubbles. Some of the instruments are co-located to provide redundant measurements for quality control. Acoustic Doppler velocimeters (ADV) measured flow velocity at some of the wave gauge locations.

6.4 Calibration and Postprocessing

A data acquisition system (DAQ) archived signals from the resistance-type wire gauges, ultrasonic wave gauges, and acoustic Doppler velocimeters synchronically at 50 Hz during the test. Figure 6.6 shows images of the three types of instruments. The DAQ processing unit from National Instruments is a PXI-8106 in a PXI-1052 combo chassis with SCXI-1143 anti-aliasing filters. The wavemaker motion and data recording started independently as they were triggered manually.

The resistance-type wire gauges are composed of two parallel and vertically arranged surface-piercing wires attached to plastic sockets on either end. The sockets are mounted to horizontal struts in the flume walls. In shallow-water areas, the lower socket was directly screwed into the concrete floor or into the wooden reef crest. The gauge measures the resistance between the two wires in terms of the voltage to infer the free surface position. Calibration is necessary for post-processing of the returned signal in Volt to give the water depth. Voltage readings over a large range of water levels produce a linear relation as the calibration coefficient for each gauge. The calibration process was conducted during filling and draining of the basin. The chlorine content and herein the conductivity of the city water varies depending on the local weather conditions. The calibration during draining represents the instrument behavior during the tests more closely, since the water releases most of its chlorine content in the first day after filling. The minimum distance between individual resistance-type wire wave gauges is 0.7 m to avoid cross-talking between the instruments. The gauges were mounted no closer than 1.0 m apart from each other. The resistance-type wire gauges should be deployed in locations where the water column is of homogeneous nature with only a low amount of air bubbles in the fluid, since a discontinuous medium could interrupt the circuit and lead to false

readings. Due to limited supply of instruments, some resistance-type wire gauges were used in the shallow lagoon measuring signals of turbulent breaking waves.

Ultrasonic wave gauges provide non-intrusive measurements of the surface elevation. They were mounted to struts in the flume walls with the pinger near the top of the tank wall. The instrument emits a high-frequency sound signal toward the water surface and measures the time of the reflected signal to determine the water surface elevation. The ultrasonic wave gauges were calibrated prior to deployment. The calibration consists of deriving a linear relation between the measured voltage and the water surface elevation. The raw signal from each ultrasonic wave gauge was later converted to water depth by applying the calibration coefficients. Figure 6.7 shows a comparison between measurements from a resistance-type wire wave gauge and a co-located ultrasonic wave gauge at x = 17.64 m near the wavemaker and at x = 72.6 m over the reef flat in the LWF. The incident solitary wave profiles recorded at x = 17.64 m by both gauges show very good agreement. A bore developed over the reef flat with significant turbulence and air entrainment. The ultrasonic wave gauge better captures the water surface and measures the bore at slightly higher elevation than the resistance-type wire wave gauge x = 72.6 m. The discrepancy from both instruments is less than 5% of the full signal in the turbulent wave breaking regime and less than 1% for nonbreaking waves.

Nortek Vectrino 3D acoustic Doppler velocimeters (ADV) provide measurements of the fluid particle velocity at a fixed point in the flow. The device is composed of a power supply, a temperature sensor, and a probe unit mounted to a stainless steel rod. The probe unit consists of a transmitter at the center and four outward pointing transducers measuring the backscattered signal. The ADVs were mounted to struts in the flume wall and to an aluminum wing suspended from a bridge at the center of the flume. The wing could hold up to four vertically stacked ADVs. The submerged transmitter emits a sound

pulse toward a sampling volume 5 cm away and the transducers pick up the Doppler shift introduced by reflection from moving particles suspended in the water. Depending on the motion of the particles and the temperature of the water, the ADV returns three orthogonal velocity components (u,v,w) in [m/s]. Particles outside the sampling volume may cause additional backscatter and introduce noise to the signal. The ADV also records the amount of backscatter from outside the sampling volume to provide a signal to noise ratio and a scatter correlation coefficient. The backscatter quality was improved by introducing microscopic glass spheres in the water. Additional post-processing was necessary to remove spikes and outliers from the signal. The de-spiking procedure incorporated an algorithm developed by Mori *et al*. (2007) that removes signals outside a three-dimensional ellipsoid in the sampling volume. The post-processing discards all information with a signal-to-noise ratio of less than 3 and a signal correlation of less than 70%.

CHAPTER 7
WAVE PROCESSES OVER FRINGING REEFS

The two series of laboratory experiments at Oregon State University conducted in 2007 and 2009 include 198 tests with 10 two-dimensional reef configurations and ranges of solitary wave height and water depth. This dissertation presents the results from three tests with A/h = 0.5 to examine the computed hydraulic processes near the applicable limit of the model in terms of nonlinearity and dispersion. The 2009 Benchmark Challenge also at Oregon State University provides two additional test cases for wave transformation over three-dimensional reef configurations. These test cases are logical extensions of the present experiments for validation of the proposed model in a complex dynamic system.

7.1 Two-dimensional Reefs

The 198 test cases provide a database of hydraulic processes over typical reef geometries in tropical and subtropical environments. The data allows parameterization of the processes to understand the effect of reefs on surf-zone dynamics and to provide guidelines for flood hazard assessment and coastal infrastructure design. Most important to the numerical modeling community is a series of benchmarks for validation of coastal wave models. This study utilizes four of the most challenging test cases that exemplify the physical processes for validation of the model capabilities in handling nonlinearity, dispersion, wave breaking, bore propagation, and sheet flow. The effective lengths of the flumes are 45 and 84 m and the numerical model uses a grid size Δx = 0.05 m with a maximum Courant number C_r = 0.4. A Manning coefficient of $n = 0.014$ s/m$^{1/3}$ from Chaudhry (1993) describes the smooth, finished concrete surface of the reef.

The first two test cases examine wave transformation from the fore-reef onto the dry and wet reef flat without the reef crest. Figures 7.1 and 7.2 show comparisons of the computed and recorded free surface profiles and time series along the 45-m flume with a steep fore-reef of 1:5. The test involves a water depth h = 1.0 m and a 0.5 m solitary wave resulting in A/h = 0.5 and a dry reef flat. The wave steepens rapidly at the reef edge, but does not form a plunging breaker over the steep 1:5 slope. As the wave surges over the reef edge at x = 22 m, it undergoes a gradual transition from sub- to supercritical flow. The numerical model reproduces the collapse of the wave front at x = 23 m and the surge onto the dry bed around $t\sqrt{g/h} = 55$ with a rarefaction wave. The water rushes over the dry reef flat as sheet flow without producing a pronounced bore-shape leading edge as observed in the experiments. The model captures the timing and depth. Meanwhile, the reflected component of the rarefaction falls below the initial water level exposing the reef edge momentarily, separating the flow into two segments. This demonstrates the models capability in capturing the moving wave front and wet-dry interfaces. Researchers typically use measurements of free surface elevation for model validation, while the capability of the depth-integrated models in describing flow speed is not known with certainty. Figure 7.3 shows the computed and measured flow speed of the solitary wave over the fore reef as well as the formation of the surge on the reef flat. The results are non-dimensionalized with the shallow-water celerity from the still water depth at the gauge locations; whereas the maximum bore height is used on the dry reef flat. The comparisons show very good agreement of the solitary wave and the subsequent sheet flow even at high Froude number. The minor discrepancy in the remainder of the flow is most likely due to the openings at the two ends of the laboratory flume that do not reflect the waves in the same way as in the numerical model.

The slope of the fore reef plays an important role in the wave breaking processes. Figure 7.4 shows the free surface profiles along the 84-m wave flume with a gentle fore-reef of 1:12. The test involves and a water depth of h = 2.46 m and a 1.23 m solitary wave resulting in A/h = 0.5 and standing water of 0.1 m over the reef flat. The initially symmetric solitary wave begins to skew to the front as it propagates across the toe of the slope at x = 25.9 m. In the laboratory experiments, a plunging wave breaker developed around $t\sqrt{g/h} = 64$. The jet from the breaking wave hits the water surface and forms an elliptical air cavity around $t\sqrt{g/h} = 66$ that shortly collapses and produces extensive air entrainment in the flow. The depth-integrated model does not describe overturning of the free surface, but instead approximates the entire process through conservation of volume and momentum. The solution mimics the plunging breaker as a collapsing bore, which slightly underestimates the height of the jet, but conserves the volume immediately behind the bore. The bore continues to propagate over the reef flat because of the standing water. The reflected bore from the back wall disintegrates into a series of dispersive waves over the fore reef. Figure 7.5 shows the model captures the incident wave and bore as well as the multiple reflections in the closed flume. High frequency dispersive waves superposed on long period reflection are evident after signals of the initial waves. This demonstrates the capability of the model in describing flux- and dispersion-dominated processes simultaneously. The comparison in Figure 7.6 shows the model correctly describes the flow velocity resulting from the two systems of waves even across discontinuities.

Most fringing reefs have an exposed reef crest and a lagoon that modify the hydraulic processes on the reef flat. Figure 7.7 shows the computed and measured free surface profiles along the 84-m flume. The test includes a fore reef slope of 1/12, a 0.2-m reef crest, and a water depth of 2.5 m. This setup exposes the reef crest by 6 cm and

submerges the flat with 14 cm of water. The 0.75-m solitary wave gives a dimensionless wave height of A/h = 0.5. The solitary wave shoals over the relatively gentle slope. The profile becomes near vertical and the wave begins to break around $t\sqrt{g/h} = 57$. Observations during the laboratory experiment indicate subsequent overturning of the free surface and the development of a plunging breaker on top of the reef crest with air entrainment and splash-up around $t\sqrt{g/h} = 60$. The present model mimics the plunging breaker as a collapsing bore and correctly describes the free surface profile during the entire process. The flow transitions to advection- or flux-dominated over the reef flat such that the conservative form of the governing equations becomes instrumental in capturing the pertinent hydraulic processes. Around $t\sqrt{g/h} = 61$, the broken wave begins to travel down the back slope of the reef crest and generates a supercritical flow displacing the initially still water in the lagoon. The flow generates a hydraulic jump off the back reef and a propagating bore downstream. Laboratory observations indicate overturning of the free surface at the hydraulic jump as the supercritical flow transfers volume and momentum to the subcritical flow that fuel the propagating bore at the front. The hydraulic jump initially moves downstream with the strong supercritical flow. Around $t\sqrt{g/h} = 68$, the momentum flux balances at the flow discontinuity and the hydraulic jump becomes stationary momentarily. The present model detects the breaking at the hydraulic jump during the process through the momentum gradient in the Riemann solver approach that would otherwise not be accounted for by conventional methods based on free surface motion. The hydraulic jump subsequently diminishes with the flow and moves back to the reef crest as a bore. In the meanwhile, the propagating bore shows a gradual reduction in amplitude and continues to propagate downstream.

The end wall of the flume reflects the bore back to the lagoon that in turn overtops the reef crest as sheet flow and generates a hydraulic jump on the fore reef. The reflected

bore, which has lower Froude number, generates a series of dispersive waves that warrant a closer examination. Figure 7.8 compares the computed and recorded surface elevation time series. The station at x = 80 m immediate adjacent to the incident bore and its reflection superposed on top of it, while the gauge at x = 72.7 recorded separate incident and reflected bores. The time series at x = 65.2 on the reef flat shows the reflected bore from the end wall as well as its reflection from the reef crest. The process continues with the subsequent reflection from the end wall. The time series at x = 57.9m shows overtopping at the reef crest. As the water rushes down the fore reef, the flow transitions back from flux to dispersion-dominated through a hydraulic jump. Observations during the experiments confirm an overturning free surface with air entrainment near x = 54.4 m. The hydraulic jump initially generates an offshore propagating bore, which transforms into a train of waves over the increasing water depth over the fore reef at $x \leq 50.4$ m. The resulting undulations intensify as higher harmonics are released from the wave packet. At the same time a long period reflected wave propagates in onshore direction and superposes with the released higher harmonics from the offshore propagating bore. Wave gauges located near the toe of the slope record highly dispersive waves of $kh > 15$ that cannot be fully resolved by the present model. The subsequent oscillations show a slight over-prediction in wave height. Figure 7.9 shows the velocity in x direction at a location in front of the reef crest. Despite its depth-integrated structure, the model captures the velocity of the initial strong supercritical flow conditions and subsequent dispersive waves.

The model reproduces the long and intermediate-period oscillations even after a long simulation involving a series of wave breaking and reflection in the flume throughout the two tests in the LWF. The conservative structure of the model allows description of the transition between super and subcritical flows and the present wave breaking model

reproduces the surging and plunging waves over the reef. This test also demonstrates the applicability of the Riemann solver model for wave breaking. The local deactivation of dispersion terms efficiently eliminates potential instabilities, and at the same time, does not alter the dispersion properties of subsequent wave transformation processes such as the release of higher order dispersive waves from a decaying bore.

7.2 Three-dimensional Reefs

The National Science Foundation funded a workshop and a benchmarking exercise for inundation models at the Oregon State University in 2009. The organizer provided two benchmark test cases with laboratory data from experiments at the Tsunami Wave Basin. Swigler (2009) provided a detailed description of the experiments, instrumentation, and data post-processing. These test cases, which involve wave transformation over three-dimensional reef configurations, are logical extensions of the present experiments. The laboratory data allows validation of models to handle dispersion and flux dominated processes simultaneously.

Figure 7.10 shows the finished reef configuration determined from a laser scan and the setup of the instrumentation for Benchmark I. The neutral position of the wavemaker is at $x = 0$. The main feature in the experiment is a triangular reef flat between 7.5 and 9 cm below the still water level. The reef sits on top of a bilinear background profile extending from $x = 10.2$ to 17.7 m at a slope of 1:16 and from $x = 17.7$ to 32.4 m at 1:32. The slope of the reef is 1:3.5 at the apex and flares to 1:16 over a distance of 9 m on either side to converge the wave energy. The water depth in front of the bilinear profile varies slightly around 0.78 m. The top of the relief model has an elevation between 0.16 to 0.13 m above the still water level with a mild grade to the back of the basin. Time series of the water surface elevation were reported along transects at the centerline from gauges 1 to 7,

at 5 m offset from gauges 8 to 13, and at the edge of the reef flat from gauges 7 and 14 to 17. Velocity measurements are available at gauges 3, 6, and 13. Because of the limited supply of instruments, the data were recorded over several weeks from a number of repetitions of the same test conditions with the instrument array repositioned along the basin.

The incident solitary wave has a height of 0.39 m giving rise to strongly nonlinear conditions with $A/h = 0.5$. Figure 7.11 shows a series of snapshots as the solitary wave transforms over the reef and slope complex. In the laboratory experiment, spilling at the crest occurred locally at $t = 5$ sec, when the solitary wave reached the apex of the reef with little shoaling over the steep slope. With shoaling of the wave along the sides, plunging subsequently developed along the entire length of reef edge at $t = 8$ sec. The model reproduces the breaking process as a collapsing bore spreading across the triangular reef flat. The flow transitions into a surge moving up the initially dry slope and overtops the reef and slope complex. At $t = 22$ sec, drawdown of the water has already occurred on the slope interacting with the reflection from the wavemaker, while the sheet flow on the top continues to move forward. As observed in the laboratory experiment, the upper slope is mostly dry with water trickling down the streaks of the concrete surface and the sheet flow at the top has been reflected from the back wall as a bore over the impounded water by $t = 35$ sec. The panel at $t = 48$ sec shows the second reflection from the wavemaker and sloshing of the impounded water at the top separated by the dry upper slope.

The data from the laboratory experiment allows a quantitative comparison with the model prediction. Figures 7.12 and 7.13 show good agreement of the computed and recorded surface elevation during the initial steepening and breaking of the solitary wave along the two cross-shore transects of the basin. The model gives slightly higher amplitude at the

front of the subsequent bores, including those shown in the longshore transect in Figure 7.14, but reproduces the overall profile reasonably well. The timing of the first and second reflection from the wavemaker is slightly off at the gauges over the shallow reef flat. This discrepancy is probably due to inadvertent, minor changes of the water levels between the repetitions that become significant in comparison to the 8 cm water depth over the reef flat. Figure 7.15 compares the recorded and computed flow velocity components at three of the gauges in the x and y directions. At the apex of the reef, the model reproduces the entire recorded time series of the x component of the velocity. The recorded data are not continuous at the two other locations at the reef flat but generally agree with the model output albeit with minor phase shift of the reflection. The hydraulic processes over the reef flat primarily involve flows in cross-shore direction as indicated in the model data. Fluctuations in the recorded y component of the flow velocity are observed even along the centerline of the basin. The signal, which is an order of magnitude lower compared to the x component, might be due to secondary flow structures such as vortices that the model cannot fully describe.

Benchmark II utilizes the same relief model but with a concrete cone of 6 m diameter and 0.45 m height fitted to the apex of the reef between x = 14 and 20 m. Figure 7.16 shows the test configuration and instrumentation layout. The presence of the cone modifies the hydraulic processes over the reef flat and provides even more complex wave dynamics for model validation. Figure 7.17 shows snapshots of the computed free surface elevation in the basin. The solitary wave breaks at the apex of the reef flat at t = 5.1 sec and the resulting surge completely overtops the cone at t = 6.6 sec. The refracted waves from the two sides of the cone collide in the back at t = 8.6 sec and continue to wrap around as trapped waves. The diffracted wave on the leeside of the cone propagates up the slope reinforcing the refracted waves from the reef edge. The drawdown of the diffracted wave

generates a bore, which collides with the reflection from the wavemaker over the reef flat around t = 17 sec and part of which is trapped around the cone as shown in the panel at t = 21.2 sec. Figure 7.18 compares the computed and recorded surface elevations. The model reproduces the recorded surface elevations in front of the cone and gives well defined peaks behind the cone that the instruments give negative or zero surface elevation probably due to turbulence and air entrainment. The model reproduces the x component of the velocity at gauge 2 in front of the cone as shown in Figure 7.19. The recorded data at gauge 3 missed the initial wave probably due to the turbulence and air entrainment behind the cone. Gauge 7 recorded most of the initial wave and gives good agreement with the computed data. The y component of the velocity is an order of magnitude smaller with distinct secondary flow structures. The overall agreement between the computed and recorded data demonstrates the validity of the proposed model in handling multiple hydraulic processes and a variety of wave breakers in the two-dimensional horizontal plane.

CHAPTER 8
CONCLUSIONS AND RECOMMENDATIONS

This dissertation has introduced an alternate form of Boussinesq-type equations with shock-capturing capabilities and demonstrated its use along with a conservative numerical scheme for modeling of breaking waves over fringing reefs. The Boussinesq-type equations of Nwogu (1993) are expressed in conserved variables and rearranged in the conservative form of the nonlinear shallow-water equations. The formulation incorporates the dispersion terms with time and spatial derivatives in either x or y direction into a new set of evolution variables. The governing equations have the same dispersion characteristics as Nwogu's (1993) and contain identical flux terms as the nonlinear shallow-water equations for proper handling of discontinuous flows as demonstrated by the Rankine-Hugoniot jump condition. This allows the governing equation to describe wave breaking as bores without additional terms to account for super-critical flow.

A Godunov-type scheme based on a Riemann solver integrates the evolution variables in time. The dispersion terms with time and spatial derivatives in x and y directions reduce to weighted summation of the solutions at previous time steps. The evolution variables in the momentum equations provide tri-diagonal systems of equations from which the flow velocity can be determined. Since the evolution variables contain spatial derivatives in either x or y direction, the two-dimensional problem is uncoupled into a series of one-dimensional problems for the solution of the velocity in the x and y directions. Data from a previous laboratory study allows calibration of an analytical and an eddy viscosity model to describe energy dissipation associated with wave breaking. Although the eddy viscosity approach performs better than the analytical approach in the calibration, the latter is preferred for general application as it determines the breaking threshold using

only one coefficient without the need for a tracking mechanism and contains all admissible wave breaking conditions and their combinations to construct a wave-breaking scenario.

The conservative formulation and numerical scheme enhance the capability and applicability of Boussinesq-type models without altering their dispersion characteristics. The model correctly describes generation of higher-order harmonics over a submerged bar and produces good agreement with laboratory data for the water depth parameter up to $kh = 5$. The shock-capturing Godunov-type scheme mimics energetic breaking waves as collapsing bores and models the moving waterline with a Riemann solver. The present model produces very good agreement with laboratory data in the plane-beach and conical island runup experiments. Two series of laboratory experiments at Oregon State University provide a unique dataset for understanding of the hydraulic processes and validation of coastal wave models for application in fringing reef environment. The model reproduces the height and velocity of breaking waves, propagating bores, and high-frequency dispersive waves recorded in the experiments. Comparison with the laboratory data for a variety of breaker types confirms the validity of the proposed breaking mechanism based entirely on momentum flux.

The work described in this dissertation has opened an alternate direction in ocean and coastal wave modeling with many opportunities for practical application and further research and development. A major contribution is the development of a tool for flood hazard mapping and assessment in fringing reef environment. Computational requirements are important issues in practical application. The reduction of the two-dimensional solution to a series of uncoupled one-dimensional problems is ideal for code parallelization. A spectral, multi-directional wavemaker algorithm is necessary to describe realistic incident wave conditions for subsequent modeling of surf zone

processes and inundation. The model could also be extended to shorter period waves by including higher order dispersion in the governing equations. A grid nesting or refinement scheme will be instrumental for modeling of basin-wide propagation and coastal runup of tsunamis.

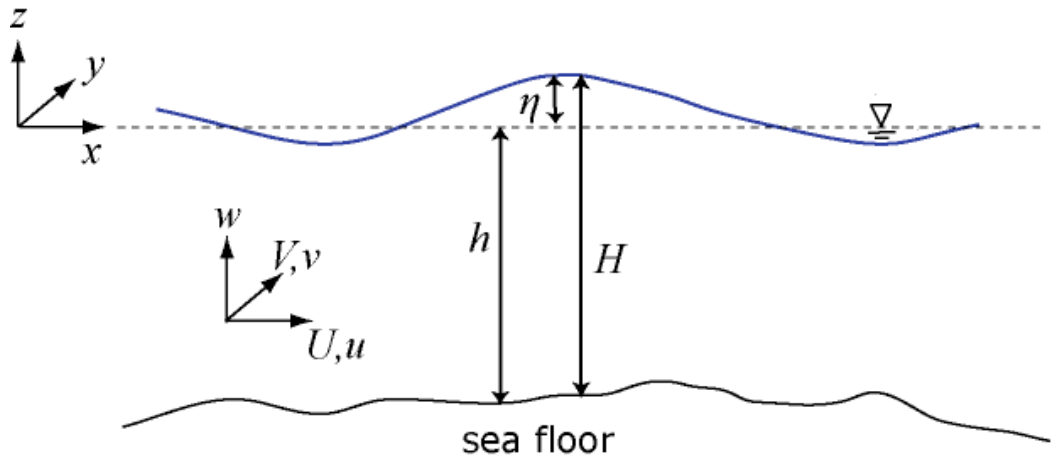

Figure 2.1 Schematic of the free-surface flow problem.

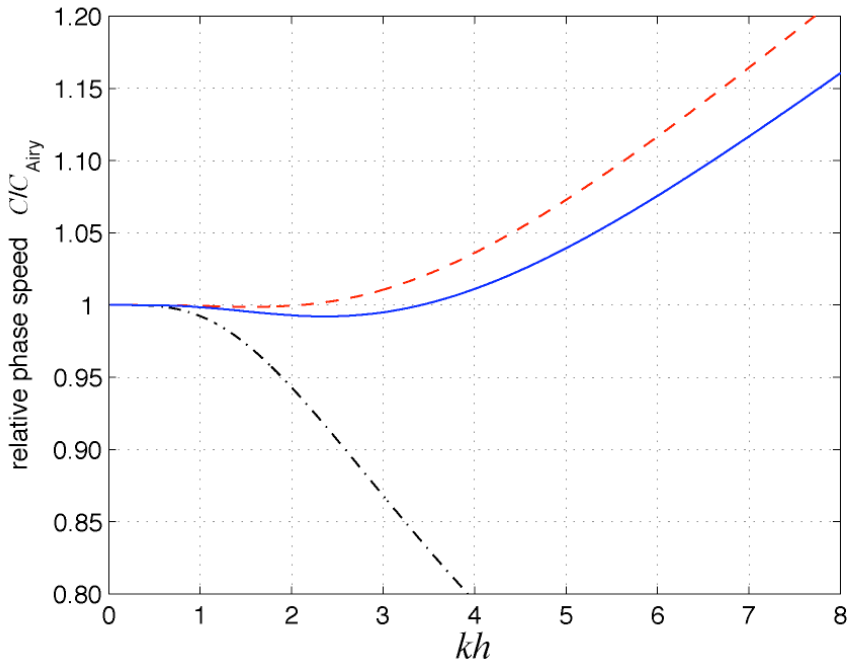

Figure 2.2 Linear dispersion properties. ——— (blue), α = -0.38519; - - - - (red), α = -0.393; – · – · – (black), α = -1/3 equivalent to Peregrine (1967).

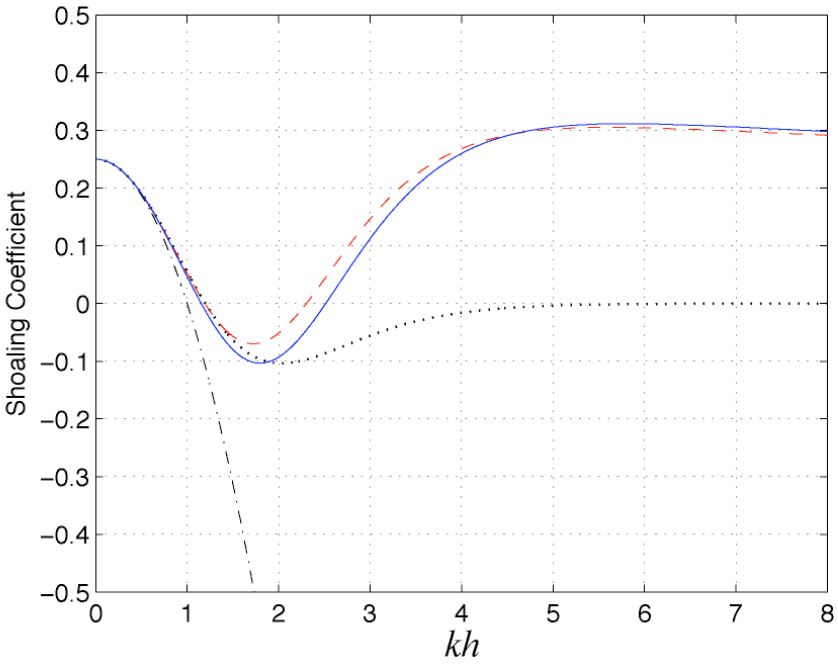

Figure 2.3 Linear shoaling properties. ——— (blue), α = -0.38519; - - - - (red), α = -0.393; – · – · – (black), α = -1/3 equivalent to Peregrine (1967).

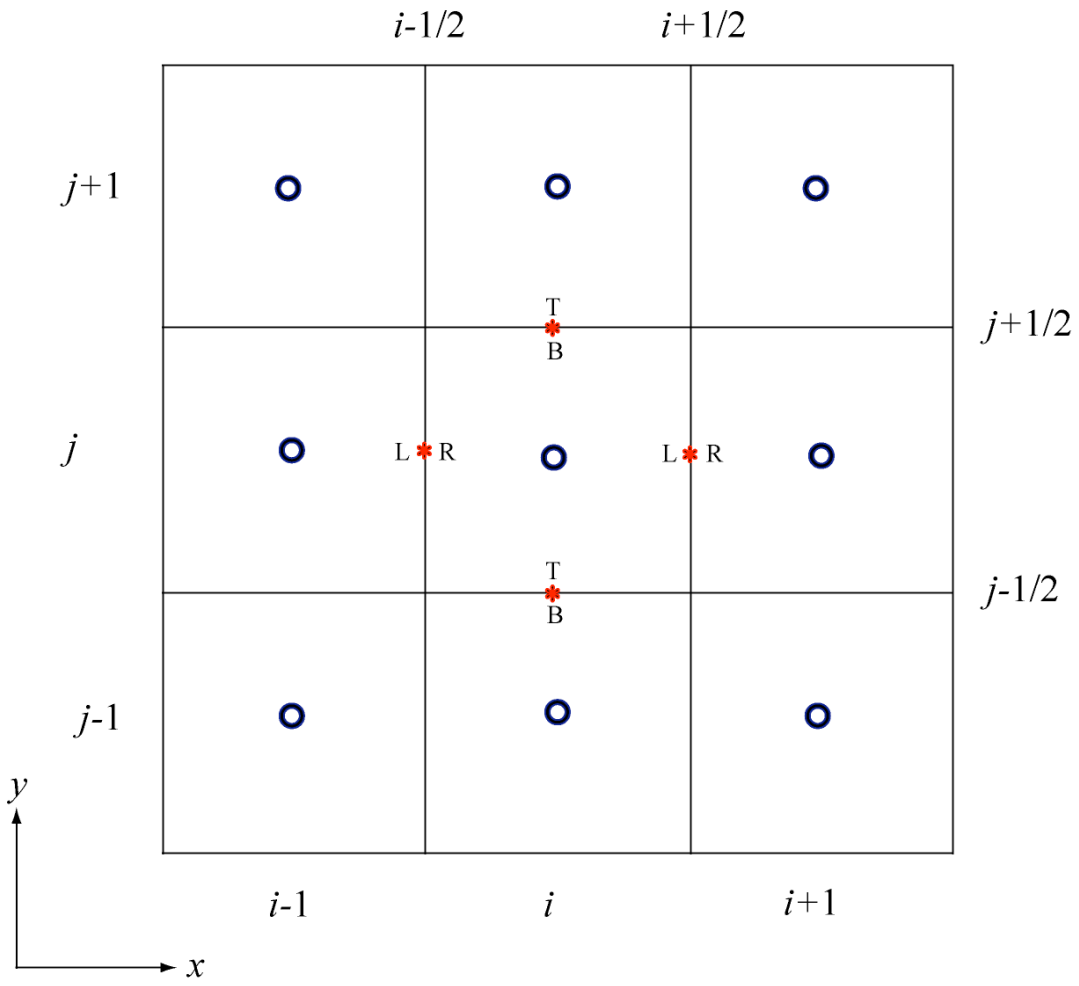

Figure 3.1 Definition sketch of spatial grid (plane view). Red stars indicate the positions of the Riemann solution.

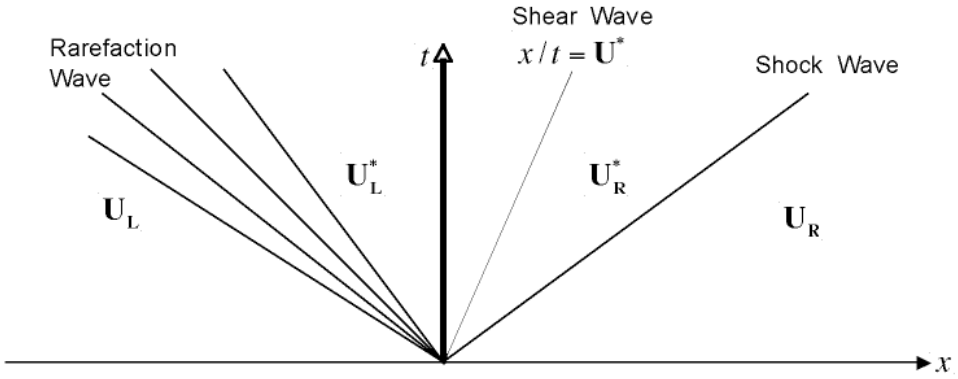

Figure 3.2 Definition sketch of the Riemann problem.

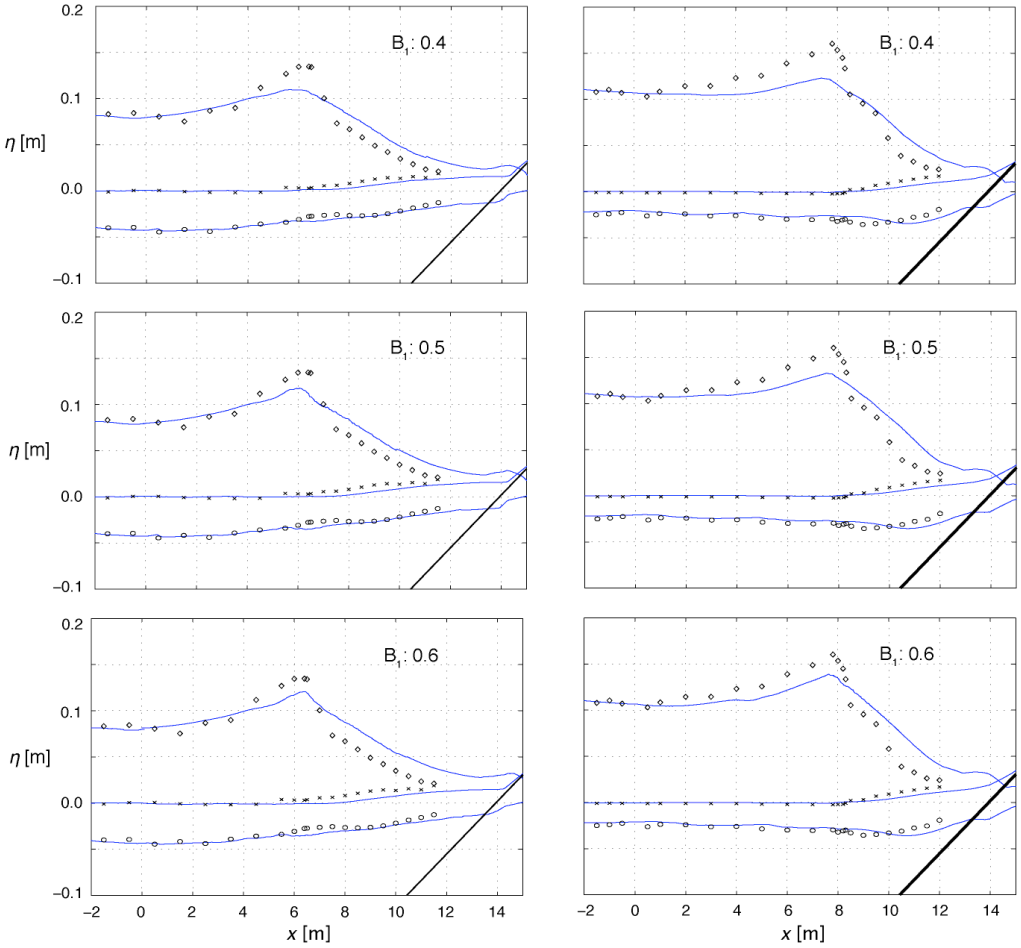

Figure 4.1 Comparison of laboratory data from Ting & Kirby (1994) and model results using the Riemann solver approach for different calibration parameters for spilling (left) and plunging (right) wave breakers. Diamonds denote crest envelope, circles denote trough envelope, and crosses denote wave setup. Solid lines indicate model results.

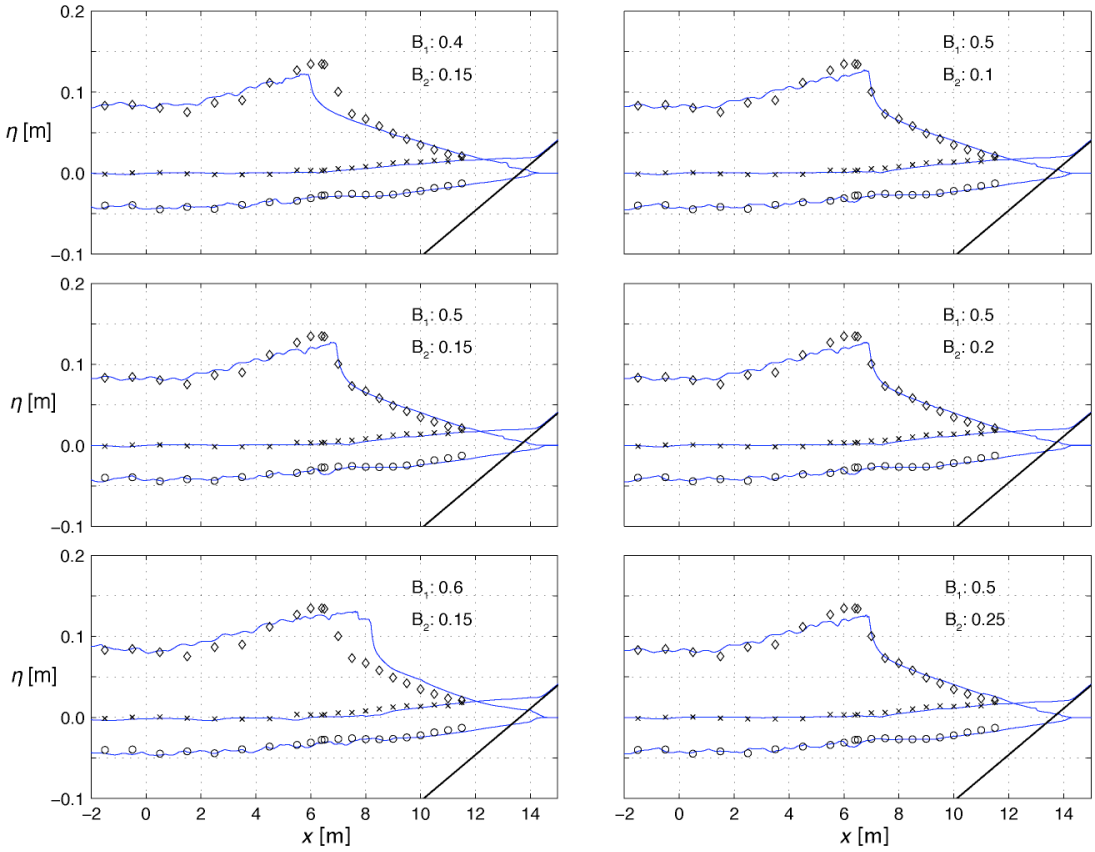

Figure 4.2 Comparison of laboratory data from Ting & Kirby (1994) and model results using the eddy viscosity approach for spilling wave breakers. Diamonds denote crest envelope, circles denote trough envelope, and crosses denote wave setup. Solid lines indicate model results.

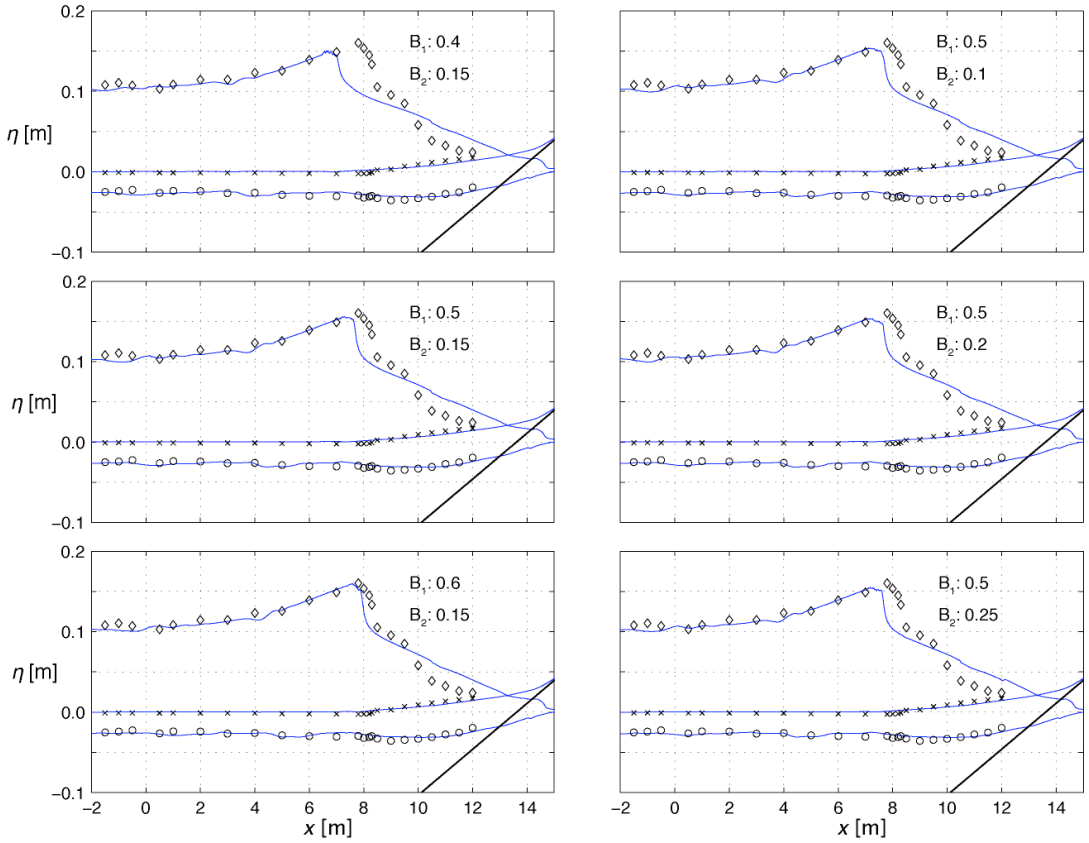

Figure 4.3 Comparison of laboratory data from Ting & Kirby (1994) and model results using the Riemann solver approach for plunging wave breakers. Diamonds denote crest envelope, circles denote trough envelope, and crosses denote wave setup. Solid lines indicate model results.

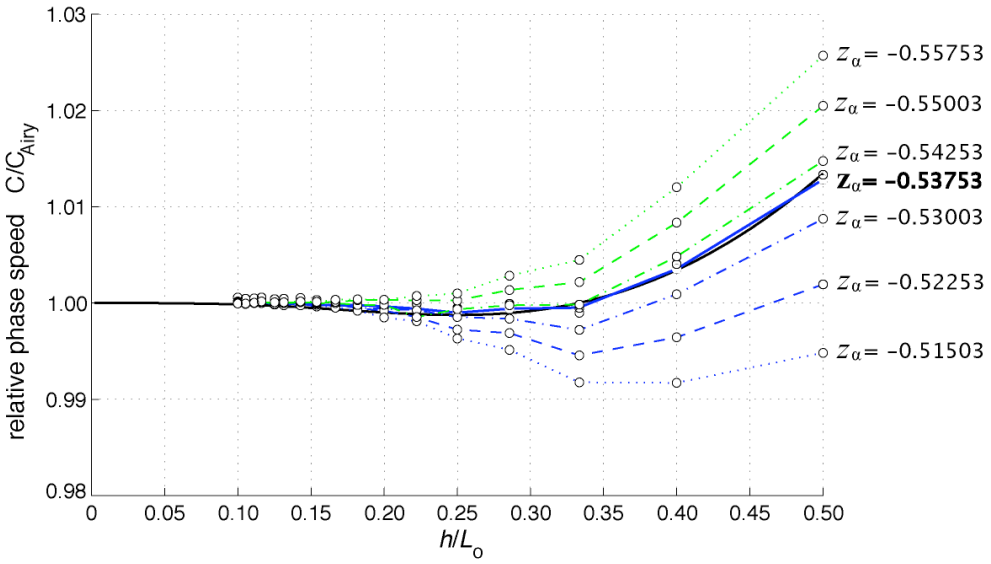

Figure 5.1. Computed celerity for different reference depths. Black line denotes celerity obtained from the linearized form of the Boussinesq-type equations at z_α = -0.53753.

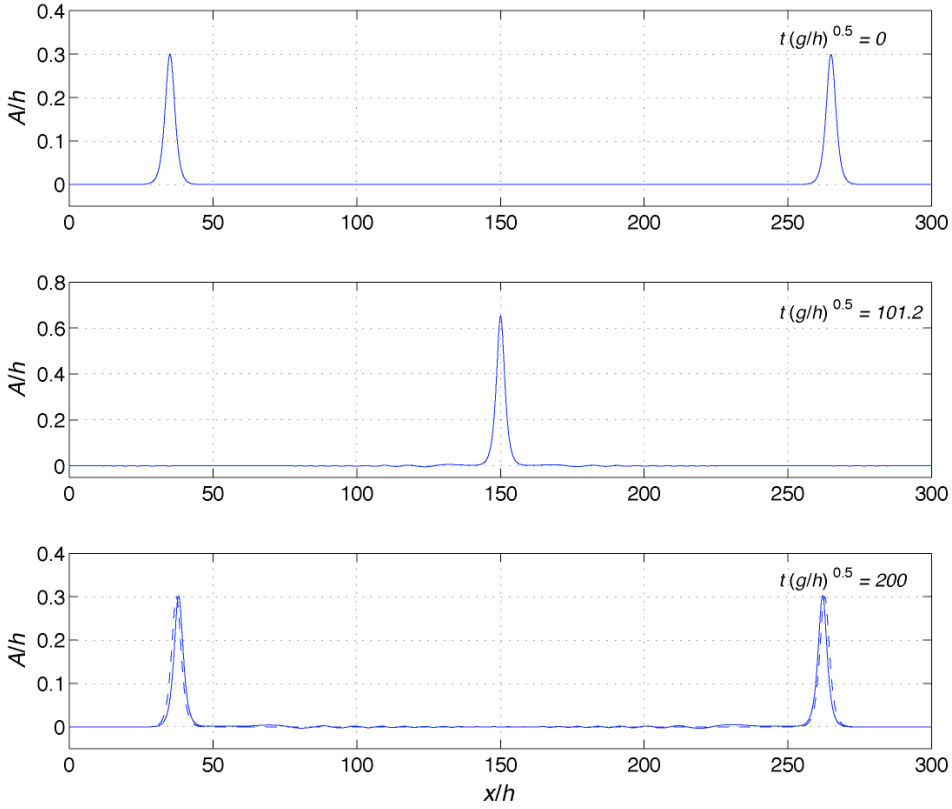

Figure 5.2. Surface profiles of solitary waves with A/h = 0.3 propagating in opposite directions in a channel of constant depth. Solid and dash lines denote numerical and analytical solutions.

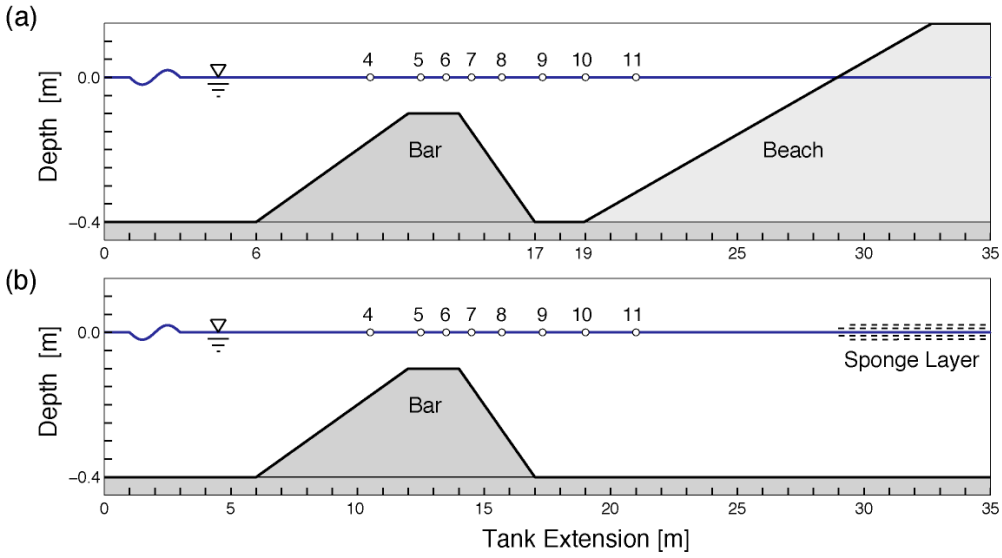

Figure 5.3. Definition sketch of wave transformation over a submerged bar. (a) Laboratory setup from Beji and Battjes (1993). (b) Numerical model setup. Circles denote gauge locations.

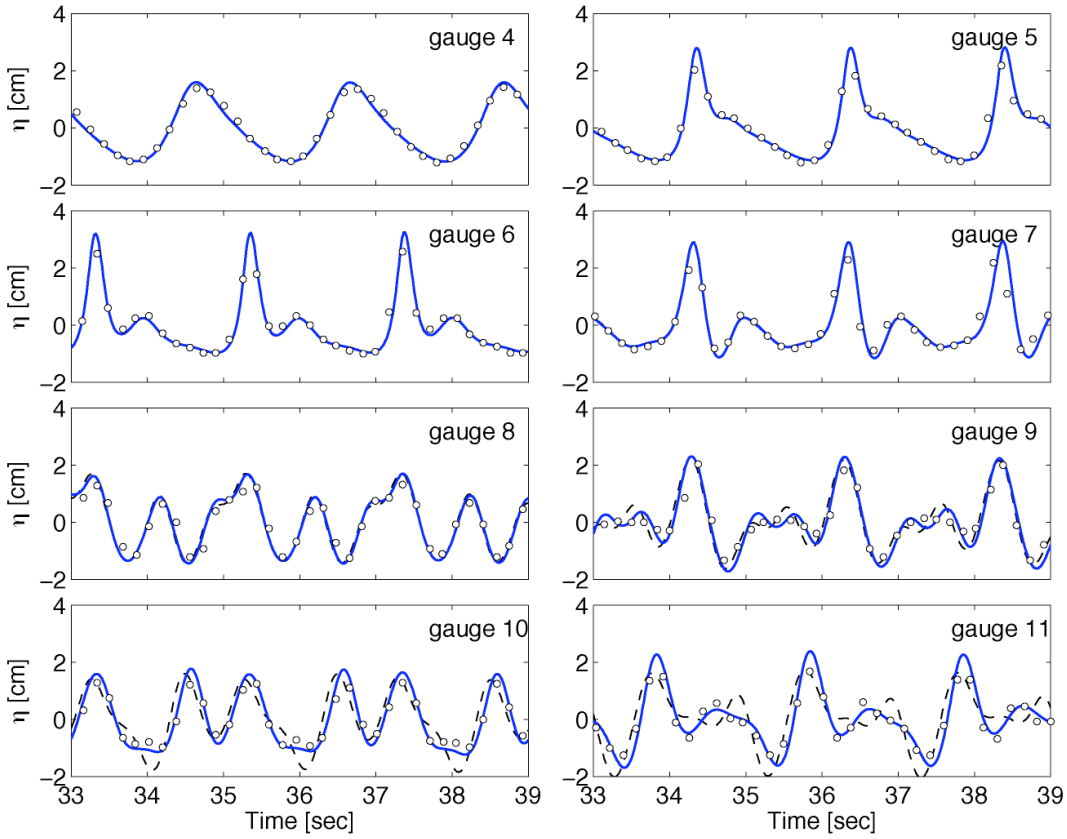

Figure 5.4. Surface elevations of sinusoidal wave transformation over a submerged bar with A = 1.0 cm and T = 2.02 s. Solid lines denote computed results, where ——— (blue), α = -0.38519; – – – · (black), α = -0.393. Circles denote measured data.

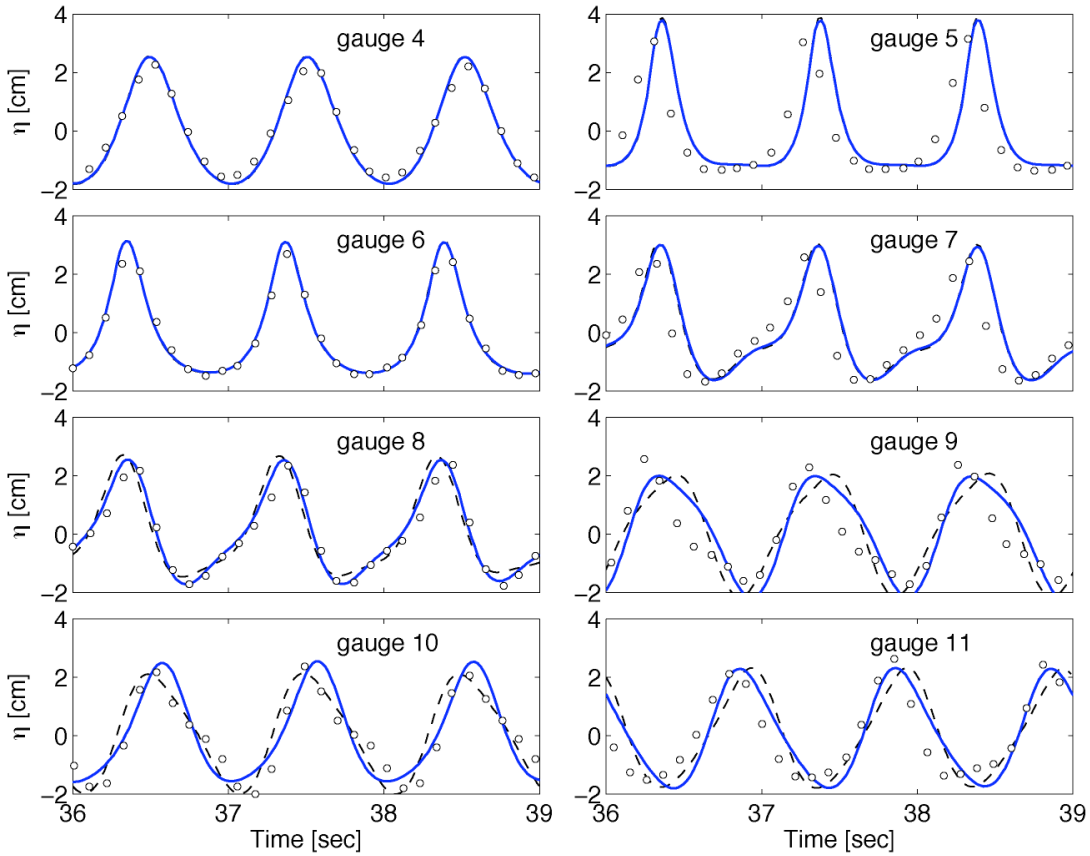

Figure 5.4. Surface elevations of sinusoidal wave transformation over a submerged bar with A = 2.05 cm and T = 1.01 s. Solid lines denote computed results, where ——— (blue), α = -0.38519; – – – · (black), α = -0.393. Circles denote measured data.

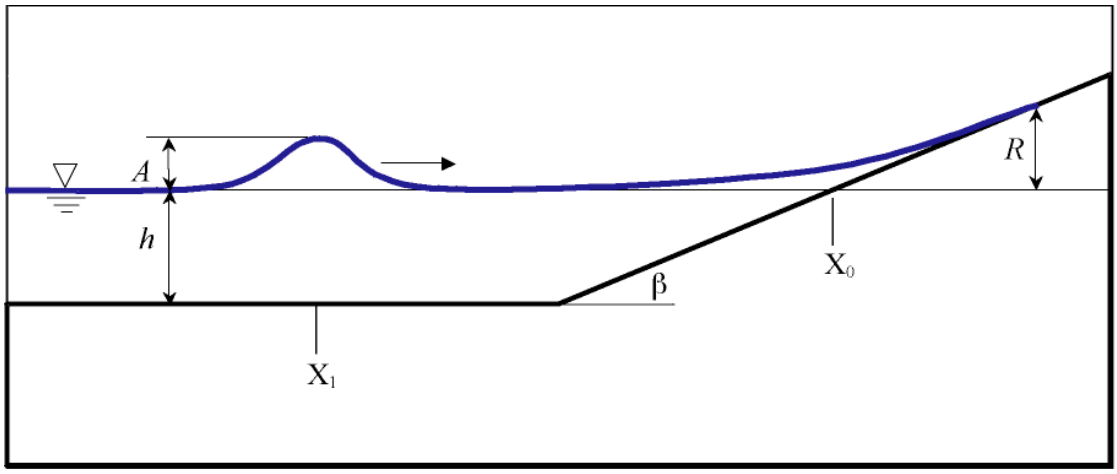

Figure 5.6. Definition sketch of solitary wave runup on a plane beach.

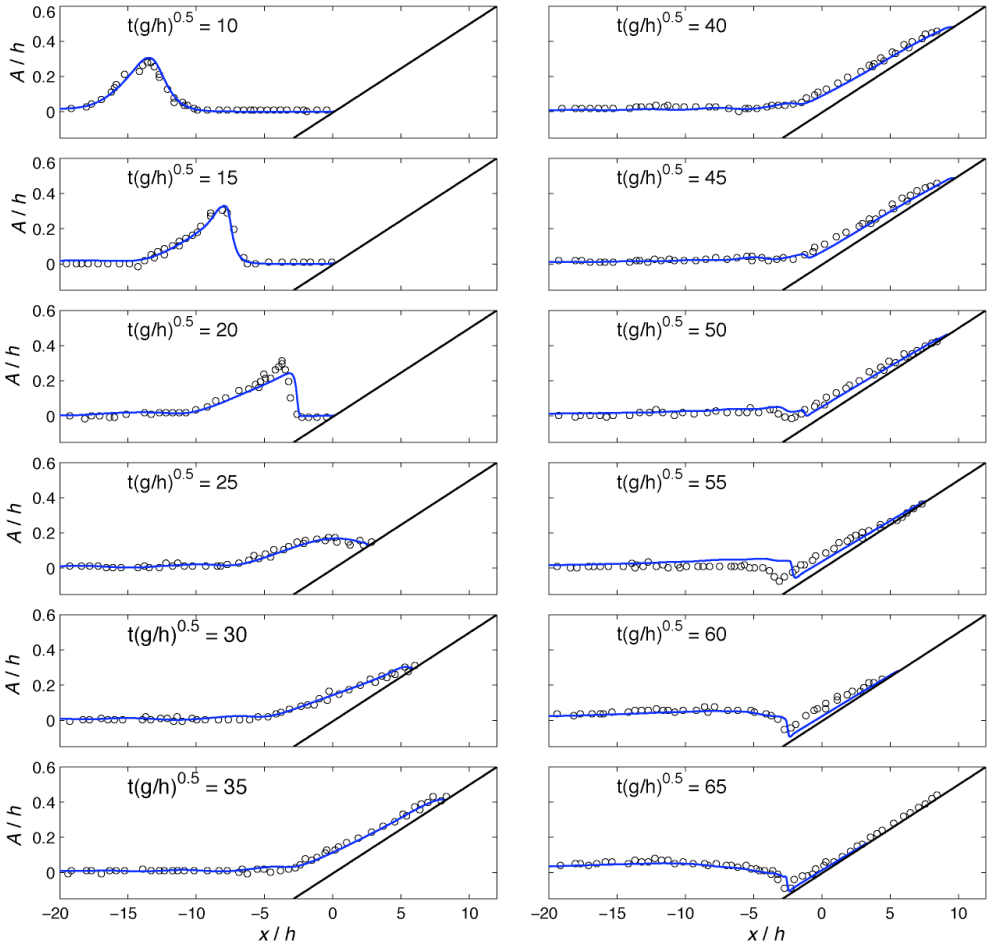

Figure 5.7. Free surface profiles of solitary wave transformation on a 1:19.85 plane beach with A/h = 0.3. Solid lines and circles denote computed and measured data.

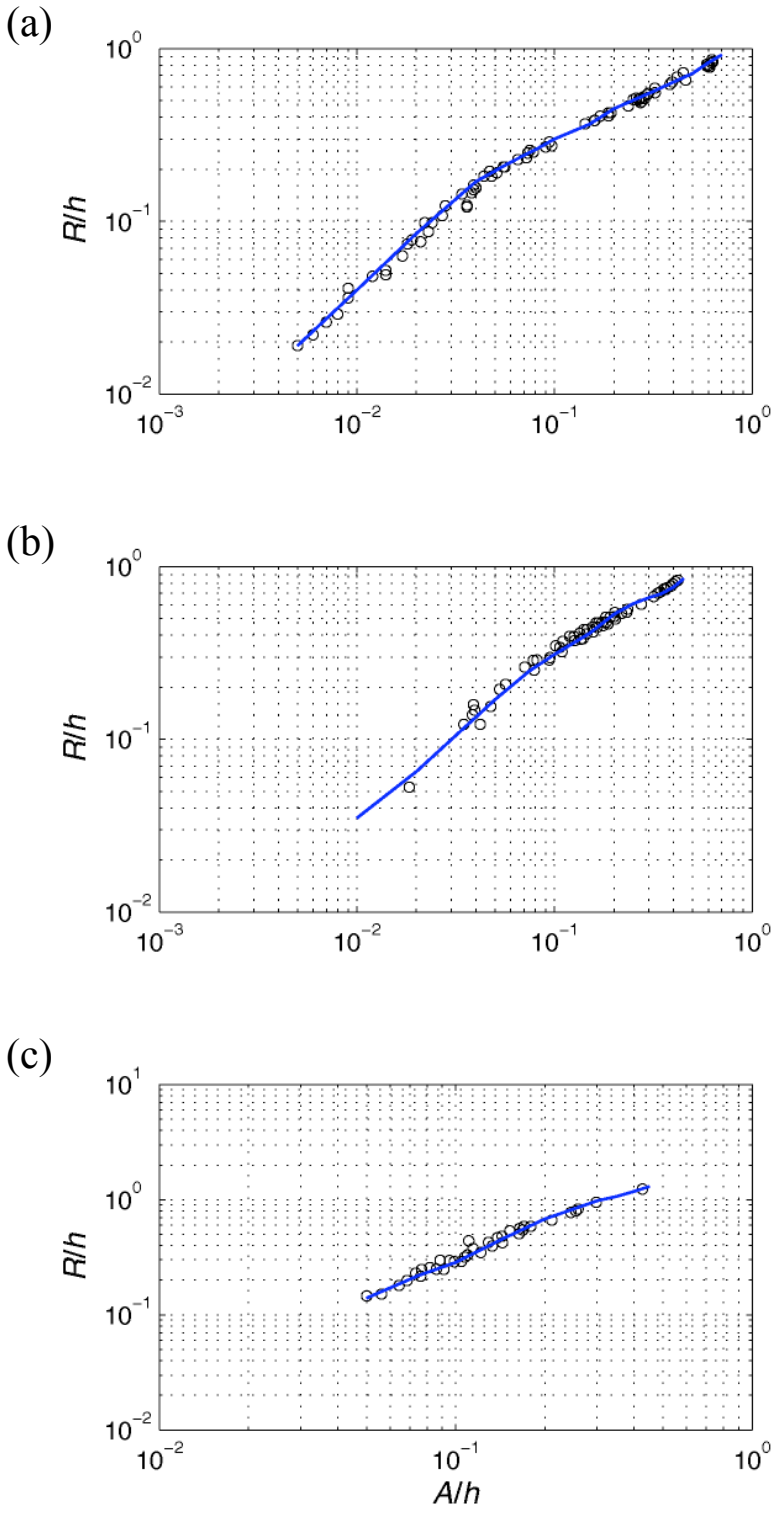

Figure 5.8. Solitary wave runup on a plane beach. (a) 1:19.85 (Synolakis, 1987). (b) 1:15 (Li & Raichlen, 2002). (c) 1:5.67 (Hall & Watts, 1953). Solid lines and circles denote computed and measured data.

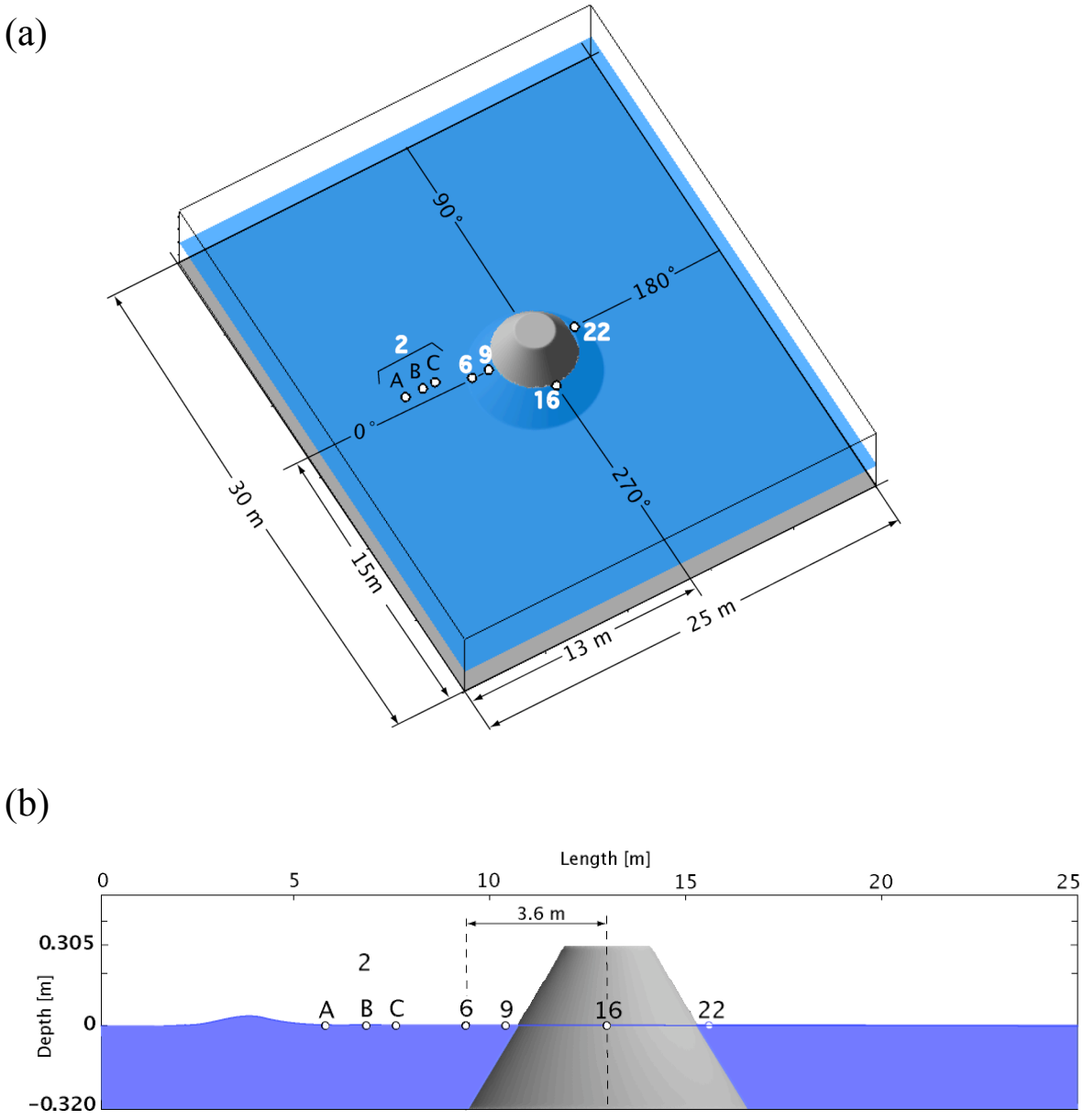

Figure 5.9. Schematics of the conical island laboratory experiment. (a) Perspective view. (b) Cross-sectional view along centerline. Circles denote gauge locations.

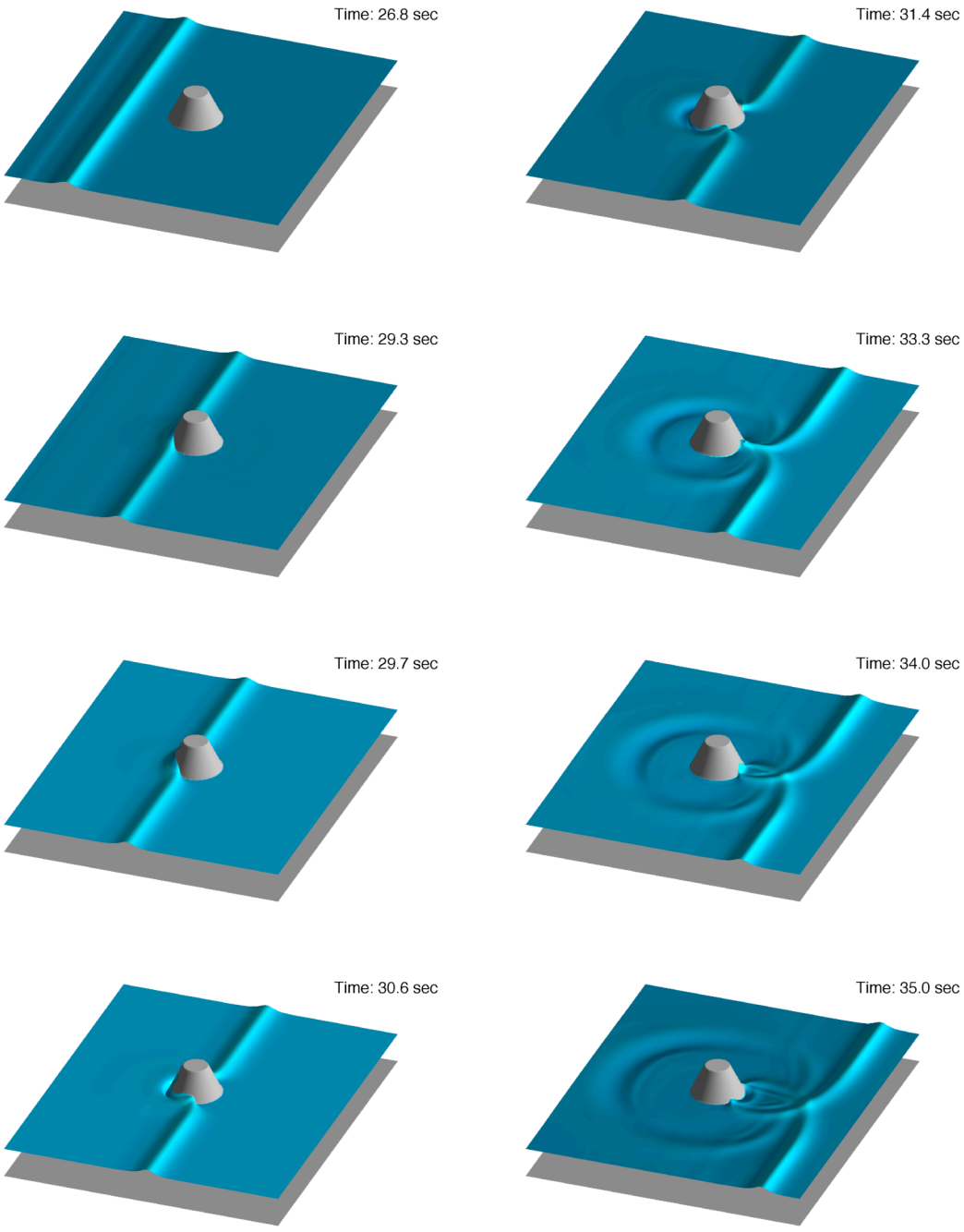

Figure 5.10. Wave transformation around the conical island for $A/h = 0.181$.

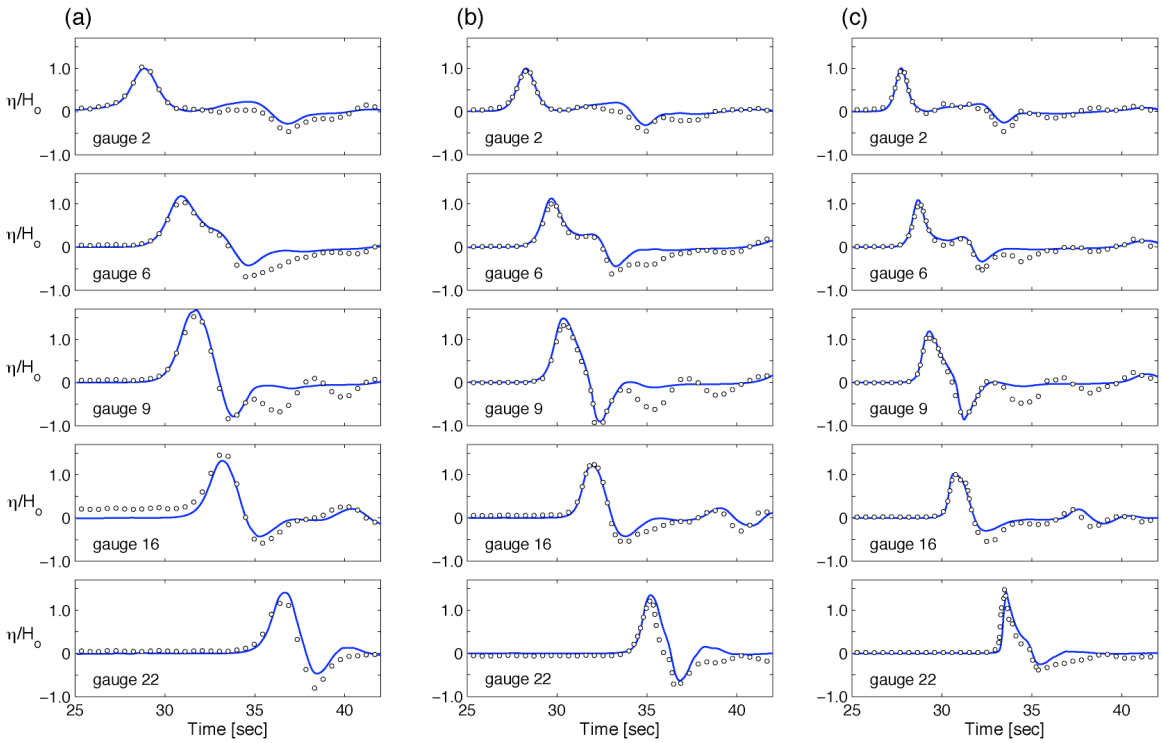

Figure 5.11. Free surface profiles of wave transformation around the conical island. (a) A/h = 0.045; (b) A/h = 0.096; (c) A/h = 0.181. Solid lines and circles denote computed and measured data.

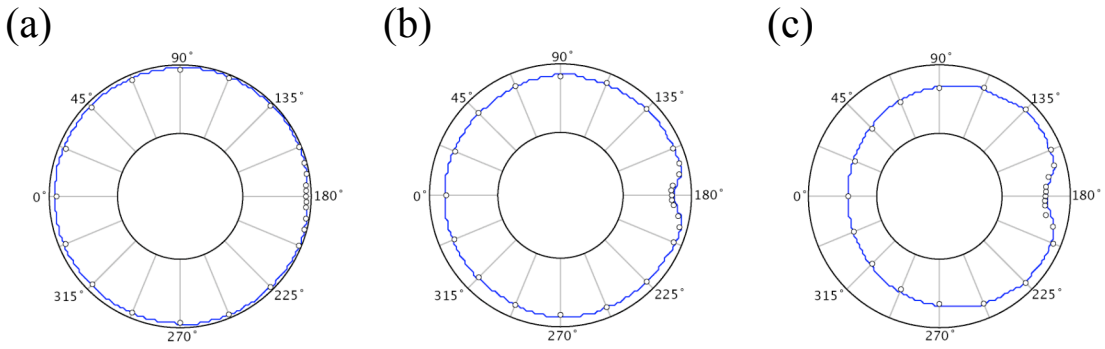

Figure 5.12. Maximum inundation around the conical island. (a) A/h = 0.045; (b) A/h = 0.096; (c) A/h = 0.181. Solid lines and circles denote computed and measured data.

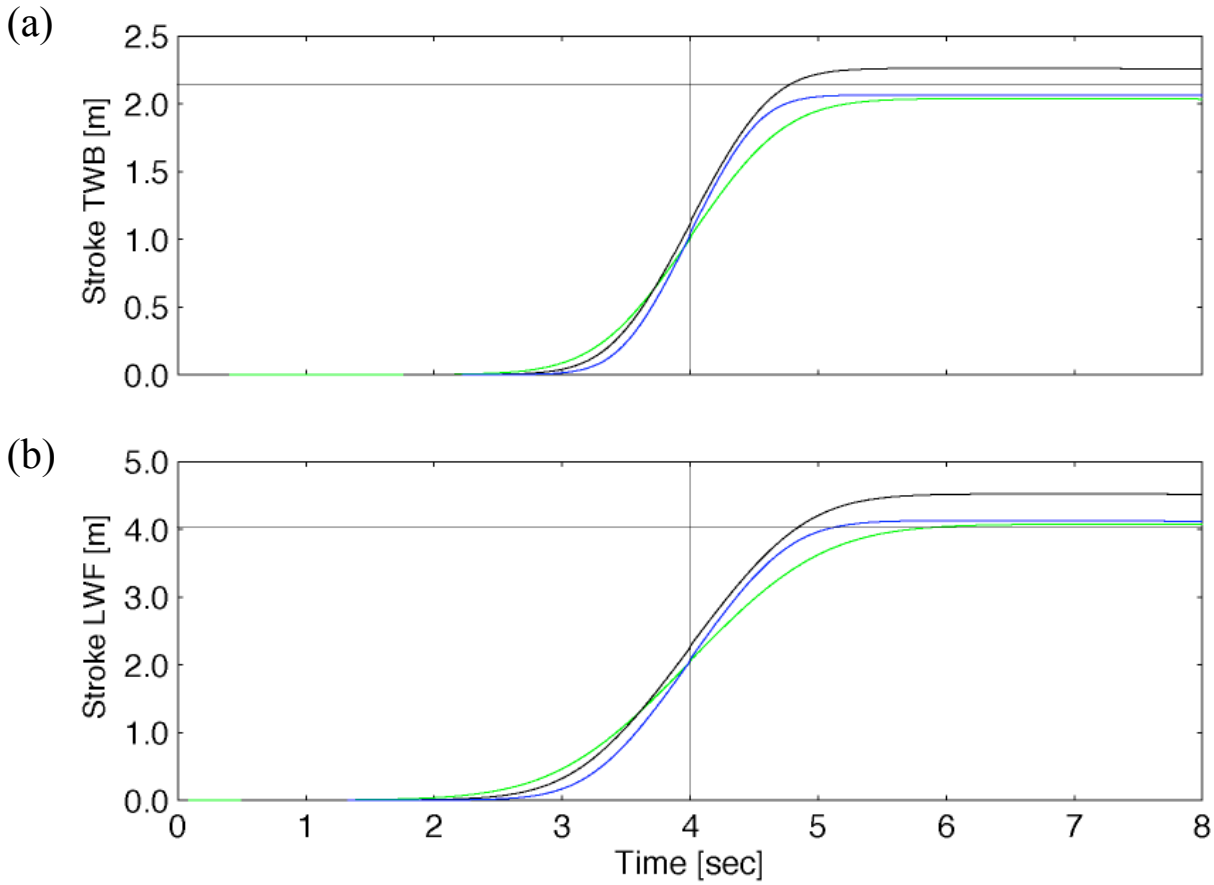

Figure 6.1 Wavemaker stroke at O.H. Hinsdale Wave Research Laboratory at Oregon State University. (a) Tsunami Wave Basin; —— (blue), A = 0.8 m, h = 1.0 m; —— (black), A = 0.8 m, h = 1.2 m; —— (green), A = 0.6 m, h = 1.3 m. (b) Large Wave Flume; —— (blue), A = 1.6 m, h = 2.0 m; —— (black), A = 1.6 m, h = 2.4 m; —— (green), A = 1.2 m, h = 2.6 m.

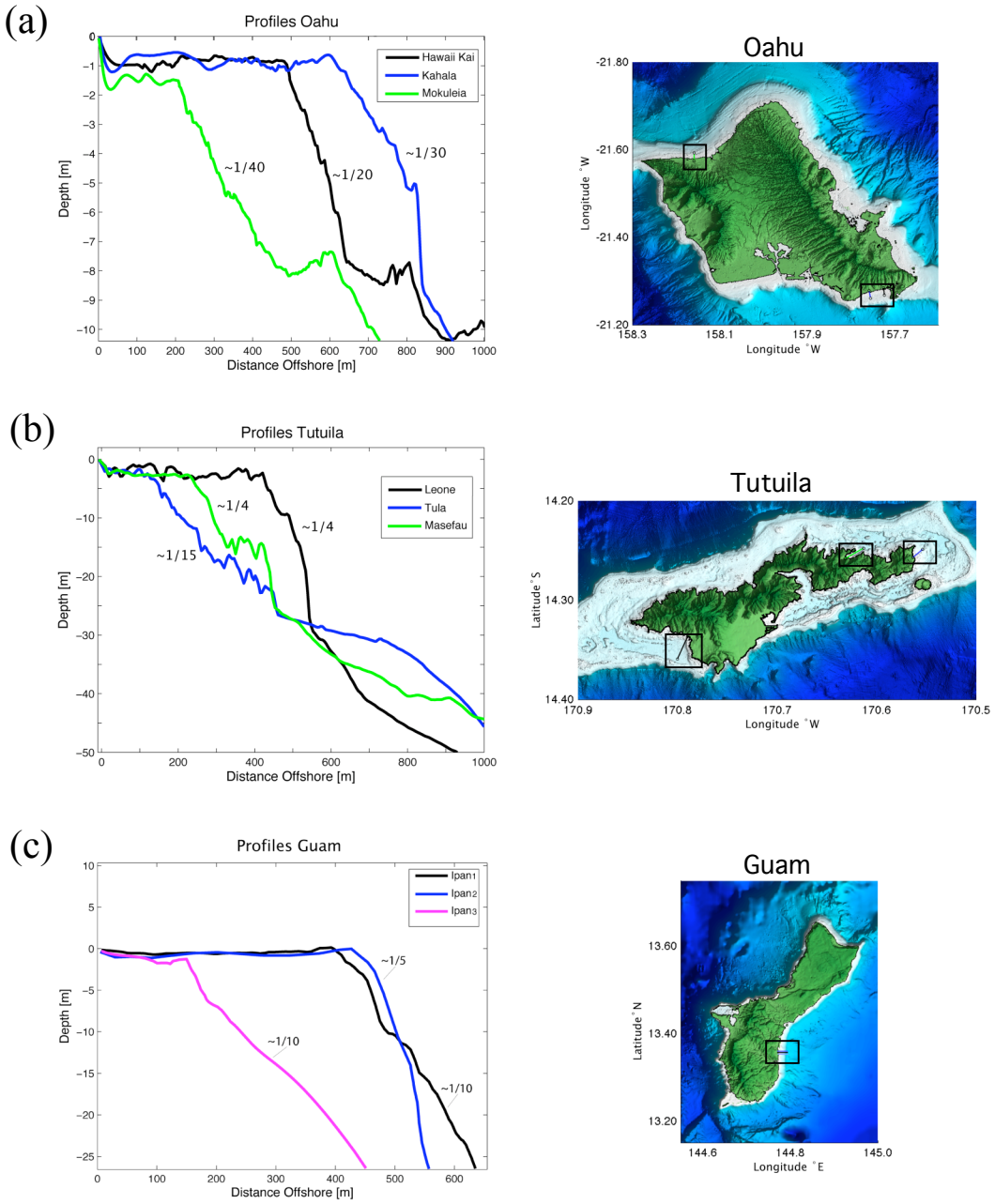

Figure 6.2. Profiles of fringing reef bathymetry. (a) Oahu, Hawaii; (b) Tutuila, American Samoa; (c) Guam. Black boxes indicate profile locations in each bathymetry plot respectively.

(a)

(b)

Figure 6.3. Constructed channels in the Tsunami Wave Basin at Oregon State University. (a) View from wavemaker. (b) View from end of channels.

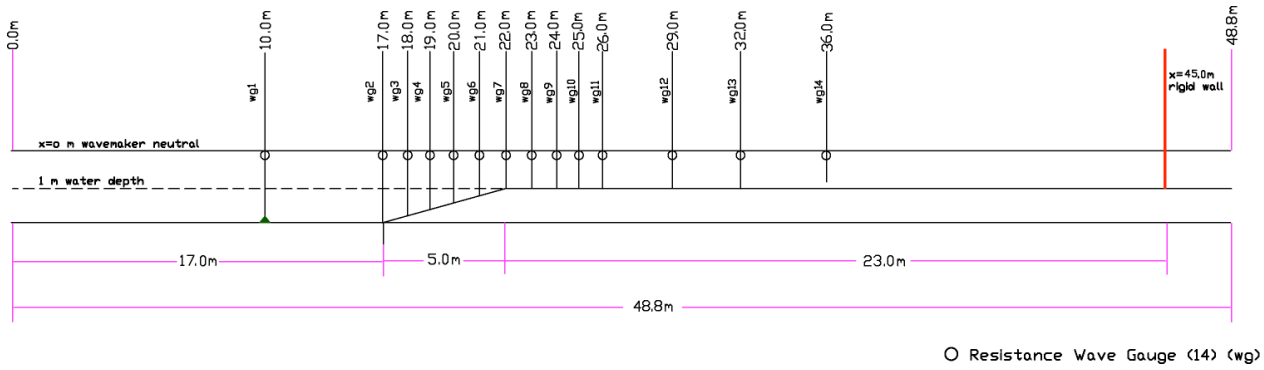

Figure 6.4. Two-dimensional reef model of 1:5 slope in the Tsunami Wave Basin at Oregon State University. Circles and vertical lines indicate wave gauge locations.

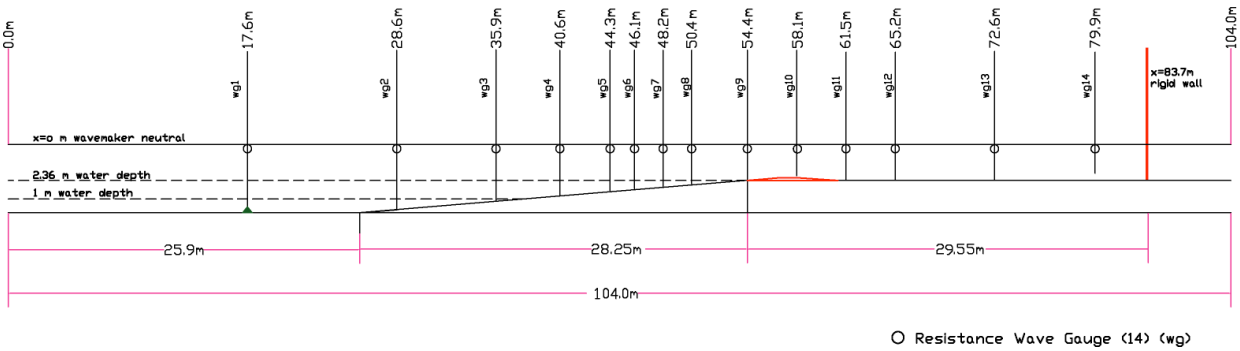

Figure 6.5. Two-dimensional reef model of 1:12 slope in the Large Wave Flume at Oregon State University. Circles and vertical lines indicate wave gauge locations.

(a)

(b)

(c)

Figure 6.6. Instruments used for laboratory experiments. (a) Resistance-type wire wave gauges. (b) Acoustic Doppler velocimeter (bottom), Ultra-sonic wave gauge (top right). (c) Wave propagating through TWB channel along instruments.

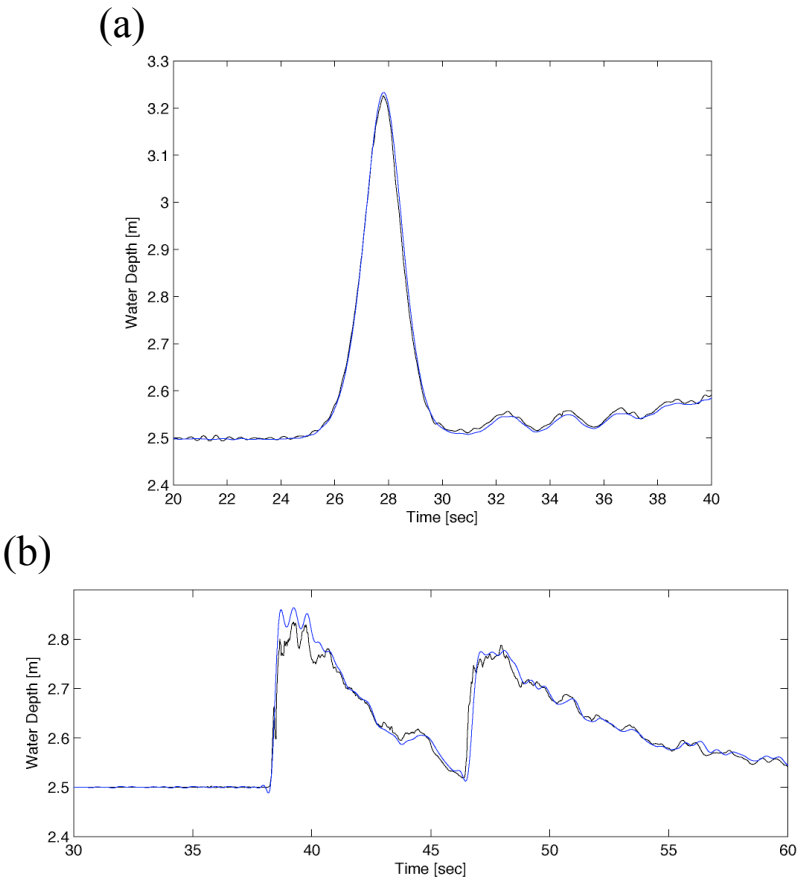

Figure 6.7. Comparison of ultra-sonic and resistance-type wire wave gauges in the Large Wave Flume. (a) At x = 17.64 m. (b) At x = 72.6 m. ——— (blue) Ultra-sonic wave gauge; ——— (black) resistance-type wire wave gauge.

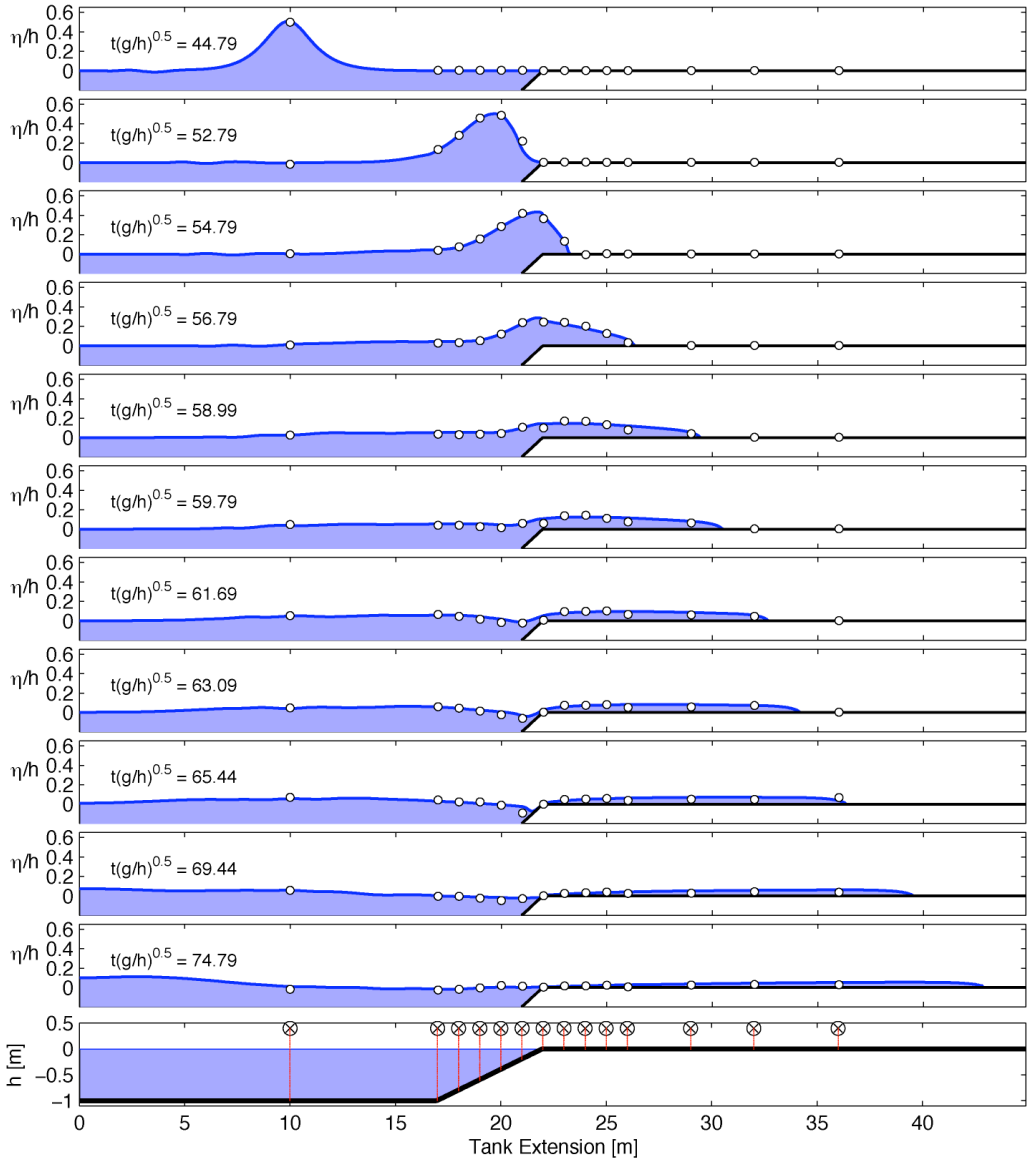

Figure 7.1. Snapshots of free surface profiles for propagation of solitary wave with A/h = 0.5 over 1:5 slope and dry reef flat. Solid lines and circles denote computed and measured data.

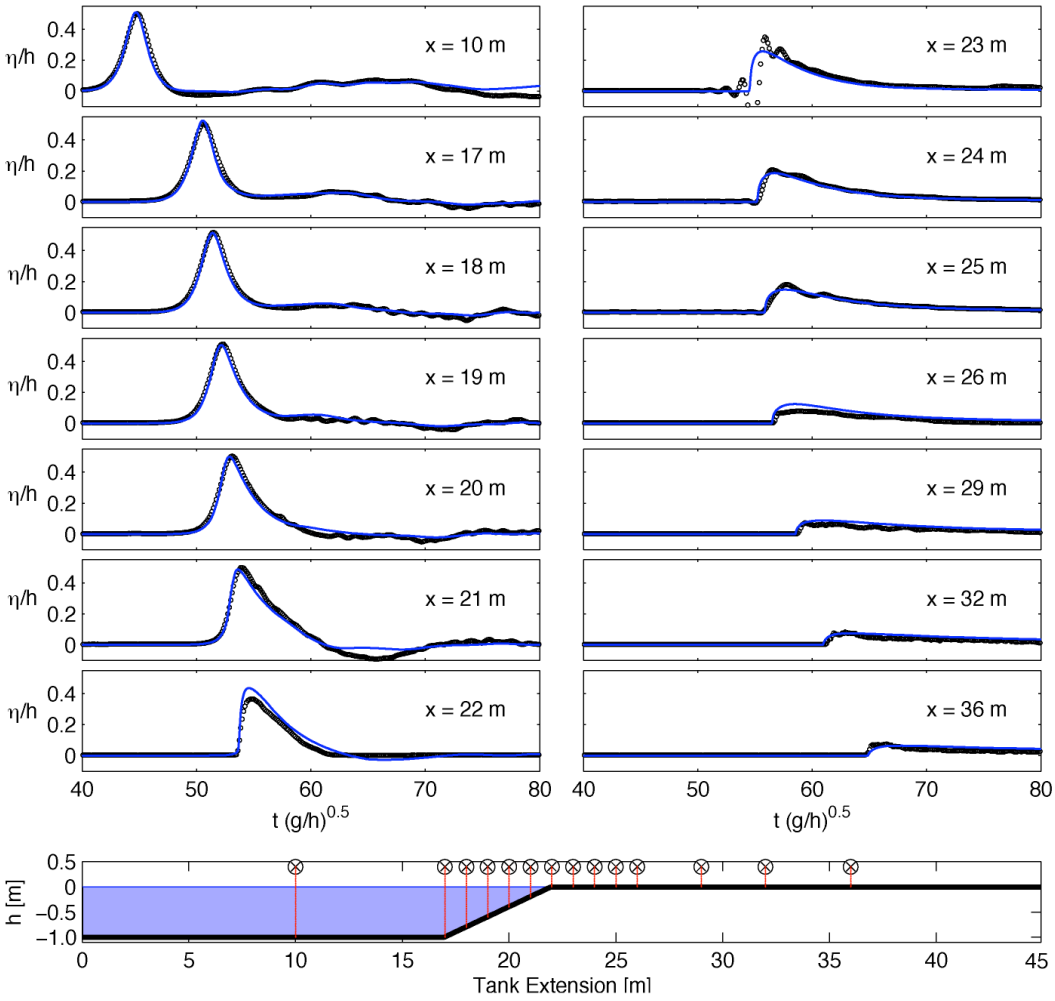

Figure 7.2. Time series of free surface profiles for propagation of solitary wave with A/h = 0.5 over 1:5 slope and dry reef flat. Solid lines and circles denote computed and measured data.

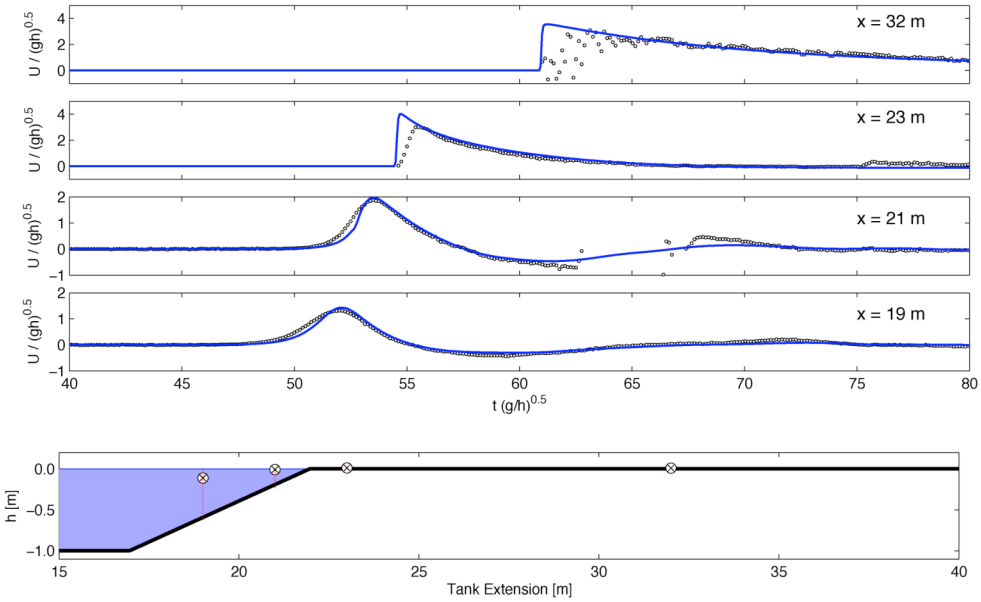

Figure 7.3 Velocity in x direction for propagation of solitary wave with $A/h = 0.5$ over 1:5 slope and dry reef flat. Solid lines and circles denote computed and measured data.

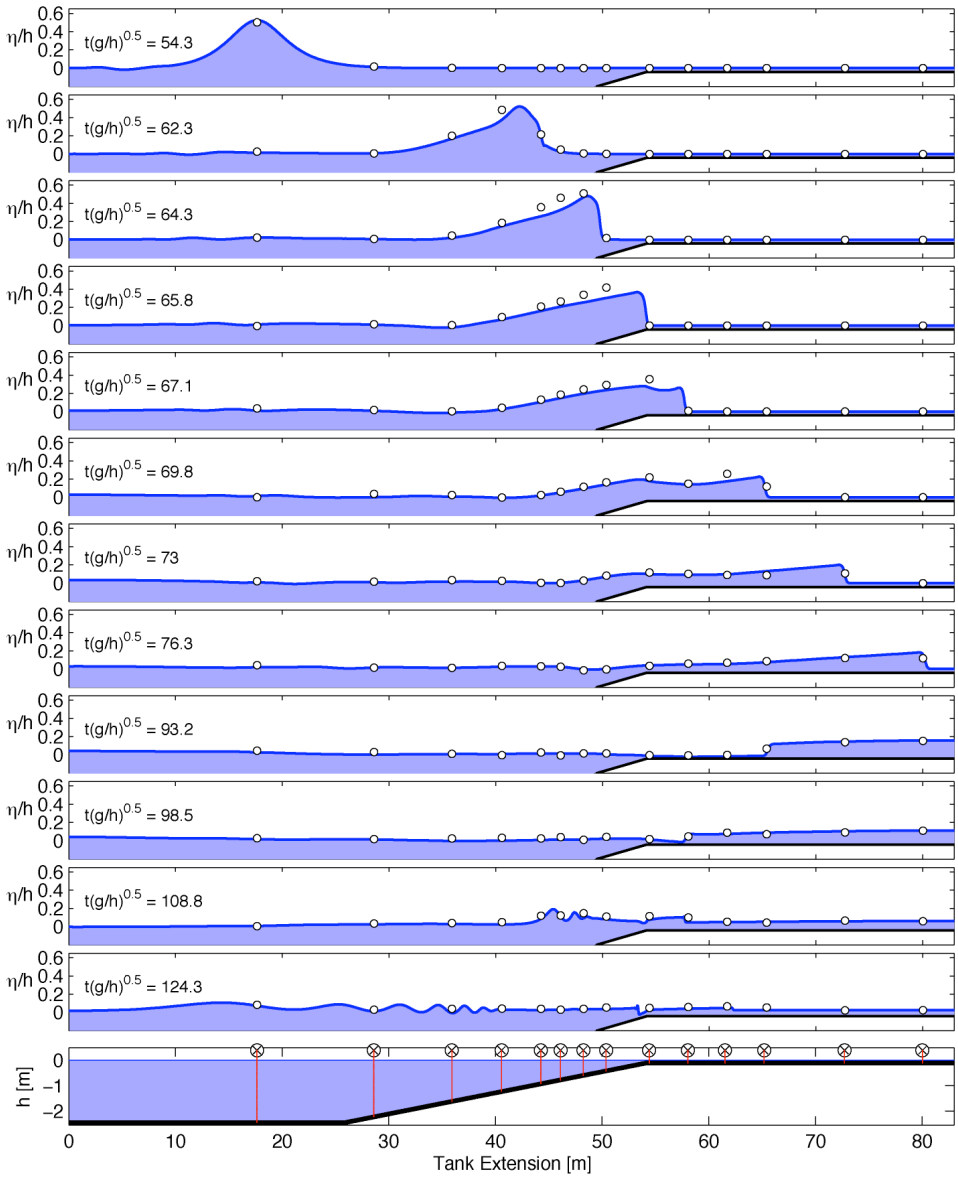

Figure 7.4. Snapshots of free surface profiles for propagation of solitary wave with A/h = 0.5 over 1:12 slope and reef flat submerged by 0.1 m of water. Solid lines and circles denote computed and measured data.

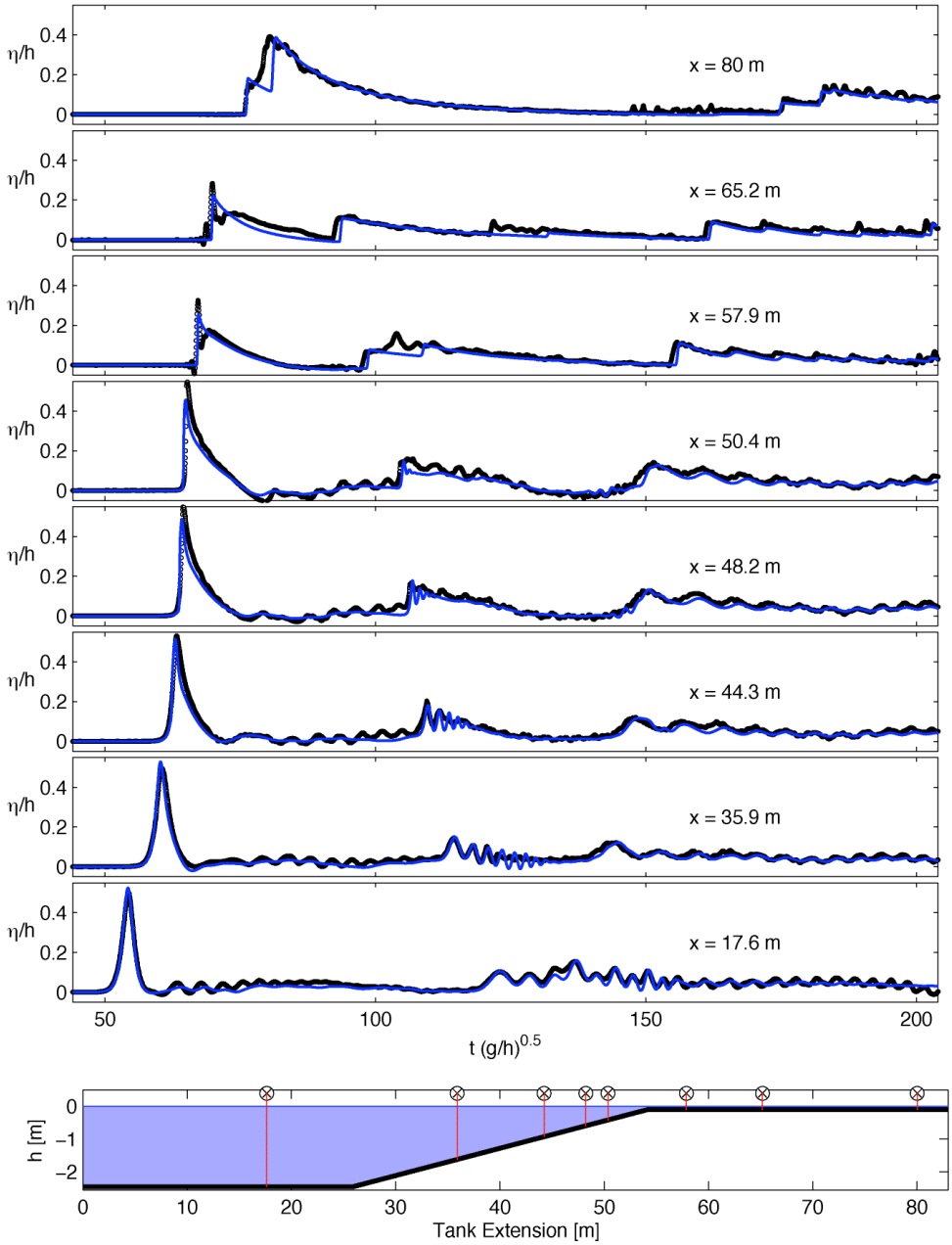

Figure 7.5. Time series of free surface profiles for propagation of solitary wave with A/h = 0.5 over 1:12 slope and reef flat submerged by 0.1 m of water. Solid lines and circles denote computed and measured data.

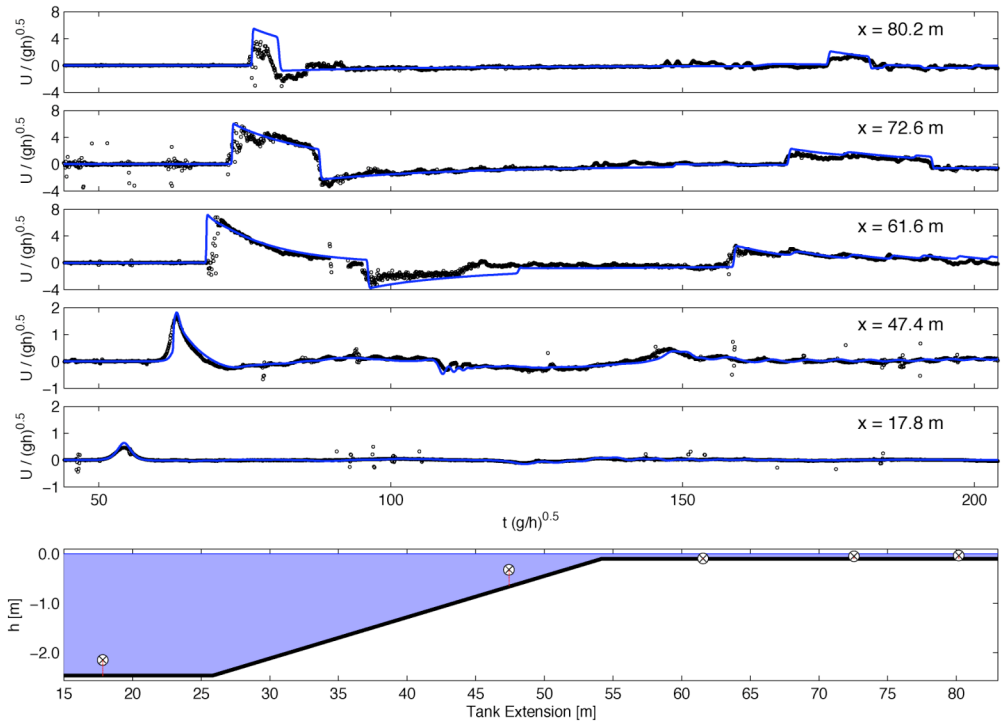

Figure 7.6. Velocity in x direction for propagation of solitary wave of A/h = 0.5 over 1:12 slope and reef flat submerged by 0.1 m of water. Solid lines and circles denote computed and measured data.

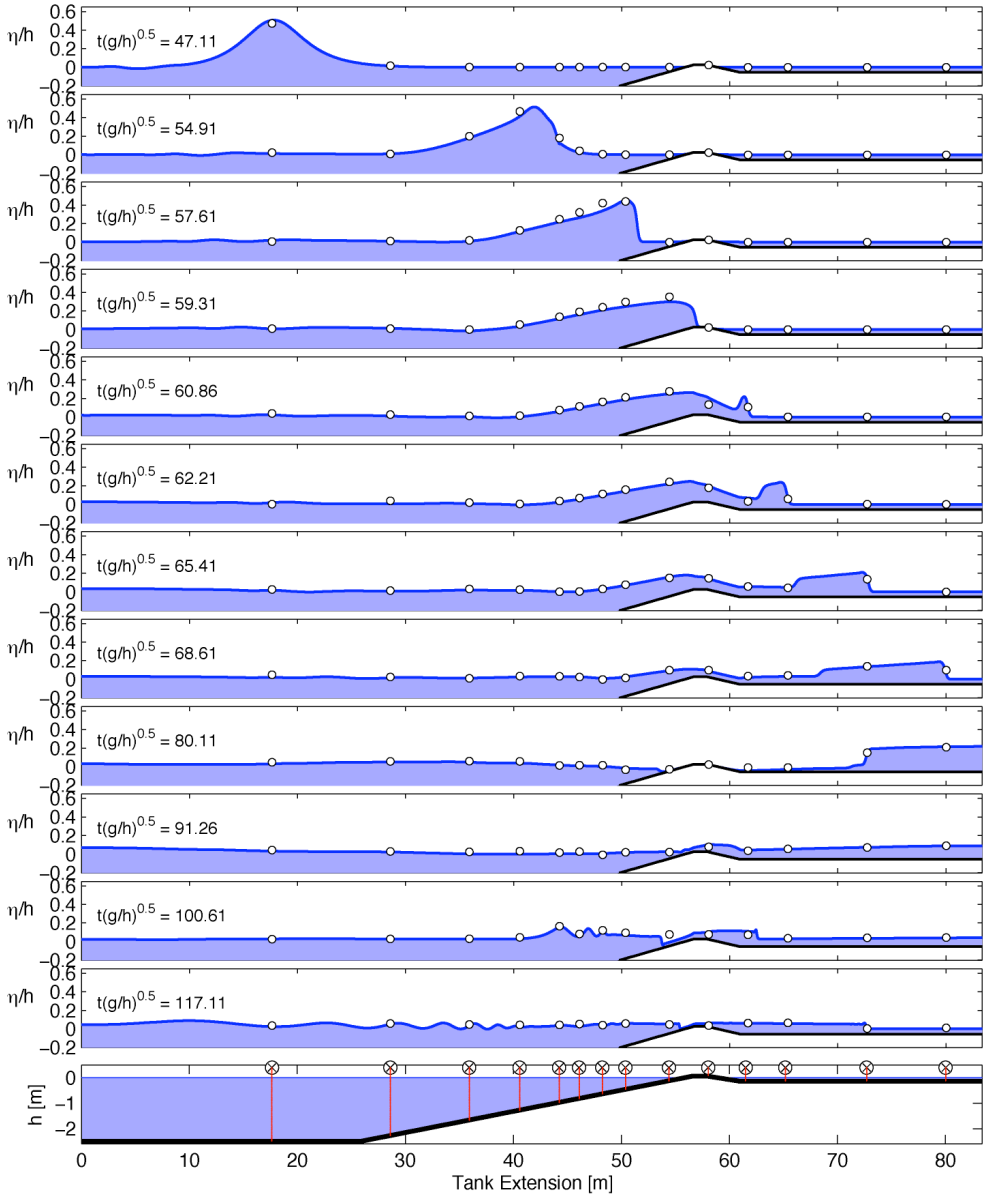

Figure 7.7. Snapshots of free surface profiles for propagation of solitary wave with A/h = 0.5 over 1:12 slope and exposed reef crest. Solid lines and circles denote computed and measured data.

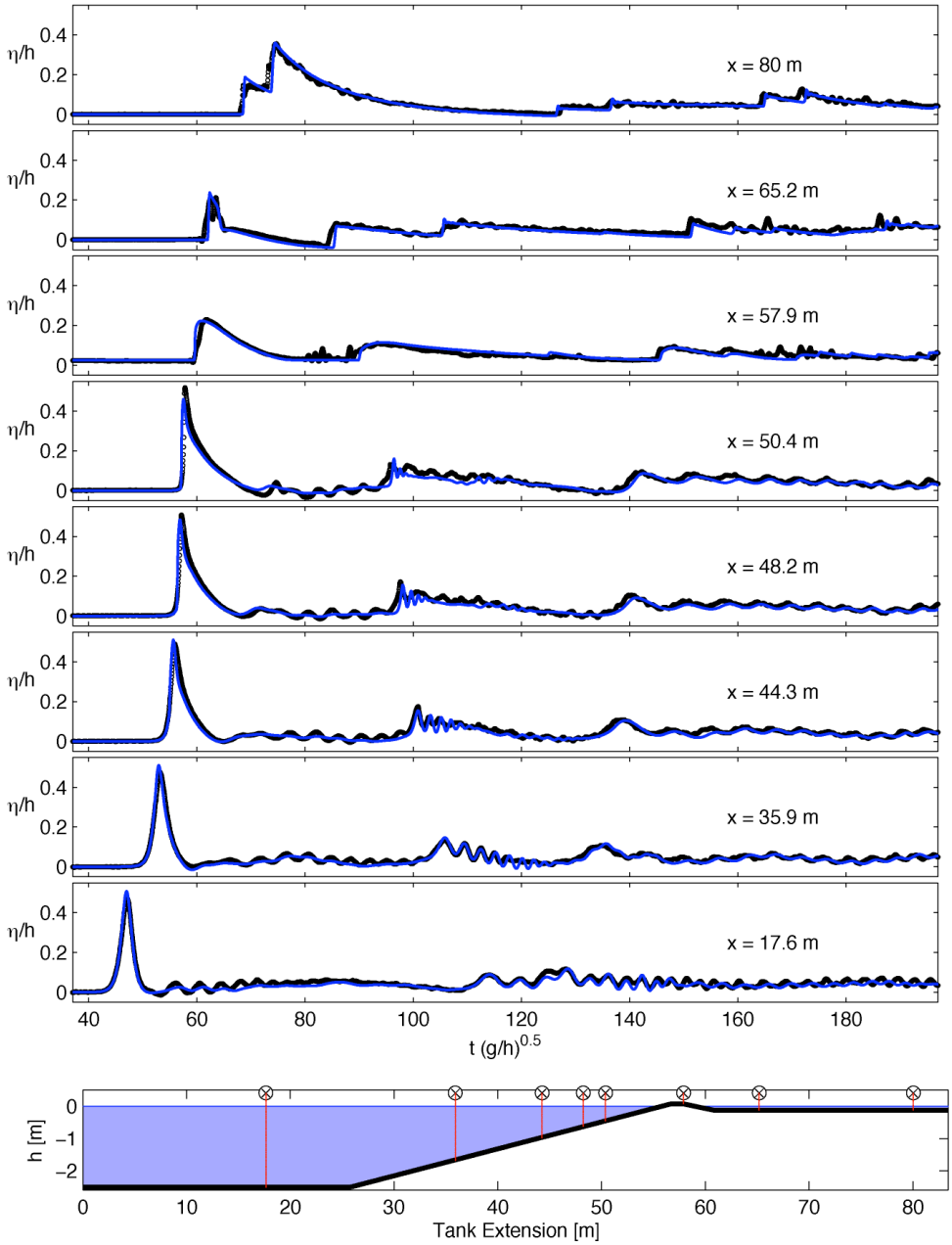

Figure 7.8. Time series of free surface profiles for propagation of solitary wave with A/h = 0.5 over 1:12 slope and exposed reef crest. Solid lines and circles denote computed and measured data.

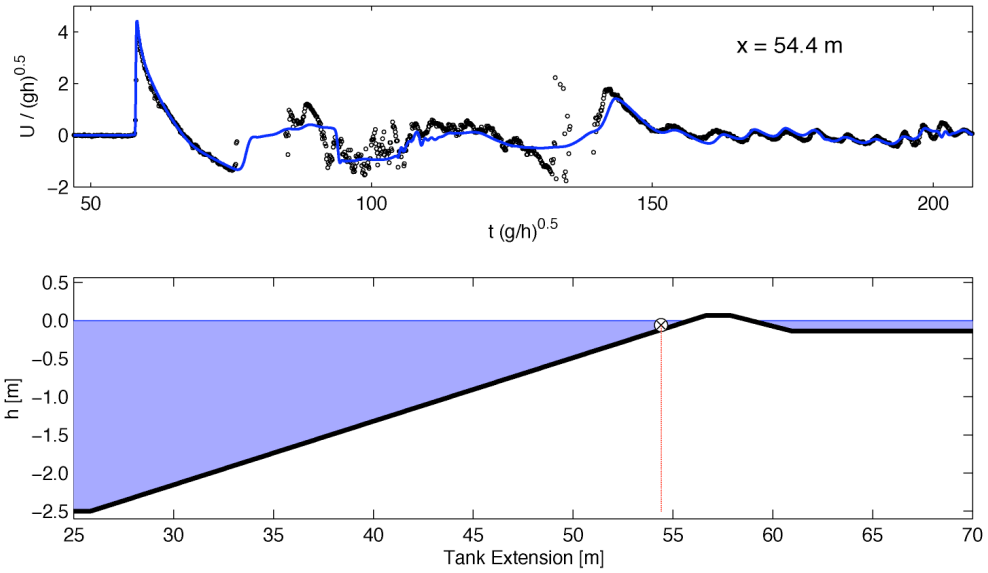

Figure 7.9. Velocity in x direction for propagation of solitary wave of $A/h = 0.5$ over 1:12 slope and exposed reef crest. Solid lines and circles denote computed and measured data.

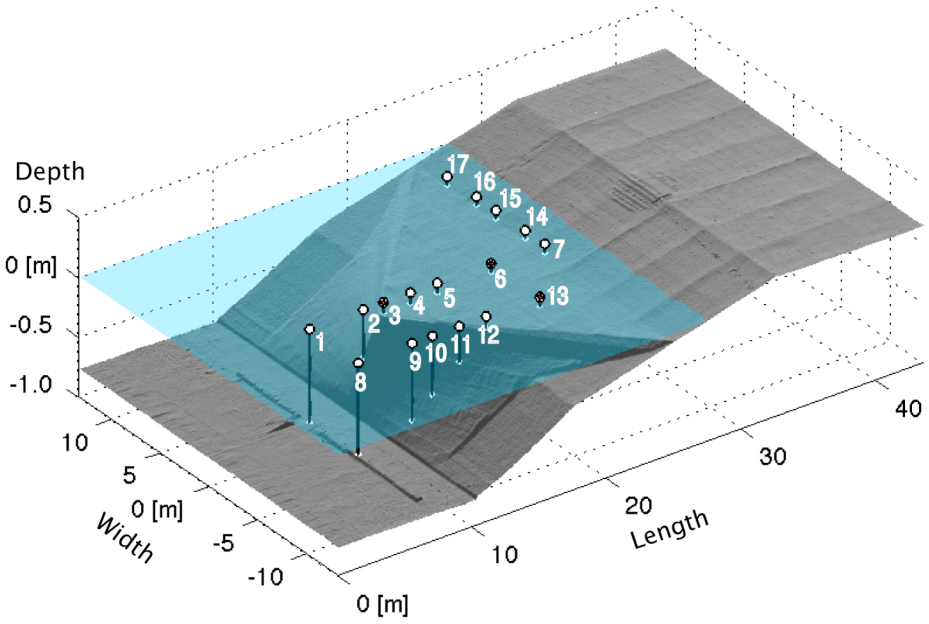

Figure 7.10. Perspective view of Benchmark I bathymetry from laser scan at original resolution of Δx = 5 cm. Circles denote wave gauge locations at free surface and corresponding location on tank bottom. Red crosses at gauges 3, 6, and 13 indicate positions of acoustic Doppler velocimeters for velocity measurements.

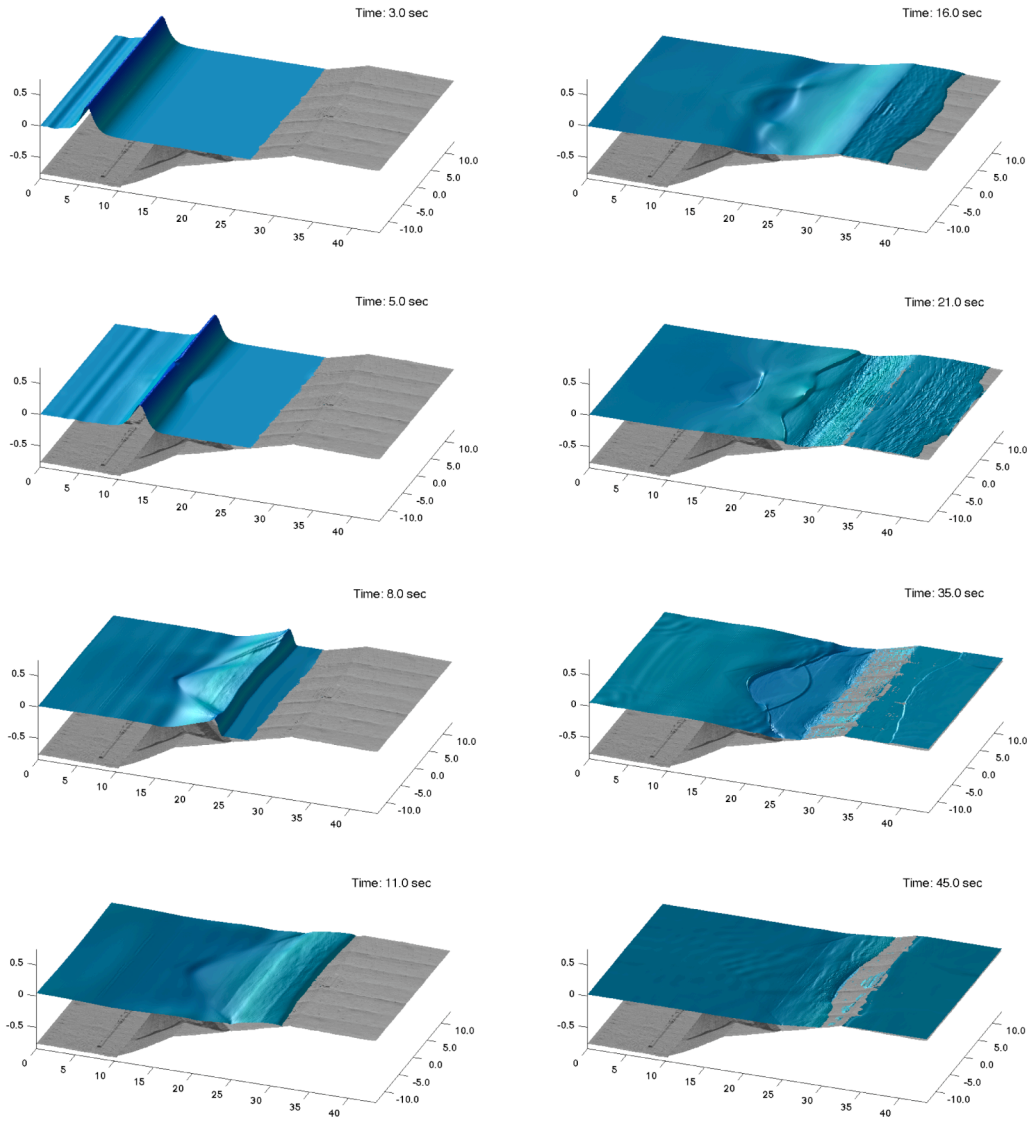

Figure 7.11. Snapshots of solitary wave transformation in Benchmark I.

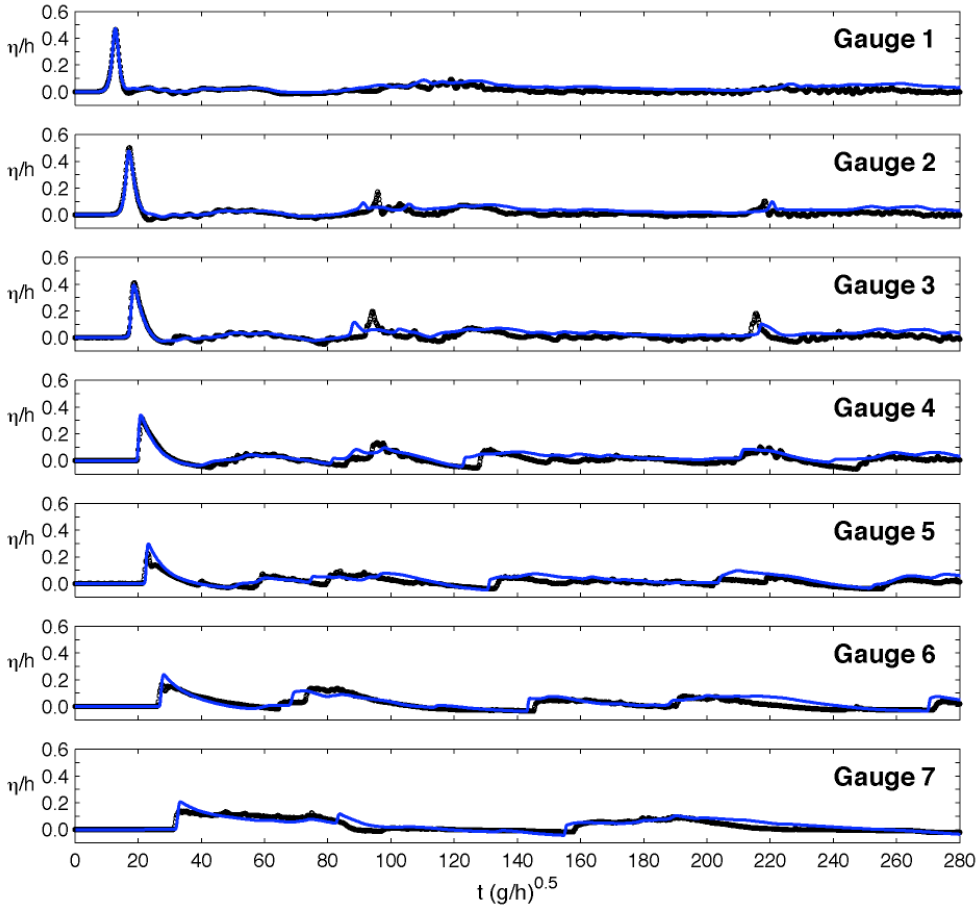

Figure 7.12. Time series of free surface profiles along basin centerline in Benchmark I. Solid lines and circles denote computed and measured data.

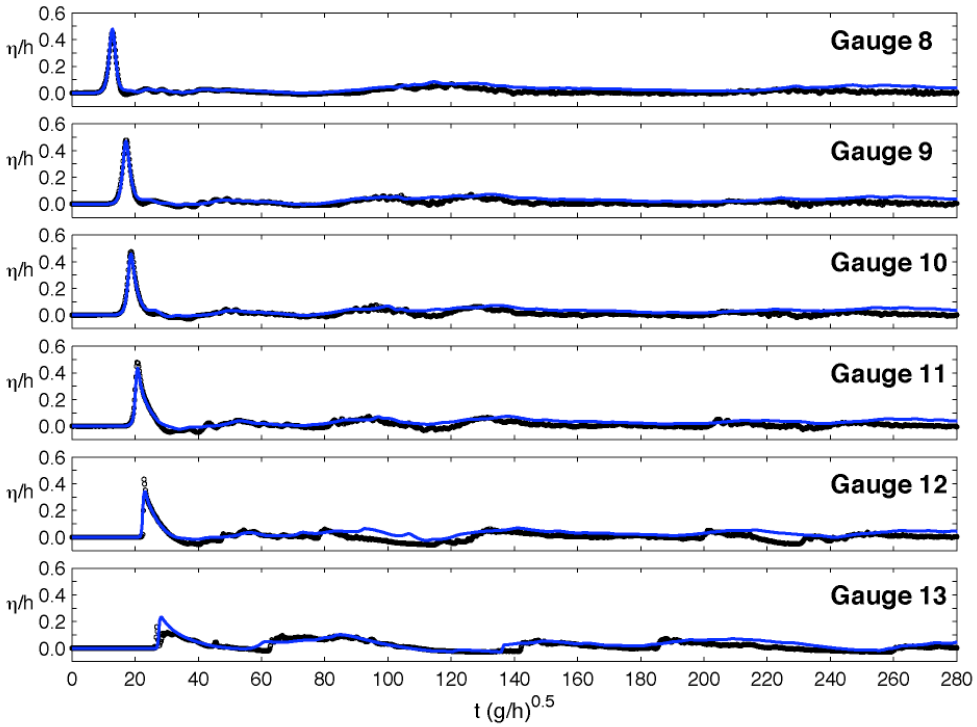

Figure 7.13. Time series of free surface profiles along transect at x = -5 m in Benchmark I. Solid lines and circles denote computed and measured data.

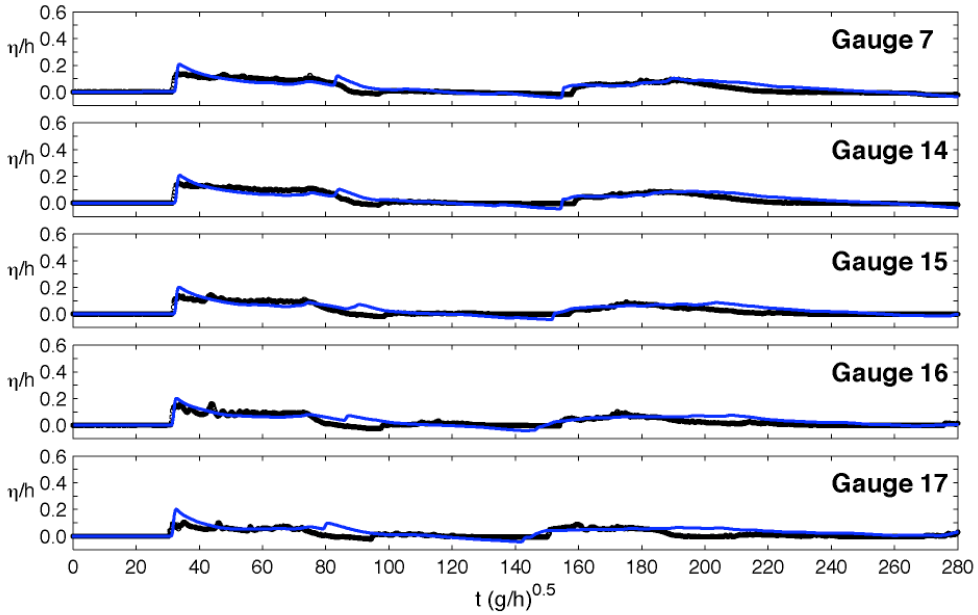

Figure 7.14. Time series of free surface profiles along longshore transect in Benchmark I. Solid lines and circles denote computed and measured data.

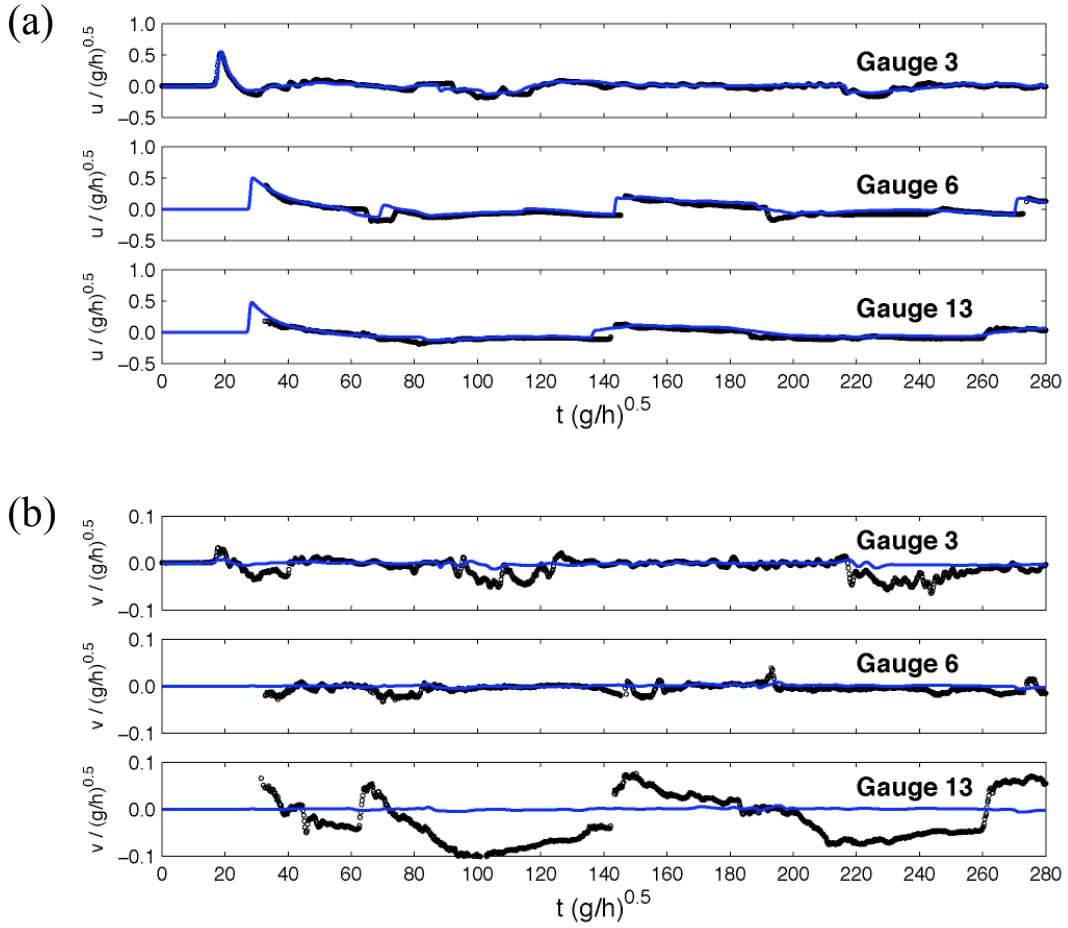

Figure 7.15. Time series of velocity in Benchmark I. (a) Cross-shore component. (b) Longshore component. Solid lines and circles denote computed and measured data.

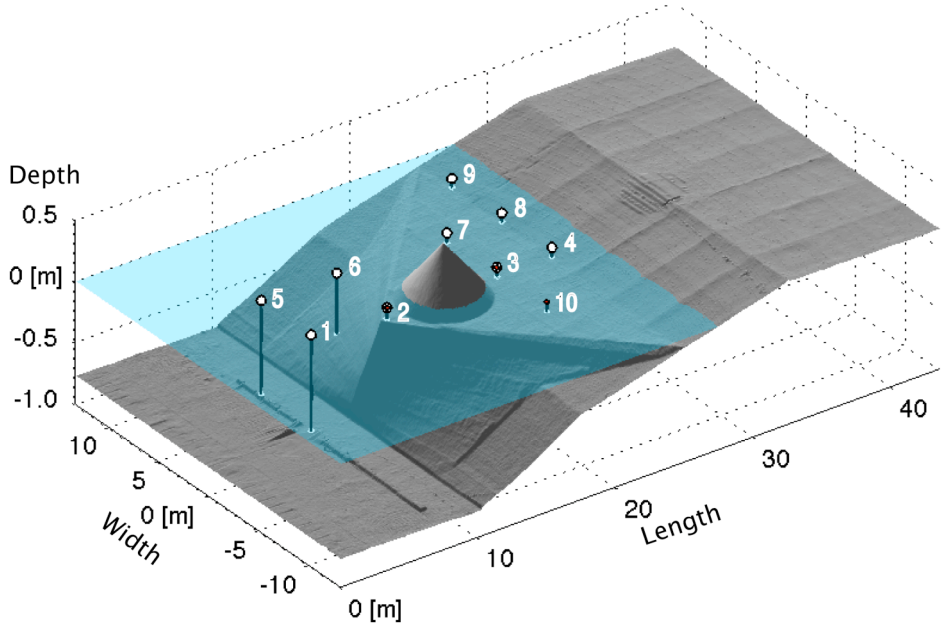

Figure 7.16. Perspective view of Benchmark II bathymetry from laser scan at original resolution of Δx = 5 cm. Conical island was added after laser scan. Circles denote wave gauge locations at free surface and corresponding location on tank bottom. Red crosses at gauges 2, 3, and 10 indicate positions of acoustic Doppler velocimeters for velocity measurements.

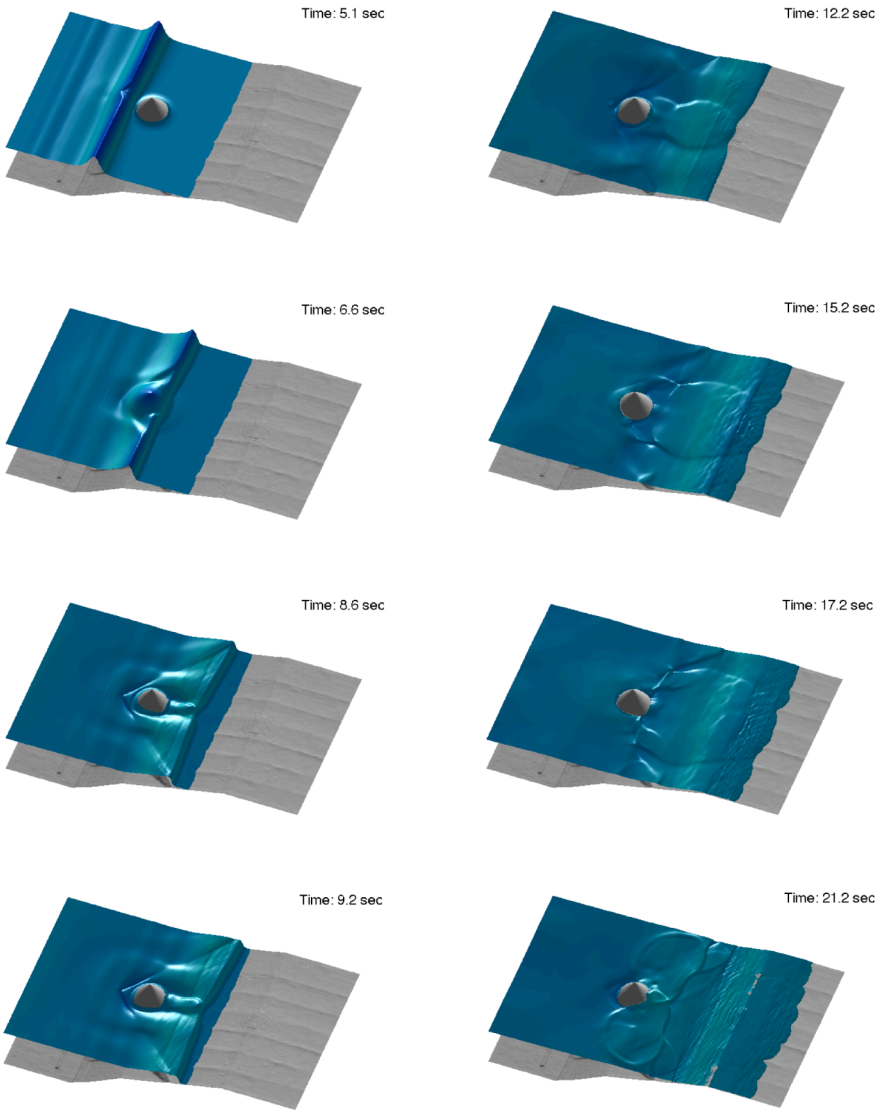

Figure 7.17. Snapshots of solitary wave transformation in Benchmark II.

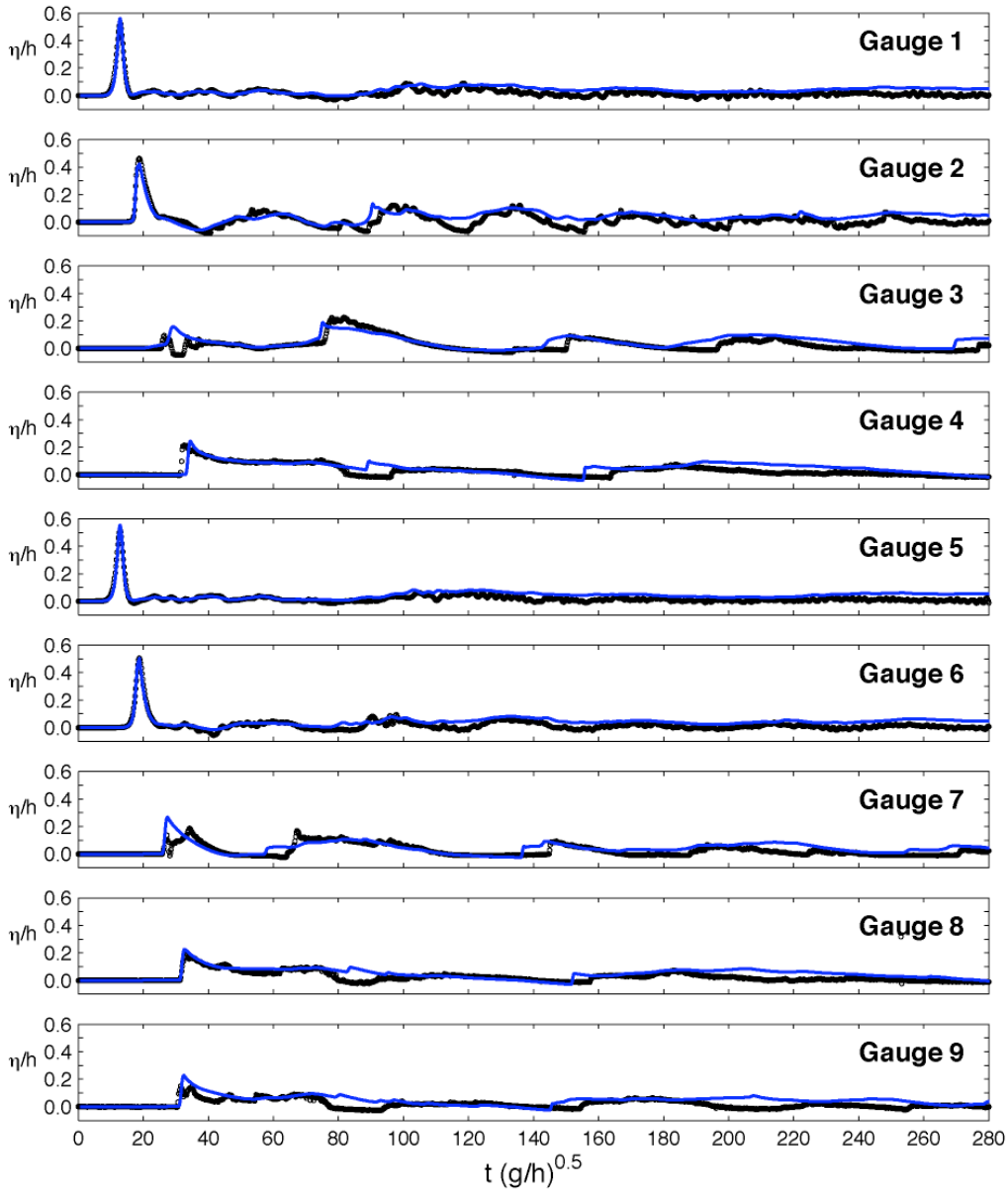

Figure 7.18. Time series of free surface profiles at wave gauges in Benchmark II. Solid lines and circles denote computed and measured data.

(a)

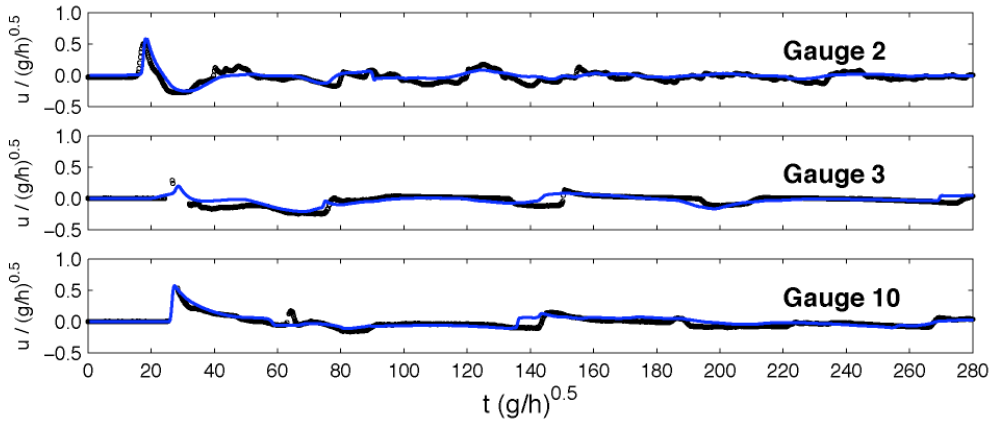

(b)

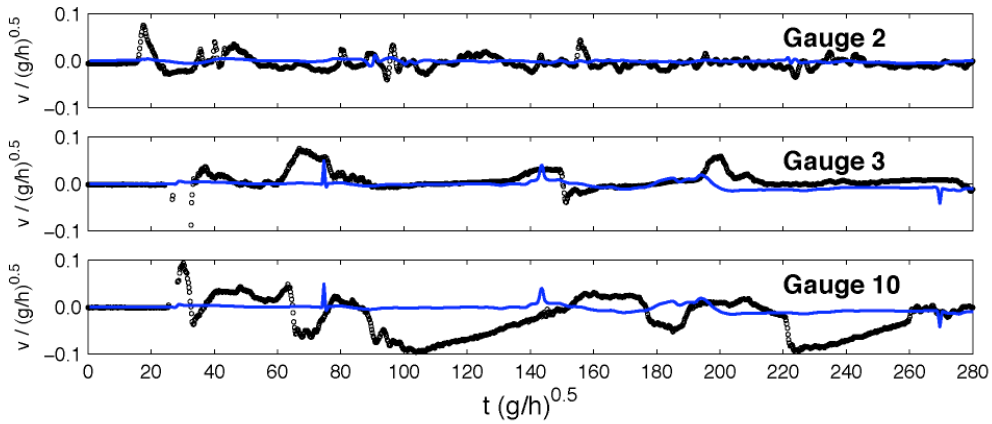

Figure 7.19. Time series of velocity in Benchmark II. (a) Cross-shore component. (b) Longshore component. Solid lines and circles denote computed and measured data.

REFERENCES

Beji, S., Battjes, J.A., 1993. Experimental investigation of wave propagation over a bar. *Coastal Engineering* 19 (1-2), 151-162.

Brocchini, M., Dodd, N., 2008. Nonlinear shallow-water equation modeling for coastal engineering. *Journal of Waterway, Port, Coastal, and Ocean Engineering* 134 (2), 104-120.

Begnudelli, L., Sanders, B.F., Bradford, S.F., 2008. Adaptive Godunov-based model for flood simulation. *Journal of Hydraulic Engineering* 134 (6), 714-725.

Burden, R.L., Faires, J.D., 2005. *Numerical Analysis*, Eighth Edition. Thomson, Brooks/Cole, Belmont.

Casulli, V., and Stelling, G.S. (1998). Numerical simulation of 3D quasi-hydrostatic, free-surface flows. *Journal of Hydraulic Engineering*, 124 (7), 678-686.

Chang, Y.-H., Hwang, K.-S., Hwung, H.-H., 2009. Large-scale measurements of solitary wave inundation on a 1:20 slope. *Coastal Engineering* 56 (3), 1022-1034.

Chaudhry, M.H. (1993). *Open-Channel Flow*. Prentice-Hall Inc., Englewood Cliffs, New Jersey.

Cho, Y.S., Liu, P.L.-F., 1999. Crest length effects in nearshore tsunami run-up around islands. *Journal of Geophysical Research* 104, 7907–7913.

Choi, B.H., Hong, S.J., Pelinovsky, E., 2006. Distribution of runup heights of the December 26, 2004 tsunami in the Indian Ocean. *Geophysical Research Letters* 33, L13601. doi:10.1029/2006GL025867.

Demirbilek, Z., Nwogu, O.G., 2007. Boussinesq Modeling of Wave Propagation and Runup over Fringing Coral Reefs, Model Evaluation Report. US Army Corps of Engineers, *Report ERDC/CHL TR-07-12*, Vicksburg, Mississippi.

Dodd, N., 1998. Numerical model of wave run-up, overtopping, and regeneration. *Journal of Waterway, Port, Coastal and Ocean Engineering* 124 (2), 73-81.

Fuhrman, D.R., Madsen, P.A., 2009. Tsunami generation, propagation, and run-up with a higher order Boussinesq model. *Coastal Engineering* 56 (7), 747–758.

George, D.L. (2010). Adaptive finite volume methods with well-balanced Riemann solvers for modeling floods in rugged terrain: Application to the Malpasset dam-break flood (France, 1959). *International Journal for Numerical Methods in Fluids*, DOI:10.1002/fld.2298, in press.

Gobbi, M.F., Kirby, J.T., Wei, G., 2000. A fully nonlinear Boussinesq model for surface waves. Part 2. Extension to $O(kh)^4$. *Journal of Fluid Mechanics* 405, 181-210.

Gourlay, M. R., 1996a. Wave set-up on coral reefs. 1. Set-up and wave-generated flow on an idealized two dimensional horizontal reef. *Coastal Engineering*, 27, 161-193.

Gourlay, M. R.,1996b. Wave set-up on coral reefs. 2. Set-up on reefs with various profiles. *Coastal Engineering*, 28, 17-55.

Ferziger, J.H., Peric, M., 2002. *Computational Methods for Fluid Dynamics*. 3rd Edition, Springer-Verlag, Berlin, Heidelberg, New York.

Hall, J.V., Watts, J.W., 1953. Laboratory investigation of the vertical rise of solitary waves on impermeable slopes. *Technical Memo No. 33*, Beach Erosion Board, US Army Corps of Engineers.

Heitner, K. L., and Housner, G.W., 1970. Numerical model for tsunami runup. *Journal of Waterway, Port, Coastal, and Ocean Engineering*, 96, 701-719.

Horrillo, J.J., Kowalik, Z., and Shigihara, Y. (2006). Wave dispersion study in the Indian Ocean tsunami of December 26, 2004. *Marine Geodesy*, 29(1), 149-166.

Kennedy, A.B., Chen, Q., Kirby, J.T., Dalrymple, R.A., 2000. Boussinesq modeling of wave transformation, breaking, and runup. Part I: 1D. *Journal of Waterway, Port, Coastal, and Ocean Engineering* 126 (1), 39-47.

Kim, K.H., Kim, C., 2005. Accurate, efficient and monotonic numerical methods for multi-dimensional compressible flows Part II: Multi-dimensional limiting process. *Journal of Computational Physics* 208 (1), 570-615.

LeVeque, R.J., 2002. Finite Volume Methods for Hyperbolic Problems. Cambridge University Press, Cambridge.

Li, Y., Raichlen, F., 2002. Non-breaking and breaking solitary wave run-up. *Journal of Fluid Mechanics* 456, 295-318.

Liu, P.L.-F., 1994. Model equations for wave propagation from deep to shallow-water. In: Liu, P.L.-F. (Ed.), *Advances in Coastal Engineering*, vol. 1, pp. 125-157.

Liu, P.L.-F., Cho, Y.S., Briggs, M.J., Kanoglu, U., Synolakis, C.E., 1995a. Runup of solitary waves on a circular island. *Journal of Fluid Mechanics* 302, 259–285.

Liu, P.L.-F., Cho, Y.S., Yoon, S.B., Seo, S.N., 1995b. Numerical simulations of the 1960 Chilean tsunami propagation and inundation at Hilo, Hawaii. In: Tsuchiya, Shuto (Eds.), Tsunami: Progress in Prediction, Disaster Prevention and Warning. Kluwer Academic Publishers, pp. 99–115.

Liu, P.L.-F., Synolakis, C., Yeh, H., 1991. A report on the international workshop on long wave runup. *Journal of Fluid Mechanics* 229, 678–688.

Luth, H.R., Klopman, G., Kitou, N., 1994. Project 13G: Kinematics of waves breaking partially on an offshore bar; LDV measurements for waves with and without a net onshore current. *Technical Report H1573*, Delft Hydraulics, The Netherlands.

Lynett, P.J., Wu, T.R., Liu, P.L.F., 2002. Modeling wave runup with depth-integrated equations. *Coastal Engineering* 46 (2), 89-107.

Madsen, P.A., Bingham, H.B., Schäffer, H.A., 2003. Boussinesq-type formulations for fully nonlinear and extremely dispersive water waves: derivation and analysis. *Proceedings of the Royal Society of London* A 459, 1075–1104.

Madsen, P.A., Schäffer, H.A., 1998. Higher order Boussinesq-type equations for surface gravity waves-Derivation and analysis. *Philosophical Transactions of the Royal Society of London* A 356, 3123-3186.

Madsen, P.A., Sørensen, O.R., 1992. A new form of the Boussinesq equations with improved linear dispersion characteristics. Part 2. A slowly-varying bathymetry. *Coastal Engineering* 18 (3-4), 183-204.

Madsen, P.A., Sørensen, O.R., Schäffer, H.A., 1997. Surf zone dynamics simulated by a Boussinesq type model. Part I. Model description and cross-shore motion of regular waves. *Coastal Engineering* 32 (4), 255-287.

Mori, N., T. Suzuki and S. Kakuno (2007) Noise of acoustic Doppler velocimeter data in bubbly flow, *Journal of Engineering Mechanics*, American Society of Civil Engineers, 133 (1), 122-125.

Munger, S. and Cheung, K.F. 2008. Resonance in Hawaii waters from the 2006 Kuril Islands Tsunami. *Geophysical Research Letters* 35 (7), L07605, Doi: 10.1029/2007GL032843.

Nwogu, O., 1993. An alternative form of the Boussinesq equations for nearshore wave propagation. *Journal of Waterway, Port, Coastal, and Ocean Engineering* 119 (6), 618-638.

Pan, C.H., Lin, B.Y., Mao, X.Z., 2007. Case study: numerical modeling of the tidal bore on the Qiantang River, China. *Journal of Hydraulic Engineering* 133 (2), 130-138.

Peregrine, D.H., 1967. Long waves on a beach. *Journal of Fluid Mechanics* 27, 815-827.

Roeber, V., K. F. Cheung, and M. H. Kobayashi (2010), Shock-capturing Boussinesq-type model for nearshore wave processes, *Coastal Engineering*, 57 (4), 407–423.

Roeber, V., Y. Yamazaki, and K. F. Cheung (2010), Resonance and impact of the 2009 Samoa tsunami around Tutuila, American Samoa, *Geophysical Research Letters*, 37, L21604, doi:10.1029/2010GL044419.

Schäffer H.A., Madsen, P.A., Deigaard, R., 1993. A Boussinesq model for waves breaking in shallow-water. *Coastal Engineering* 20 (3-4), 185-202.

Seelig, W., 1983. Laboratory study of reef-lagoon system hydraulics. *Journal of Waterway, Port, Coastal, Ocean Engineering* 109 (4), 380-391.

Skotner, C., and Apelt, C. J., 1999. Application of a Boussinesq model for the computation of breaking waves. Part II: Wave-induced setdown and setup on a submerged coral reef. *Ocean Engineering* 26, 927-947.

Smagorinsky, J., 1963. General circulation experiments with the primitive equations. *Monthly Weather Review* 91, 99-164.

Stelling, G., Zijlema, M., 2003. An accurate and efficient finite-difference algorithm for non-hydrostatic free-surface flow with application to wave propagation. *International Journal for Numerical Methods in Fluids* 43 (1), 1-23.

Svendsen, I.A., 1984. Wave heights and setup in a surf zone. *Coastal Engineering* 8 (4), 303-329.

Swigler, D.T., 2009. Laboratory study investigating the three-dimensional turbulence and kinematic properties associated with a breaking solitary wave. MSc thesis, Texas A&M University.

Synolakis, C.E., 1987. The runup of solitary waves. *Journal of Fluid Mechanics* 185, 523-545.

Ting, F.C.K., Kirby, J.T., 1994. Observation of undertow and turbulence in a laboratory surf zone. *Coastal Engineering* 24 (3-4), 51-80.

Titov, V.V., Synolakis, C.E., 1995. Modeling of breaking and nonbreaking long-wave evolution and runup using VTCS-2. *Journal of Waterway, Port, Coastal, and Ocean Engineering* 121 (6), 308-316.

Titov, V.V. and Synolakis, C.E. (1998). Numerical modeling of tidal wave runup. *Journal of Waterway, Port, Coastal, and Ocean Engineering*, 124 (4), 157-171.

Toro, E.F., 2001. Shock-Capturing Methods for Free-Surface Shallow Flows. Wiley, New York.

Veeramony, J., Svendsen, I.A., 2000. The flow in the surf-zone waves. *Coastal Engineering* 39 (2-4), 93-122.

Von Neumann, J., Richtmyer, R.D., 1950. A Method for the numerical calculation of hydrodynamic shocks. *Journal of Applied Physics* 21, 232-237.

Wei, G., Kirby, J.T., 1995. A time-dependent numerical code for extended Boussinesq equations. *Journal of Waterway, Port, Coastal, and Ocean Engineering* 120, 251-261.

Wei, G., Kirby, J.T., Grilli, S.T., Subramanya, R., 1995. A fully nonlinear Boussinesq model for surface waves: Part I. Highly nonlinear unsteady waves. *Journal of Fluid Mechanics* 294, 71-92.

Wei, Y., Mao, X.Z., Cheung, K.F., 2006. Well-balanced finite-volume model for long-wave runup. *Journal of Waterway, Port, Coastal, and Ocean Engineering* 132 (2), 114-124.

Wu, Y., Cheung, K.F., 2008. Explicit solution to the exact Riemann problem and application in nonlinear shallow-water equations. *International Journal for Numerical Methods in Fluids* 57 (11), 1649-1668.

Yamazaki, Y., Kowalik, Z., Cheung, K.F., 2009. Depth-integrated, non-hydrostatic model for wave breaking and run-up. *International Journal for Numerical Methods in Fluid* 61, 473-497.

Yamazaki, Y., K. F. Cheung, and Z. Kowalik (2010), Depth-integrated, non-hydrostatic model with grid nesting for tsunami generation, propagation, and run-up, *International Journal for Numerical Methods in Fluid*, doi:10.1002/fld.2485, in press.

Yeh, H., Liu, P., Synolakis, C. (Eds.), 1996. Long-wave Runup Models. World Scientific.

Zelt, J.A., 1991. The runup of nonbreaking and breaking solitary waves. *Coastal Engineering* 15 (3), 205-246.

Zijlema, M. and Stelling, G.S. (2008). Efficient computation of surf zone waves using the nonlinear shallow water equations with non-hydrostatic pressure. *Coastal Engineering*, 55 (10), 780-790.

Zhou, J.G., Causon, D.M., Mingham, C.G., Ingram, D.M., 2001. The surface gradient method for the treatment of source terms in the shallow-water equations. *Journal of Computational Physics* 168 (1), 1-25.

APPENDIX

In the following, we look at the solution of an isolated right moving shock wave. The left and the right states of water depth, h, and flow velocity, u, for the Rankine-Hugoniot condition are

$$\mathbf{W}_* = \begin{bmatrix} h_* \\ u_* \end{bmatrix}; \quad \mathbf{W_R} = \begin{bmatrix} h_L \\ u_L \end{bmatrix}. \tag{A.1}$$

The shock wave involves three constant states, namely $\mathbf{U}_L$ to the left, $\mathbf{U}_R$ to the right, and a new constant state, $\mathbf{U}_*$, valid in the region between the left and the right states. This region is denoted as star region and it connects the known left and right states, which run into the shock path as illustrated here:

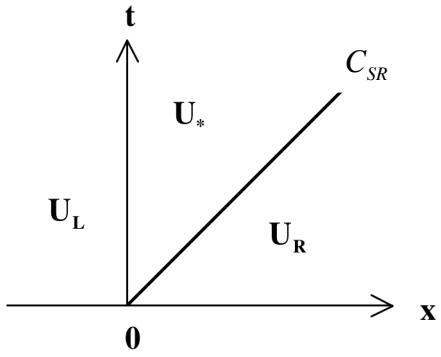

Applying a frame of reference moving to the right with the shock at speed C_{SR}, leads to the transformation of the equations as

The relative velocities among the frame of reference can be expressed as

$$\bar{u}_* = u_* - C_{SR} \quad ; \quad \bar{u}_R = u_R - C_{SR}. \tag{A.2}$$

For the flow situation involving $\bar{u}_*$ and $\bar{u}_R$ the vectors of conserved variables are

$$\bar{\mathbf{U}}_* = \begin{bmatrix} h_* \\ h_* \bar{u}_* \end{bmatrix} \; ; \; \bar{\mathbf{U}}_R = \begin{bmatrix} h_R \\ h_R \bar{u}_R \end{bmatrix}. \tag{A.3}$$

For the transformed frame of reference the Rankine-Hugoniot condition results in

$$h_* \bar{u}_* = h_R \bar{u}_R, \tag{A.4}$$

$$h_* \bar{u}_*^2 + \frac{1}{2} g h_*^2 = h_R \bar{u}_R^2 + \frac{1}{2} g h_R^2. \tag{A.5}$$

The mass flux through the shock can be stated as

$$M_R \equiv -h_* \bar{u}_* = -h_R \bar{u}_R, \tag{A.6}$$

which leads to

$$\bar{u}_* = -\frac{M_R}{h_*} \text{ and } \bar{u}_R = -\frac{M_R}{h_R}. \tag{A.7}$$

A.5 gives

$$M_R = -\frac{1}{2} g \frac{h_*^2 - h_R^2}{\bar{u}_* - \bar{u}_R}. \tag{A.8}$$

Substituting (A.7) into (A.8) results in an expression for the right mass flux as

$$M_R = \sqrt{\frac{1}{2} g \left(h_* + h_R \right) h_R h_*} \; . \tag{A.9}$$

Multiplication of the Rankine-Hugoniot condition by $h_R u_*$ leads to

$$h_R h_* \bar{u}_*^2 + \frac{1}{2} g h_R h_*^3 = h_R^2 \bar{u}_R^3 + \frac{1}{2} g h_R^3 h_*, \tag{A.10}$$

which is

$$\left(h_R - h_* \right) = \frac{1}{2} g h_R^3 h_* - \frac{1}{2} g h_R h_*^3. \tag{A.11}$$

The velocity in the star region can be defined in terms of a function f_R governing the flow quantities across h_* and h_R respectively by

$$u_* = u_R + f_R(h_*, h_R). \tag{A.12}$$

The function is then expressed as

$$f_R(h_*, h_R) = (h_* - h_R)\sqrt{g\frac{h_* + h_R}{2h_R h_*}}. \tag{A.13}$$

It is possible to obtain a relation for the shock speed, C_{SR}, by using $\bar{u}_* = u_* - C_{SR}$, $\bar{u}_R = u_R - C_{SR}$, and $M_R \equiv -h_*\bar{u}_* = -h_R\bar{u}_R$ leading to

$$C_{SR} = u_R + \frac{M_R}{h_R}. \tag{A.14}$$

By using the shallow-water celerity $a_R = \sqrt{gh_R}$ and the equation above, we can also write the shock speed as

$$C_{SR} = u_R + a_R q_R \tag{A.15}$$

with

$$q_R = \sqrt{\frac{(h_* + h_R)h_*}{2h_R^2}}. \tag{A.16}$$

By introducing Froude numbers like F_{rS} for the shock and F_{rR} ahead of the shock as

$$F_{rS} = \frac{C_{SR}}{a_R} \text{ and } F_{rR} = \frac{u_R}{a_R}. \tag{A.17}$$

It is possible to derive a relation for flow stage behind the shock in terms of only the initial data stage ahead of the shock and the shock Froude number. Since the flow must be supercritical through the shock, it is required that $h_* \geq h_R$ and also $q_R \geq 1$. Therefore

$$q_R = F_S - F_R \geq 1. \tag{A.18}$$

The water depth in the star region behind the shock is then

$$h_* = h_R\left[\frac{-1+\sqrt{1+8\left(F_{rS}-F_{rR}\right)^2}}{2}\right], \tag{A.19}$$

and the particle velocity behind the shock is given by

$$u_* = u_R + a_R\left(1-\frac{h_R}{h_*}\right)\left(F_{rS}-F_{rR}\right). \tag{A.20}$$

For a left moving shock the two above equations read respectively

$$h_* = h_L\left[\frac{-1+\sqrt{1+8\left(F_{rL}-F_{rS}\right)^2}}{2}\right], \tag{A.21}$$

$$u_* = u_L + a_L\left(1-\frac{h_L}{h_*}\right)\left(F_{rL}-F_{rS}\right). \tag{A.22}$$